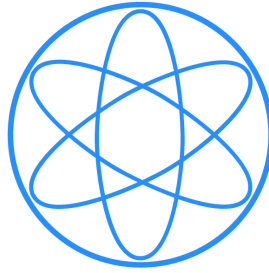


PHYSIK-DEPARTMENT



**Quenching Factor Measurements
of CaWO_4 at mK Temperatures
by Neutron Scattering
for the Dark Matter Experiments
CRESST and EURECA**

Diplomarbeit
von

Raimund Strauss



TECHNISCHE UNIVERSITÄT
MÜNCHEN

Abstract

In the past years, detailed observations and cosmological models have reached the conclusion that large amounts of Dark Matter exist in the universe. Since the standard model of particle physics cannot explain the abundance of non-baryonic matter, weakly interacting massive particles (WIMPs) are predicted by many theories. A promising approach to directly detect such Dark Matter particles is the measurement of nuclear recoils induced by WIMP-nucleon scattering.

The CRESST (Cryogenic Rare Event Search with Superconducting Thermometers) experiment, located in the Gran Sasso underground laboratory (LNGS) in Italy, uses CaWO_4 scintillating crystals, equipped with superconducting transition-edge sensors (TESs), as cryogenic ($\sim 10\text{mK}$) targets with a total mass of $\sim 10\text{kg}$. An event-by-event background discrimination is achieved by simultaneously measuring the deposited recoil (phonon) energy and the associated scintillation light, which is detected by a Si absorber also equipped with a TES. CRESST, combined with technology from the EDELWEISS experiment, will be scaled to a total target mass of up to $\sim 1\text{ton}$ in the future multiple-target experiment EURECA.

CaWO_4 with its heavy constituent tungsten (atomic mass number $A \approx 184$) is a suitable target, since the elastic spin-independent WIMP-nucleon scattering cross-section is predicted to be proportional to A^2 . For kinematic reasons, background neutrons that can mimic WIMP recoils, scatter mainly off oxygen. The heavier the recoiling nucleus, the higher is the ratio between phonon and light signals, which is commonly referred to as Quenching Factor (QF). An accurate determination of the QFs is essential to distinguish between possible WIMP recoils and background. Past measurements were not able to determine the QF of tungsten at mK temperatures with satisfying accuracy.

The neutron-scattering facility at the accelerator of the Maier-Leibnitz laboratory (MLL) in Garching is a unique experiment aiming to determine QFs of target crystals at mK temperatures. Neutrons with energies of up to $\sim 11\text{MeV}$ are scattered off a CRESST-like CaWO_4 cryodetector into neutron-detector arrays positioned at certain scattering angles. By measuring the phonon energies of the nuclear recoils in the cryodetector and performing a Time-of-Flight (ToF) measurement, the recoiling nucleus (O, Ca or W) can be identified for all energies of the incident neutrons. The QFs of the respective elements can then be determined by analysing the data obtained from the phonon and light channels of the cryodetector. Data is acquired by a newly installed VME-based electronics and the challenging data analysis is performed off-line.

The ToF method has successfully been applied and data from one beamtime (~ 1 week) has been analysed. The results of the experiment clearly show that three populations of recoiling nuclei corresponding to O, Ca and W can be identified and - despite low statistics - reasonable tendencies for the QFs are measured. Particularly promising is the possibility to determine QFs at low recoil energies down to the region of interest of the CRESST experiment (10-40keV).

The results obtained so far suggest several improvements to reach maximum performance: The light detector's sensitivity will be increased by the application of the Neganov-Luke effect and a reduction of the mass surrounding the cryodetector will help to suppress background, which is mainly due to parasitic neutron scattering. The experiment in its final phase will be able to characterize different target materials for the future EURECA experiment within beamtimes of typically 2-4 week.

Contents

I	Dark Matter	9
1	Introduction to Dark Matter	11
1.1	Evidence for Dark Matter	11
1.2	Dark Matter Candidates	13
2	The CRESST Experiment	15
2.1	The CRESST Detectors	15
2.2	Experimental Setup	15
2.3	Results and Future Developments	17
2.3.1	Results of the Commissioning Run	17
2.3.2	Current Run	19
3	Further Dark Matter Experiments	21
3.1	Cryogenic Ionization Detectors	21
3.2	NaI Scintillator	21
3.3	Liquid Noble Gases	23
3.4	Obtained Dark Matter Limits	24
4	The EURECA Project	25
4.1	Planned Experimental Setup	25
4.2	Multitarget Aspect	25
II	Neutron Scattering Experiment	29
5	Quenching Factors	31
5.1	Definition	31
5.2	The Birks Equation	32
5.3	Relevance of QF for Dark Matter Search	34
5.4	Earlier QF Measurements	36
5.4.1	Time of Flight Mass Spectrometer	36
5.4.2	Neutron Scattering at Room Temperature	37
5.4.3	Neutron Scattering at mK Temperatures - First Steps	37
5.4.4	Earlier Results for QFs of O, Ca and W	39
6	Working Principle of the Experiment	41
6.1	Time-of-Flight Method	41
6.2	Scattering Angles	42

6.3	Recoil Spectra of CaWO_4 at Fixed Scattering Angles	44
7	Experimental Setup	47
7.1	The MLL Accelerator as a Neutron Source	47
7.1.1	Ion Production and Acceleration	48
7.1.2	Pulsed Ion Beam	48
7.1.3	Neutron Production	49
7.1.4	Mounting of the Cell and Beam-Monitoring System	52
7.2	Cryogenic Setup	52
7.2.1	^3He - ^4He Dilution Refrigerator	52
7.2.2	CRESST-like Detector Module	54
7.3	Neutron Detectors	56
7.3.1	Organic Liquid Scintillators	57
7.3.2	Design of the neutron detectors	58
7.3.3	Construction of a new Mounting System	60
7.3.4	Filling with New Liquid Scintillator	60
7.3.5	Calibration and Discrimination threshold	60
7.3.6	Tests with Different Liquid Scintillators	65
7.4	"Grossmaul" Detector	67
7.4.1	Design and Properties	67
7.4.2	First Measurements	69
7.4.3	Future Improvement	70
7.5	Data Acquisition	71
7.5.1	VME Modules	71
7.5.2	Acquisition Software	72
8	Data Analysis	75
8.1	Data Readout	75
8.2	Analysis of the Cryodetector Pulses	76
8.2.1	Creating a Standard Event	76
8.2.2	Quality Control of the Events	79
8.2.3	Calibration of the Cryodetector	83
8.3	Search for Coincident Events	88
8.3.1	Time Stamp Mapping	88
8.3.2	Neutron- γ Discrimination	89
8.3.3	Double Coincidences	89
8.3.4	Triple Coincidences	90
9	Results	93
9.1	Energy Spectrum of the Neutron Beam	93
9.2	Coincident Events	94
9.2.1	Determination of Triple-Coincidence Events	94
9.2.2	Distribution of Triple-Coincidence Events in Time	95
9.2.3	Error Estimation	97
9.2.4	Identification of the Recoiling Nuclei	99
9.3	Recoil Rates	100
9.4	Quenching Factors	101

10 Discussion of the Results	105
10.1 Consistency of the Measured Data	105
10.2 Problems with the Present Setup	106
10.2.1 Large Mass Surrounding the Cryodetector	106
10.2.2 Resolution of the Light Detector	107
10.2.3 Double-Bunch Structure	107
10.3 Consequences for the Beamtime in October 2009	108
11 Outlook	111
11.1 Future Improvements	111
11.1.1 New Design of the Detector Holder	111
11.1.2 Changes of the Cryostat	111
11.1.3 Neganov-Luke Light Detector	112
11.1.4 Additional Large-Area Neutron Detectors	113
11.1.5 Reduction of Systematical Errors	113
11.1.6 Monte-Carlo Simulations	113
11.1.7 Update of the Analysis Software	113
11.1.8 Improved Beam Monitoring System	113
11.1.9 Application of the CRESST calibration system	114
11.2 New Target Materials for EURECA	114
Bibliography	115
Acknowledgments	119

Part I
Dark Matter

Chapter 1

Introduction to Dark Matter

1.1 Evidence for Dark Matter

The existence of large amounts of non-luminous matter in our galaxy has been claimed since the 1930s - first by F. Zwicky [1] - and the evidence that the majority of the mass of the universe is made up of non-baryonic Dark Matter (DM) has been continuously growing [2].

Strong evidence for DM comes from the detailed study of rotational curves of galaxies. From observations of the emission lines of neutral hydrogen, the velocities of stars can be measured even at high radial distances from the galaxies' centers. The following relation between the velocity v of the star and its distance r from the galaxy core is expected within Newtonian mechanics:

$$v(r) = \sqrt{\frac{GM(r)}{r}} \quad (1.1)$$

where G is the gravitational constant and $M(r)$ is the mass of the luminous matter inside the orbit. However, measurements of rotational curves of galaxies (e.g. the galaxy NGC6503 in figure 1.1) do not show the $r^{-\frac{1}{2}}$ dependence, but a flat distribution even for large distances from the galactic cores.

On large scales, observations of the cosmic microwave background (CMB) provide evidence for the existence of non-baryonic Dark Matter. First discovered by Penzias and Wilson in 1964 [4] and nowadays measured with high precision by satellite missions, the CMB shows small temperature fluctuations over the whole sky. These temperature fluctuations were mapped by WMAP (Wilkinson Microwave Anisotropy Probe) [5]. After expansion into spherical harmonic functions a power spectrum in dependence of the multipole moment l (see figure 1.2) is obtained. For small l and thus large scales, the intensity in the power spectra is low, which means the CMB is homogeneous. From maxima in the power spectrum, the size of the temperature fluctuations in the CMB can be derived and compared with cosmological models. Best agreement has been found for the Λ CDM theory [6], i.e. a universe dominated by Cold Dark Matter and the cosmological constant Λ . According this model, $\sim 23\%$ of the mass-energy density of the universe is due to DM, only $\sim 4\%$ originates from baryonic matter and $\sim 73\%$ is due to Dark Energy (Λ) the physical origin of which is also unknown.

Further convincing evidence for DM is demonstrated by the merging of two galaxy

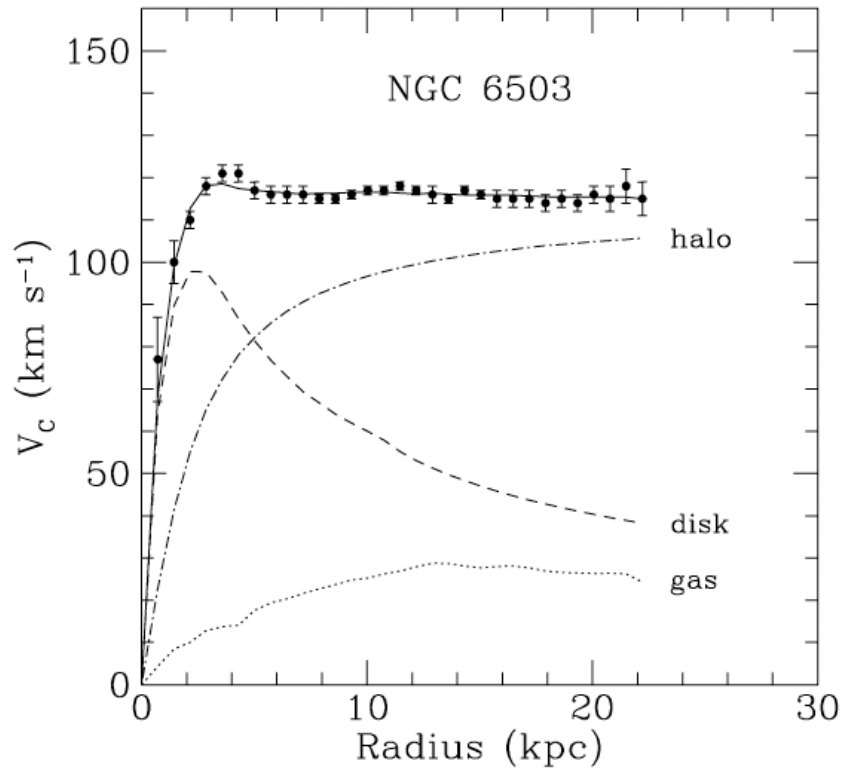


Figure 1.1: Rotational curve of the galaxy NGC 6503 together with the contributions of gas, optical disc and halo [3].

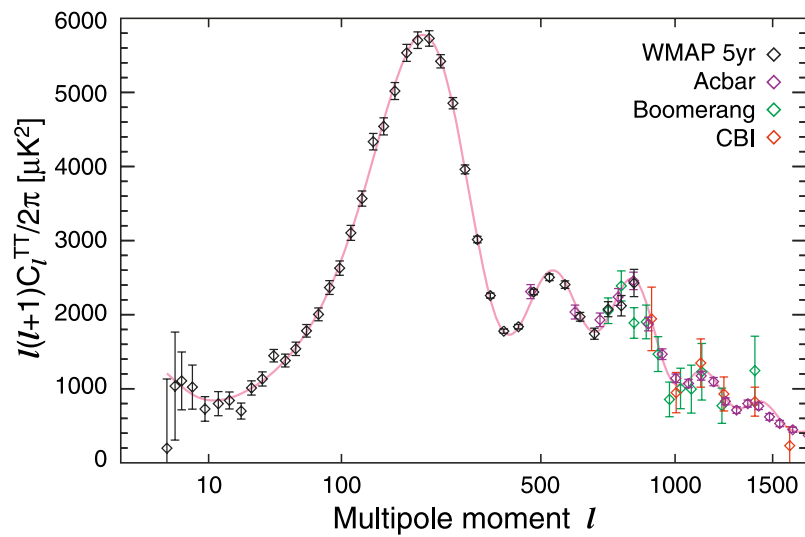


Figure 1.2: Five-year power spectrum obtained from WMAP [5] plotted together with the results from Acbar, Boomerang and CBI. The solid curve fits the ΛCDM best. For details see text and [6].

clusters, as observed for the Bullet Cluster (see figure 1.3) [7]. Gravitational lensing shows the gravitational potential of the two galaxies (solid lines), whereas optical and X-ray pictures show the luminous matter distribution after the merging process for stars and intercluster plasma, respectively. As clearly visible in figure 1.3, the cluster cores passed through each other with nearly no interaction, whereas the gas shows clear signs of friction and is thus concentrated between the two cluster cores. This strongly demonstrates, that the major part of the matter is due to a component which is weakly interacting and which we do not yet understand: Dark Matter.

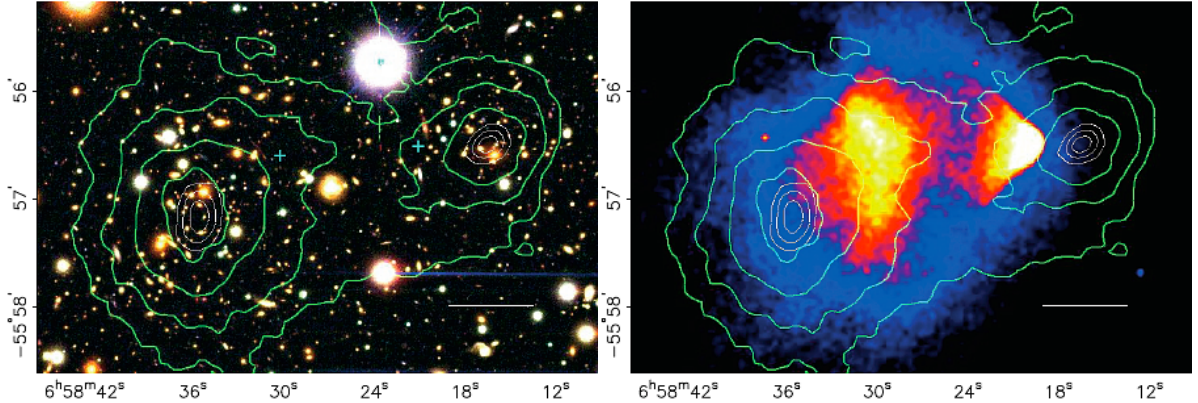


Figure 1.3: Left: Optical image of the "Bullet Cluster" observed by the Magellan telescope. The solid lines indicate the gravitational potential. Right: X-ray image of the "Bullet Cluster" observed by the Chandra telescope. The white horizontal bars indicate distances of 200kpc. Images from [7].

1.2 Dark Matter Candidates

Although Dark Matter has not yet been discovered, a few constraints are already known from the observations discussed in section 1.1. DM particles have to interact weakly with baryonic matter, otherwise it would have been already detected. Since apparently it clumps on small-scale structures - as for example shown for the Bullet Cluster [7] - DM particles have to be heavy, otherwise they would be relativistic and smear out structures that are present in the universe. Candidates proposed by different models are commonly referred to as WIMPs (Weakly Interacting Massive Particles). In the following the most important candidates are listed.

- **Neutrinos:** The only possible candidate among the particles of the standard model is the neutrino, since it is interacting only weakly and by gravitation. However, experiments show that neutrinos are light $m < 2.3eV$ [8]. Thus they alone cannot represent the large amount of non-baryonic matter, since small-scale structures could not exist due to the relativistic velocities of the neutrinos.
- **Supersymmetric Particles:** The most likely candidate for a massive DM particle is the lightest supersymmetric (SUSY) particle, the neutralino, which is stable and is predicted to interact with baryonic matter only through weak interaction (and gravitation). The MSSM (Minimal Supersymmetric extension of the Standard

Model) theory [9] predicts cross-sections for direct detection of these particles by nuclear scattering off baryonic matter - for spin-dependent and spin-independent interaction. The MSSM also provides the possibility of indirect detection via particles produced in the coannihilation of SUSY particles, since they are proposed to be Majorana particles.

- **Axions:** These hypothetical particles are introduced to solve the CP problem of the QCD (Quantum Chromodynamics). Although they are light ($m < 10^{-2}\text{eV}$), they could have built small-scale structures and thus make up Dark Matter, as they were never - in comparison to the neutrinos - in thermal equilibrium in the early universe [10].

Chapter 2

The CRESST Experiment

The CRESST (Cryogenic Rare Event Search with Superconducting Thermometers) experiment uses cryogenic detectors for the direct measurement of Dark Matter particles. In this chapter, the basics of the experiment after the upgrade to CRESST-II [11], its setup and the obtained results are described. CRESST is successfully running at the moment and new results will be published in 2010.

2.1 The CRESST Detectors

The CRESST detectors use CaWO_4 crystals at mK temperatures as target material and silicon-on-sapphire (SOS) scintillating substrates to detect the scintillation light [11]. One cylindrical CaWO_4 absorber crystal has a mass of $\sim 300\text{g}$ and is 4cm in height and 4cm in diameter. On the surface of the crystal a transition-edge-sensor (TES) is deposited, to obtain a highly sensitive measurement of temperature changes in the absorber. The TES relies on a tungsten film, which is stabilized in the transition from the superconducting to the normal-conducting state ($\sim 15\text{mK}$). As can be seen in figure 2.1, small changes in temperature cause a significant change in the resistance of the sensor. In this case the phonon signal induced by a scattered particle can be measured. CaWO_4 with its heavy constituent tungsten was chosen as target material, since the experiment is looking for coherent - spin independent - WIMP interaction with a predicted cross-section proportional to A^2 , where A is the atomic number (see section 5.3). In addition, CaWO_4 has a high output of scintillation light.

The SOS light detectors that are sensitive down to $\sim 20\text{eV}$ consist of a sapphire waver of 40mm diameter and 0.4mm thickness, with a silicon layer is epitaxially grown on one side. Again a tungsten TES is used for readout.

Both detectors are combined to a CRESST module inside a reflective, scintillating housing, as drawn schematically in figure 2.2. The detectors are read out simultaneously by SQUIDs (Superconducting Quantum Interference Devices) [11]. In figure 2.3 an opened CRESST detector module is shown.

2.2 Experimental Setup

The CRESST experiment is based in the Gran Sasso underground-laboratory (LNGS) in Italy, where the muon-induced background is reduced (compared to the flux at the

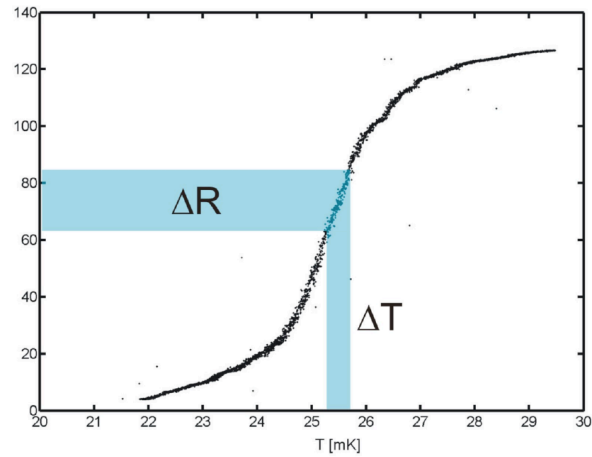


Figure 2.1: Typical transition curve of a transition-edge-sensor (TES) from the superconducting to the normal-conducting state [12]. As indicated, small changes in temperature cause significant changes in the resistance of the sensor.

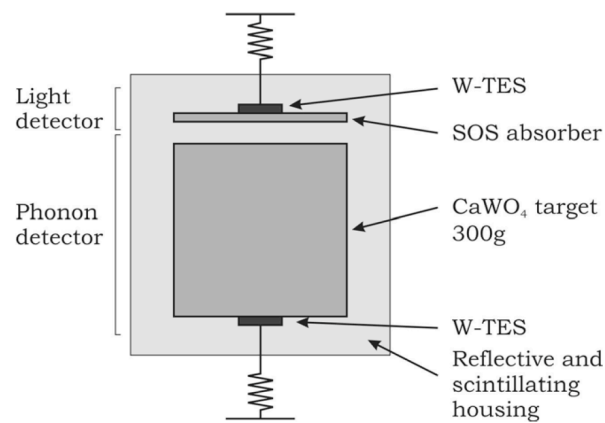


Figure 2.2: Schematic picture of the CRESST detector module, where the most important parts are indicated [11]. Each TES of both detectors is weakly coupled to the mixing chamber of the cryostat (see section 7.2).

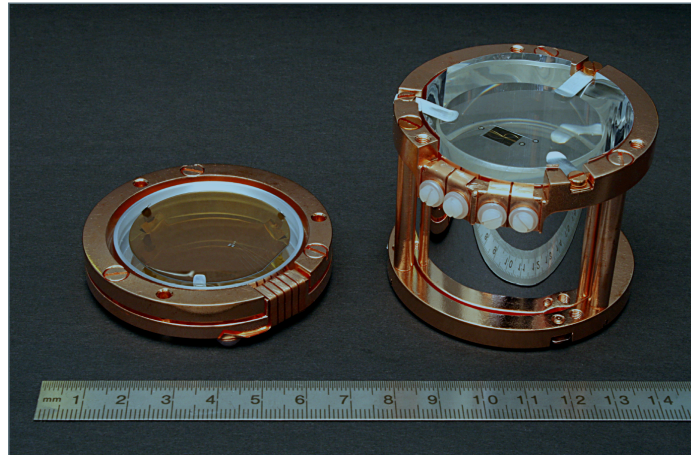


Figure 2.3: Opened CRESST detector module [11], with the SOS light detector on the left and the CaWO_4 target crystal on the right side. The crystal is encircled by a scintillating foil and hold by silver-coated bronze clamps within a structure made of copper. On the top face of the crystal the TES structure is visible.

surface) by six orders of magnitude to a rate of about $1\text{m}^{-2}\text{h}^{-1}$ [13]. The detectors are cooled to mK temperatures by a ^3He - ^4He dilution refrigerator (as described in detail in section 7.2). A cold finger (made of copper) with a length of $\sim 1\text{m}$ couples the detector volume to the mixing chamber in order to suppress background originating from the devices of the cryostat. To further reduce the background (discussed in 5.3), a system of active and passive shieldings is installed around the cryostat (see figure 2.4). The detector volume is enclosed by 14cm of copper, 20cm of lead and a gas-tight radon box, which is continuously flushed with pure N_2 gas and thus reduces the activity due to radon. The Rn-box itself is surrounded by a neutron shield consisting of 45cm thick polyethylen blocks and an active muon-veto (~ 20 plastic-scintillator panels) [11].

Up to 33 detector modules can be mounted within the detector volume in the so-called "carousel" (see figure 2.5). A multichannel electronics system with 66 SQUID-readout channels and the respective data acquisition was installed to handle the large number of detectors. The whole experimental setup and readout electronics are housed in a Faraday cage to reduce electro-magnetic disturbances.

2.3 Results and Future Developments

2.3.1 Results of the Commissioning Run

In the commissioning run of CRESST II from March 27th to July 23rd 2007, two detector modules were operated with a cumulative exposure of 47.9kg-days. Since the light output per deposited energy is strongly dependent on the type of particle interacting in the scintillator crystal (commonly referred to as quenching, see chapter 5), the ratio between light and phonon energy (light yield) can be used to discriminate background from possible WIMP events. Different measurements [14] [15] [16] clearly demonstrate: The heavier the recoiling particle, the lower is the light output of a recoil event. Since

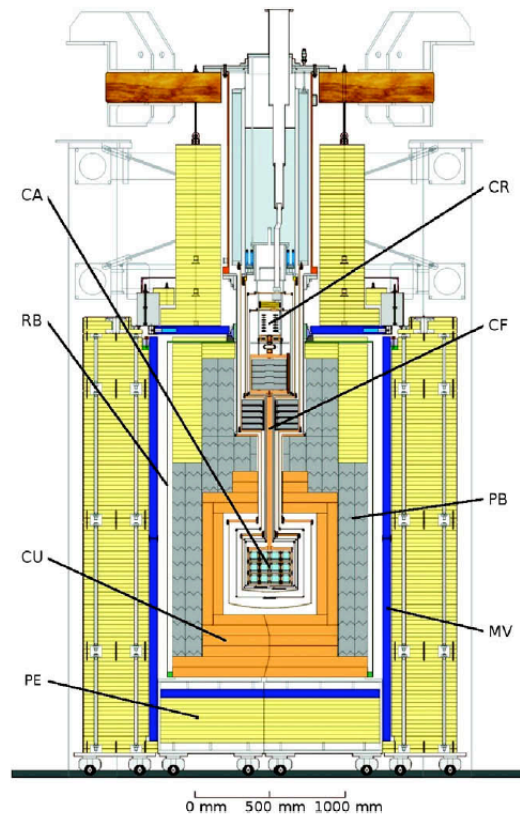


Figure 2.4: The CRESST cryostat after the upgrade to CRESST II: CA indicates the detector carousel, CR the mixing chamber of the cryostat, CF the cold finger, PB the lead shield, MV the muon veto, PE the polyethylen shield, CU the copper shield and RB the radon box [11]. For explanations see text.

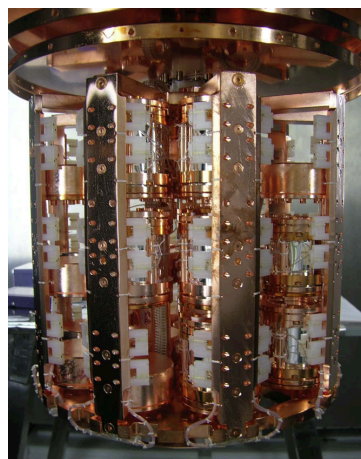


Figure 2.5: The detector holder (called "the carousel") can be equipped with up to 33 CRESST detector modules [11]. It is thermally coupled to the mixing chamber by a cold finger made of copper (see text).

tungsten recoils are highly preferred due to the $\sim A^2$ dependence of the cross-section for WIMP-nucleus interaction, an upper limit for the light output for a possible WIMP-induced recoil can be defined. In figure 2.6 the light yield (normalized to one for electron recoils) is plotted versus the phonon energy deposited into the CaWO_4 crystals of the two detectors operated in the commissioning run. Below the solid (red) curve in this plot, 90% of all WIMP events due to tungsten recoils are expected. After an exposure of 47.9kg-days three events remain in the acceptance region between 10 and 40keV.

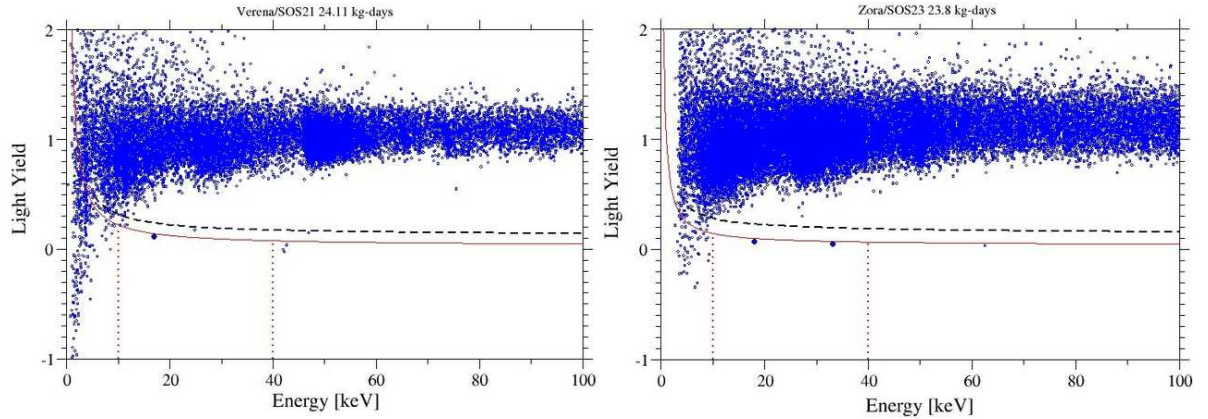


Figure 2.6: Yield plots of the two detectors (Zora and Verena) operated during the commissioning run of CRESST-II in 2007 [11]. Below the dashed (black) curve 90% of all nuclear recoils and below the solid (red) curve 90% of all tungsten recoils are expected. As described in section 5.3, WIMPs are assumed - in the energy range from 10 to 40keV - to scatter preferably off tungsten. At a total exposure of 47.9kg-days, three candidate events remain in the tungsten acceptance region.

From the measured WIMP event-rate, an upper limit for the coherent - spin independent - WIMP-nucleon scattering cross-section can be obtained. This limit is plotted in figure 3.3 in section 3.4 with a minimum of $4.8 \cdot 10^{-7}$ pb at a WIMP mass of ~ 50 GeV [11].

2.3.2 Current Run

CRESST is running continuously since July 4th 2009, after the cooldown process was interrupted by the serious earthquake in April 2009 in the Abruzzi. Currently 18 CRESST detector modules are installed in the setup, of which ten are giving data, resulting in a total target mass of 3kg. Assuming that the main part of the data-set is usable, the current CRESST run already has an exposure of several 100kg-days [17]. With additional data from the year 2010, the CRESST experiment should be able to reach a limit of the coherent WIMP-nucleon cross-section in the $\sim 10^{-8}$ pb region.

Chapter 3

Further Dark Matter Experiments

This chapter gives a brief overview of the most important running experiments for the direct detection of Dark Matter (DM) besides CRESST.

3.1 Cryogenic Ionization Detectors

The experiments CDMS [18] - currently the leading DM experiment - and EDELWEISS [19] use the simultaneous measurement of heat and ionization caused by particle interactions in semiconducting absorbers. The CDMS (Cryogenic Dark Matter Experiment) experiment, located at the Soudan Underground Laboratory, USA, uses cylindrical Ge and Si absorbers (thickness $\sim 10\text{mm}$, diameter $\sim 76\text{mm}$) operated at cryogenic temperatures ($< 50\text{mK}$). On one side of each detector four phonon sensors are deposited in order to measure the recoil energy and position of an event. The ionization signal is measured by electrodes on the other side of the crystal. The ratio of ionisation and phonon signal provides an efficient event-by-event discrimination between electron and nuclear recoil events. In the most recent publication [18], data taken between July 2007 and September 2008 with a total exposure of 612kg-days were published. The whole CDMS data set pushes the lowest upper limit for the elastic WIMP-nucleon spin-independent cross-section down to $3.8 \cdot 10^{-8}\text{pb}$ for a WIMP mass of 70GeV. Two events were observed in the event acceptance region, which is shown in figure 3.1.

The French-German EDELWEISS (Experience pour Detecter les WIMPs en Site Souterrain) experiment, located in the Laboratoire Souterrain de Modane (LSM), uses a similar detector principle based on Ge crystals of 70mm diameter and 20mm height. Recently published data of the experiment's phase II [19] sets an upper limit for the WIMP-nucleon cross-section of $1.0 \cdot 10^{-7}\text{pb}$ at 80GeV from a total effective exposure of 144kg-days. One possible WIMP candidate recoil event is observed.

3.2 NaI Scintillator

The DAMA experiments (DAMA/NaI, DAMA/LXe, DAMA/LIBRA) [20] are the only experiments that claim the discovery of Dark Matter, based on an annual modulation of the measured signal, which is predicted to be due to the varying velocity of the Earth

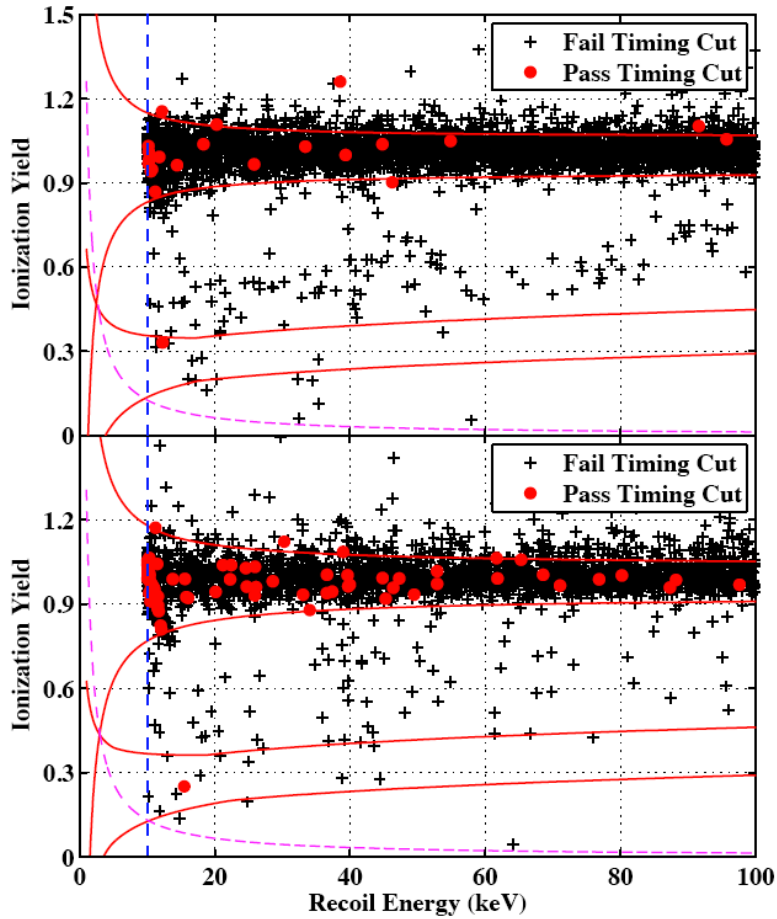


Figure 3.1: Ionization yield (ratio of ionization and recoil energy) of events obtained by two CDMS II detectors is plotted versus the recoil energy. The solid (red) curve indicate the 2σ electron and nuclear recoil bands. Round (red) markers mark the two candidate events inside the nuclear recoil band, after the application of timing cuts. For more detail concerning these results see [18].

relative to the WIMP halo. The DAMA/LIBRA experiment is situated in the Gran Sasso Laboratory (LNGS) and uses 25 ultra-pure NaI crystals (doped with Ti), whose scintillation light is detected with photomultipliers. The detectors exhibit a total target mass of 250kg. After a total exposure of 0.3ton-days, an annual variation of 2% within the energy interval between 2 and 4keV is measured (see figure 3.2).

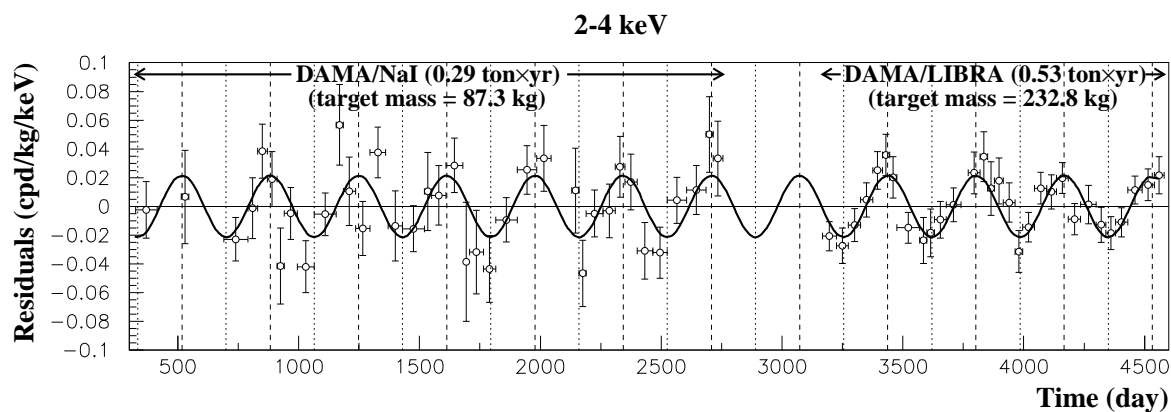


Figure 3.2: Residual rate of single-hit events in the energy interval from 2 to 4keV measured by DAMA/LIBRA and DAMA/NaI. The annual fluctuation is clearly visible and represented by a superimposed cosinoidal function (solid line). The zero of the time scale is January 1st [20].

However, these results - assuming elastic scattering - are for the most part already excluded by other experiments (see figure 3.3). But the results are compatible with the inelastic Dark Matter (iDM) theory, as discussed for example in [21]. Anyway other experiments have to prove these results and careful investigations concerning background and possible systematical errors are necessary.

3.3 Liquid Noble Gases

A different approach to detect Dark Matter particles is the use of liquid noble gases, as for example Xe or Ar. The most successful experiment is the XENON experiment [22] situated in the Gran Sasso Laboratory. The background discrimination is based on the scintillation/ionization ratio being different for electron and nuclear recoil events. The XENON detector is realized as a two-phase time-projection chamber (TPC) with liquid Xe as absorber and a gaseous Xe-phase on top of it. After an interaction of a particle in the liquid phase, charge carriers and scintillation light are produced. The charges are drifted by an electric field to the gaseous phase, where they produce a second light flash. The light is detected by two arrays of photomultipliers positioned on the bottom and at the top of the detector. These two signals and the drift time of the charges are used for active background suppression. The experiment is currently in the XENON10 phase with a target mass of 17kg and has set an upper limit for the WIMP-nucleon elastic spin-independent cross-section of $\sim 4.5 \cdot 10^{-8}$ pb for WIMP masses around 30GeV from a total effective exposure of 58.6kg-days. The next phase of the experiment is planned with a target mass of up to 1ton and an improved background suppression system.

3.4 Obtained Dark Matter Limits

The upper limits for the WIMP-nucleon elastic spin-independent cross-sections, which are obtained by the DM experiments described in this work, are shown in figure 3.3 together with a large range of theoretical predictions [23].

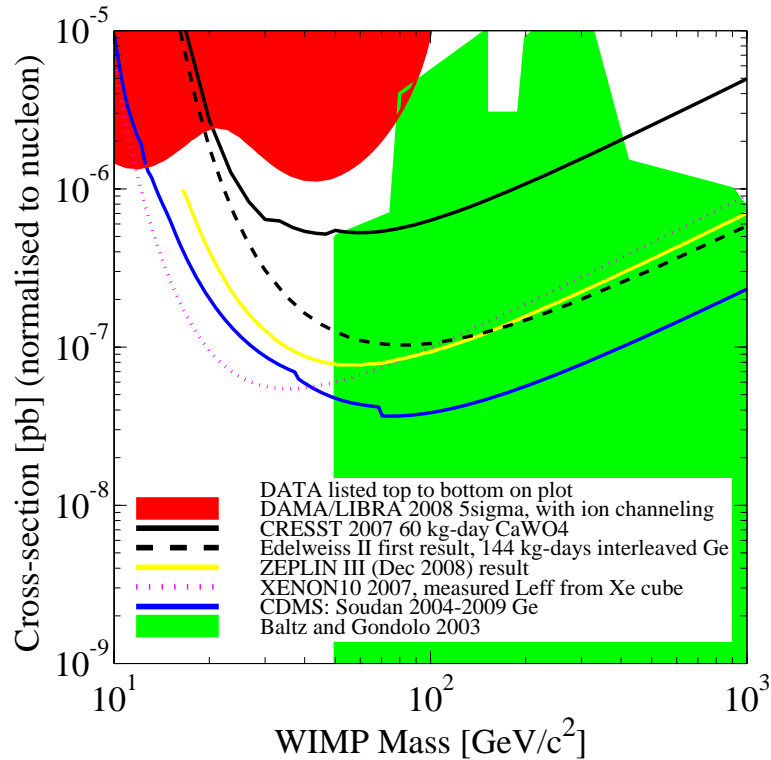


Figure 3.3: Exclusion plot for elastic spin-independent WIMP-nucleon scattering. The limits of several important Dark Matter experiments are shown together with theoretical predictions [23]. Picture taken from [24].

Chapter 4

The EURECA Project

EURECA (European Underground Rare Event Calorimeter Array) will be the future European Dark Matter search experiment using cryogenic detectors with a target mass in the ton-scale [25]. The collaboration has started in March 2005, initially based on CRESST (see section 2) [11], EDELWEISS (see section 3.1) [19] and ROSEBUD (Rare Objects SEArch with Bolometers Underground) [26], but additional groups are joining. The project is aligned with the European Astroparticle Roadmap Recommendations for multiple targets and multiple techniques.

4.1 Planned Experimental Setup

EURECA is planned to be based in the LSM (Laboratoire Souterrain de Modane) in France, which is the deepest site in Europe with about 4800m.w.e. (meters water equivalent). The cosmic muon-rate is suppressed by seven orders of magnitude to $\sim 4\text{m}^{-2}\text{day}^{-1}$. The excavations for the new lab - that will host the EURECA experiment - are planned for 2010 together with the construction of a safety gallery for the existing road tunnel. The planned tunnel system is shown in figure 4.1.

The experiment will consist of two individual cryostats for mK temperatures to allow changes on one setup while the other cryostat is running (see figure 4.2). The detector volume will be surrounded by $\sim 3\text{m}$ of water as a shield against background and the water tanks will be additionally equipped with photomultipliers (PMTs) to establish an active Cherenkov muon-veto system. Only the mixing chamber of the dilution refrigerator will be in the water tank, whereas the other cryogenic devices are placed outside to reduce radioactive contamination around the detector volumes. The pumping system will be housed in a separate cave in order to avoid vibrations (for details concerning dilution refrigerators see section 7.2). The detector modules, that are mainly based on CRESST and EDELWEISS techniques, will be installed in tower-like structures to allow quick detector exchange without long interruptions.

4.2 Multitarget Aspect

The EURECA project is based on the expertise acquired by the CRESST and EDELWEISS experiments, which are both using complementary background discrimination techniques: light and phonon detection in CRESST, phonon and ionization detection

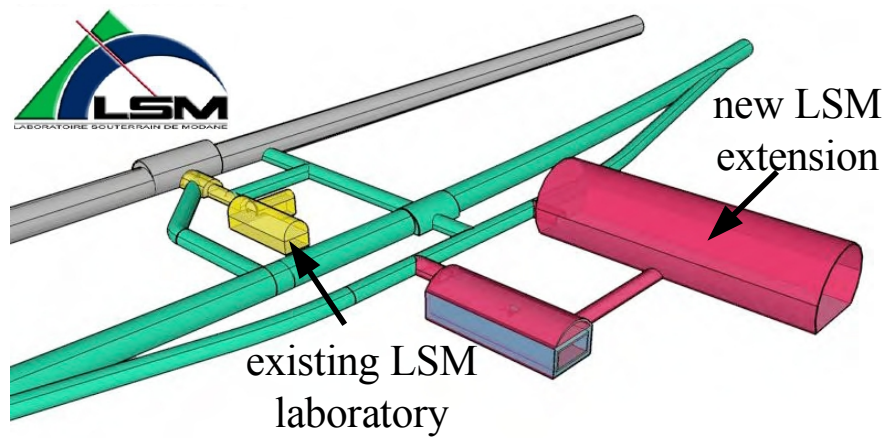


Figure 4.1: Sketch of the LSM underground laboratory in Modane, France, after the excavations for the new safety gallery and the new laboratories for the EURECA experiment are finished.

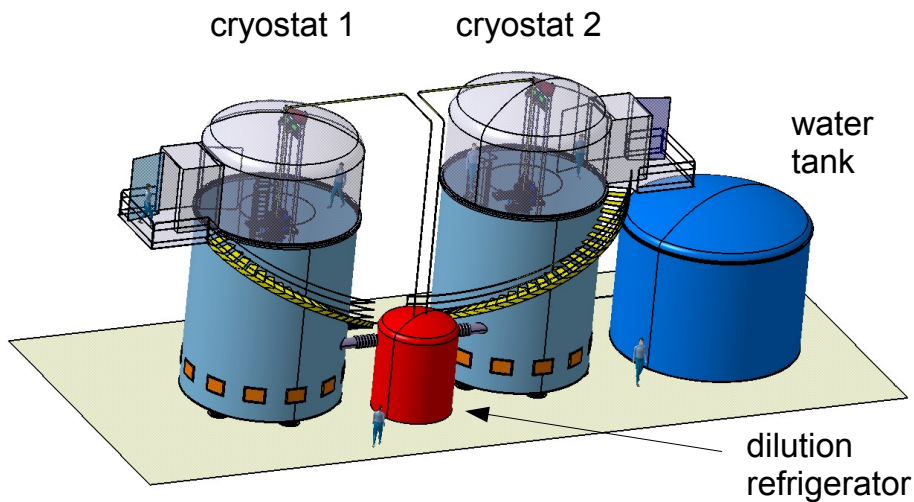


Figure 4.2: Planned setup of the EURECA experiment [27] with two individual cryostats connected to one dilution refrigerator. Except for the mixing chamber, all devices of the dilution refrigerator are placed outside the cryostats. Both cryostats are submersed in water to achieve optimal shielding against background radiation. A separate water tank can take the water of the shielding, if the setup of one of the two cryostats has to be changed.

in EDELWEISS. The cryogenic detectors of different target materials - e.g. scintillating CaWO_4 crystals and semiconducting Ge - will be arranged closely packed in tower-like structures and altogether have a target mass of several 100kg. Multiple-target materials allow to test the predicted A^2 -dependence of the coherent spin-independent WIMP-nucleon cross-section [28] due to different target materials with a wide range of atomic mass number A . Different scintillating crystals -besides the initial choice of CaWO_4 due to the expertise gained in the CRESST experiment - are under investigation and are discussed in more detail in section 11.2. The major goal of EURECA is to reach a limit for the WIMP-nucleon cross-section in the $\sim 10^{-10}$ pb region, which is currently most favoured by theory [29].

Part II
Neutron Scattering Experiment

Chapter 5

Quenching Factors

As described in chapter 2.1, the CRESST detectors simultaneously measure the deposited energy of a particle scattered in the CaWO_4 crystal and the corresponding scintillation light. The fact that the relative light output of an event is strongly related to what kind of particle is interacting, is commonly referred to as quenching. The so-called Quenching Factor (QF) is introduced in order to characterise this behavior.

5.1 Definition

In figure 5.1 left the phonon signal is plotted versus the light output of a typical CRESST-like detector module irradiated by gammas.

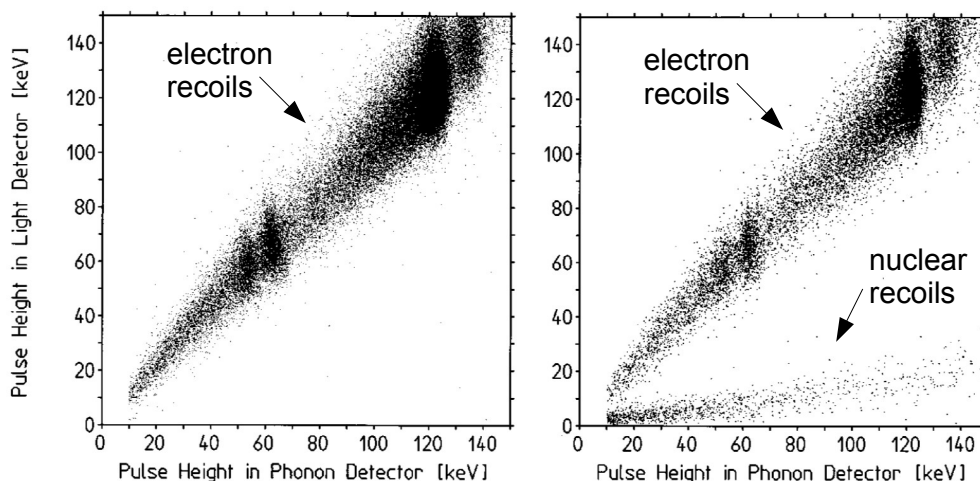


Figure 5.1: Detector response of a scintillating crystal operated as cryogenic detector used in the CRESST Dark Matter experiment. The phonon energy is plotted against the light energy. In the left panel the detector is irradiated by a ^{57}Co and a ^{90}Sr source, in the right panel with an additional AmBe neutron source. Clearly two bands corresponding to electron and nuclear recoils in the target arise. After calibration (see text), the pulse height in the light detector is given in terms of the electron-equivalent energy E_{ee} . Plot from [30].

Clearly one band with different lines, originating from discrete gamma energies can be seen. There are different methods to calibrate the channels:

- The detectors of the CRESST experiment are calibrated with the $\sim 122\text{keV}$ γ -line from a ^{57}Co source and the scale is linearized by heater pulses. This so-called control pulses deliver a known energy via ohmic heating in order to determine the pulse height-energy relation for the whole energy range [11].
- In the setup described in this work, no heater pulses are available. Hence different gamma sources are used to calibrate the detectors (^{137}Cs , ^{133}Ba , ^{55}Fe). In the energy region of the γ sources ($> 100\text{keV}$), the pulse height-energy relation is fairly linear, as shown in [16].

As the light output from a scintillator like CaWO_4 is only in the order of 1%, the phonon energy holds as a measure for the total deposited energy E_R in the crystal, whereas the energy calibration of the light channel is given in terms of the so-called electron-equivalent energy E_{ee} (figure 2.1). The Quenching Factor is defined as:

$$QF = \frac{E_R}{E_{ee}} \quad (5.1)$$

By definition the QF for a electron recoil energy of 122keV is equal to one.

In the right panel of figure 5.1 the crystal is additionally irradiated by an AmBe neutron source. A second band of events can be seen, corresponding to nuclear recoils induced by neutrons. The lightoutput is significantly lower than for electron recoil events leading to higher values of QFs.

Often the Light Yield Y is used. It is defined as:

$$Y = \frac{\text{Amplitude in the Light Detector}}{\text{Amplitude in the Phonon Detector}} \quad (5.2)$$

If the Light Yield is plotted versus the total energy measured by the phonon detector, two horizontal bands appear, corresponding to electron recoils (by convention: $Y = 1$) and nuclear recoils, respectively. As an example, figure 5.2 shows the response of the CRESST detector module Verena/SOS21 in presence of a neutron source during the commissioning run of CRESST II.

The Quenching Factor is then determined as:

$$QF = \frac{\text{Light Yield for an Electron Recoil Event of Energy } E}{\text{Light Yield for a Nuclear Recoil Event of Energy } E} \quad (5.3)$$

With the current setup of the cryogenic detectors, the resolution of the light detectors is not sufficient to separate individual nuclear recoil bands, that are related to the respective elements in CaWO_4 .

5.2 The Birks Equation

In general there is no reason to believe that the QF is energy-independent and has thus to be determined at different energies. A theoretical description of this problem is given by Birks [31]. As a basis for the following considerations based on the Birks Equation

$$\frac{dL}{dx} = \frac{S \frac{dE}{dx}}{1 + kB \frac{dE}{dx}} \quad (5.4)$$

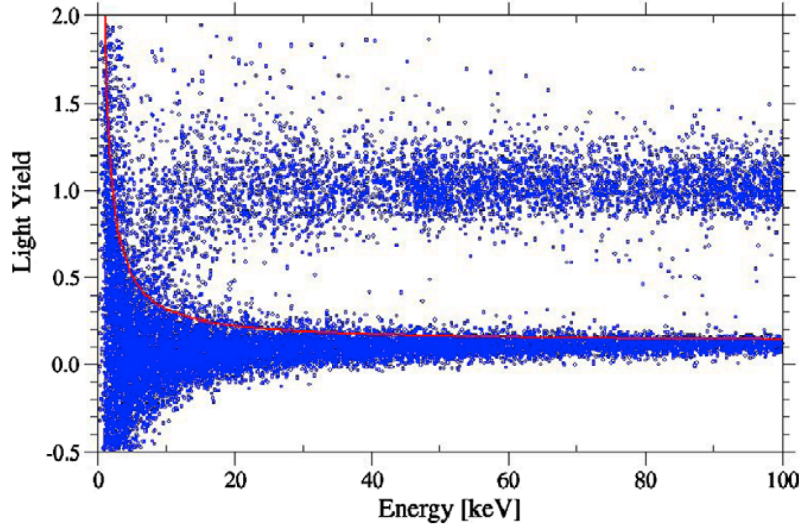


Figure 5.2: Scatter-plot for a CRESST detector module (Verena/SOS21) during the commissioning run of CRESST II in the presence of a neutron source [11]. The light yield is plotted against the phonon energy. The upper band corresponds to electron recoil events, whereas the dominant population below is due to nuclear recoils induced by neutrons. Below the red curve 90% of the oxygen recoils are expected, calculated from the quenching factors (see section 5.4) and the resolution of the light detector. The energy dependence of the Light Yield for the electron recoils is clearly visible in the energy range below 20keV.

where dL/dx is the light energy emitted per unit length, dE/dx is the energy per unit length deposited by the ion, S the scintillation efficiency. The proportionality constants k and B depend on the material (for a detailed description see [32]). For heavy ions, dE/dx gets very large. This leads to a saturation effect for the light output per unit length:

$$\frac{dL_{ion}}{dx} = \frac{S}{kB} \quad (5.5)$$

In this limit, the light yield can be obtained by integration over the path of the ion

$$L_{ion} = \frac{S}{kB} \cdot R \quad (5.6)$$

where R is the range of the ion. With $L_{ion} = SE_{ee}$ (5.1) the QF can be calculated as:

$$QF = \frac{E_R}{E_{ee}} = \frac{E_R S}{L_{ion}} = kB \frac{E_R}{R} \propto E_R \quad (5.7)$$

This means, the Quenching Factor is proportional to the mean specific energy loss $\frac{E_R}{R}$ of the respective ion.

The energy dependence is particularly important, because it is difficult to measure QFs down to the region of interest (10-40keV, see section 9). In figure 5.2 the energy dependence of the Light Yield and thus the QF for electron recoils in CaWO_4 is shown.

5.3 Relevance of QF for Dark Matter Search

Neutron Background

Neutrons are a dangerous background for the Dark Matter Search with CRESST, as they can mimic WIMP interactions. From the simulations [33] concerning the different neutron-background sources in the Gran Sasso Laboratory (LNGS), the rates expected for the CRESST detectors could be obtained. Following neutron sources are considered:

- Fission of ^{238}U produces neutrons with energies below 10MeV, as shown in figure 5.3. As it is present in the rock surrounding the lab, in the concrete walls as well as in the experimental setup itself (e.g. lead) dominates the background rate [33]. With the polyethylene shielding the neutrons can be sufficiently moderated, only the fission neutrons from material inside the shielding remain as a dangerous background.
- Muons can induce high-energy neutrons (up to 100MeV or even higher) outside and inside the experimental setup. Since the polyethylene shielding is not sufficient to moderate the muon-induced neutrons, an active muon veto is installed. However, neutrons that are induced outside the veto (rock, concrete, polyethylene ...) are still a dangerous background. Further details on this topic are discussed in [34].

For the remaining high-energy, muon-induced neutrons, double detection (simultaneous nuclear recoil events in several detectors) is a possible rejection method. For remaining neutrons from fission of ^{238}U an active background reduction by phonon-light discrimination in the detector module is required.

Due to the stoichiometric conditions in CaWO_4 and kinematic reasons, most of the neutrons are expected to be scattered off oxygen, as shown in figure 5.3 for the ^{238}U -fission neutrons, that are an essential part of the background [16].

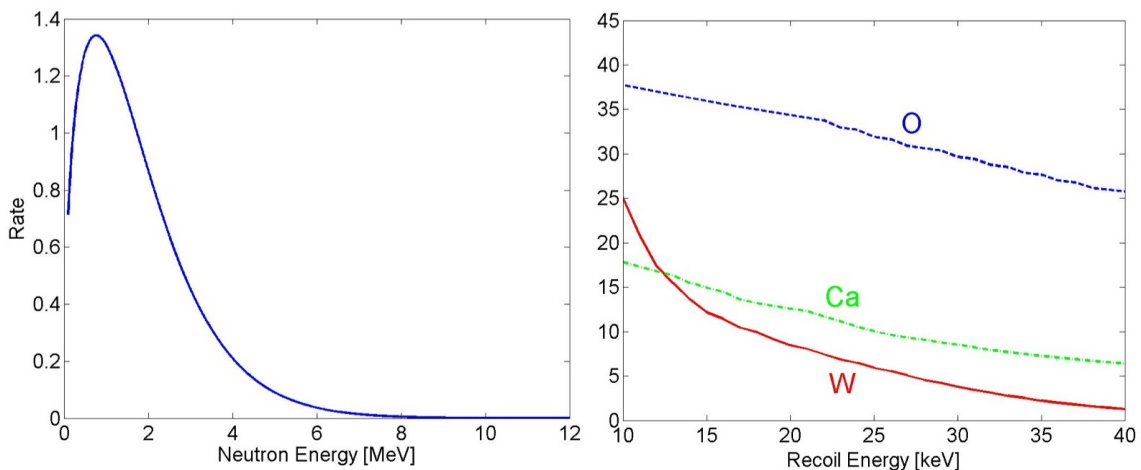


Figure 5.3: On the left side an energy spectrum of fission neutrons from ^{238}U is shown. The right panel shows their expected recoil rate in the region of interest (10-40keV) for the three elements in CaWO_4 [16].

Identification of a Possible WIMP Signal

The CRESST experiment for Dark Matter search is sensitive for spin-independent WIMP interaction with the highest sensitivity for WIMP masses around 50GeV [11]. The WIMP-nucleus scattering probability is given by

$$\Gamma = \frac{M_{Target}}{m_N} \frac{\rho_\chi}{m_\chi} \langle v \rangle \sigma_{\chi N} A^2 \quad (5.8)$$

$$= 300/\text{day} \frac{\frac{M_{target}}{1\text{kg}}}{\frac{A}{100}} \frac{\frac{\rho_\chi}{0.3\text{GeV}/\text{cm}^3}}{\frac{m_\chi}{100\text{GeV}/c^2}} \frac{\langle v \rangle}{230\text{km/s}} \frac{\sigma_{\chi N}}{1\text{pb}} \frac{A^2}{100^2} \quad (5.9)$$

where M_{Target} is the target mass of a material with mass number A , m_N the nucleon mass, ρ_χ is the WIMP density in the Halo of the galaxy, m_χ the WIMP mass, $\langle v \rangle$ the average WIMP speed and $\sigma_{\chi N}$ the total spin-independent WIMP-nucleus cross section [28]. The expected WIMP recoil spectra for different target materials are plotted in figure 5.4 for recoil energies ranging from 0 to 100keV.

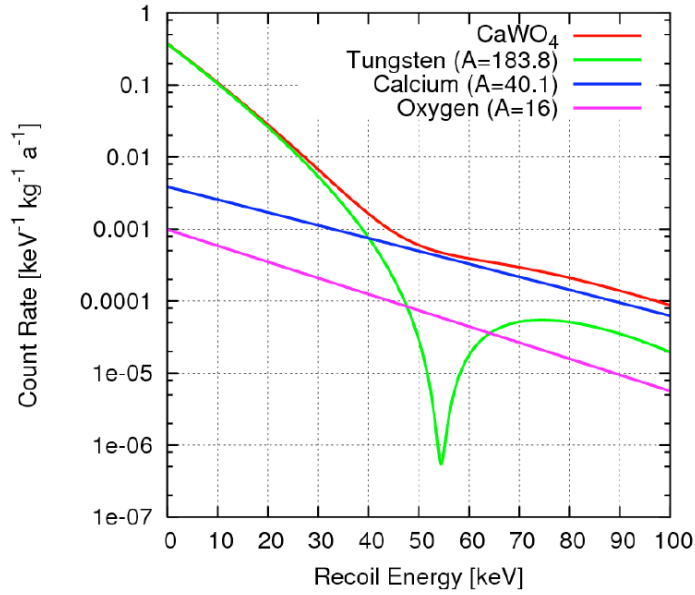


Figure 5.4: Expected WIMP recoil spectra for the three elements W, Ca, O and for CaWO_4 itself are plotted for recoil energies from 0 to 100keV. The calculation was made for a WIMP mass of 60GeV and the WIMP-nucleon cross section $\sigma_{\chi N}$ is assumed to be 10^{-8}pb . The local minimum in the cross section for scattering off W at 55keV is due to the Helm form factor. Plot from [35].

In CaWO_4 , scattering off tungsten is strongly favoured, since the the WIMP interaction cross section is $\propto A^2$,. More than 95% of all scatterings off a CaWO_4 crystal below 40keV are related to tungsten recoils. Thus 40keV is the upper threshold for DM search with a cryogenic CaWO_4 detector (the lower threshold is due to the discrimination threshold at $\sim 10\text{keV}$).

Active Background Discrimination

Since most of the background neutrons scatter off oxygen, whereas WIMP would preferably scatter off tungsten, the identification of the recoiling nucleus in the CaWO_4 crystal can help to discriminate dangerous neutron background from a possible WIMP signal. Hence a detailed understanding of the quenching and an exact measurement of the QFs is necessary to obtain maximal efficiency for the CRESST detectors.

5.4 Earlier QF Measurements

A lot of effort has been made and is still being made to measure the Quenching Factors of CaWO_4 and other materials. This section will give a brief introduction to the already performed experiments and their results.

5.4.1 Time of Flight Mass Spectrometer

At the Max-Planck-Institut für Physik in Munich (MPP) a facility has been installed to measure QFs of different crystals at room temperature. This is realized with a Time-of-Flight Mass Spectrometer (ToF-MS), where ions are shot onto a crystal's surface, causing the emission of scintillation light (see figure 5.5). The ions are produced in a Laser Desorption/Ionization source (LDI), where a pulsed laser induces ions, that are accelerated by a voltage up to 18kV and shot into the main chamber of the TOF-MS. There the ions of a fixed energy and mass are selected [14]. The laser is adjusted at such an intensity that, on average, less than one ion reaches the crystal. The produced scintillation light from the crystal is measured with a photomultiplier tube (PMT).

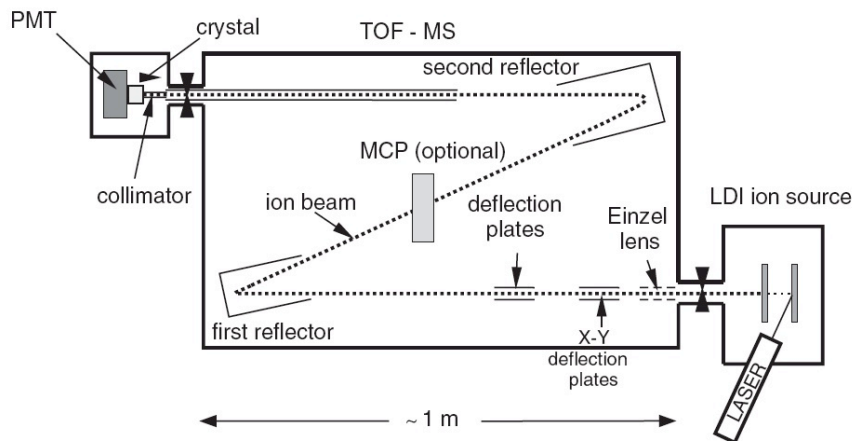


Figure 5.5: Schematics of the setup for the QF measurement with a Time-of-Flight Mass Spectrometer (ToF-MS) [14]. Ions are produced in the Laser Desorption/Ionization source (LDI) and accelerated into the main chamber, where the desired ion energy and mass are selected and finally shot onto the target crystal. The produced scintillation light is detected with a PMT.

The QFs results are listed in table 5.1 for the three elements in CaWO_4 . Al-

though QFs of various elements (even non-mandatory constituents of the scintillator) and crystals can be measured with this setup with a comparatively small complexity, these results have to be verified for the crystal's bulk and for the operating temperature of a cryogenic detector.

5.4.2 Neutron Scattering at Room Temperature

QF measurements at room temperature, but for the bulk of crystals, were performed using neutrons as probes at our institute [15]. A CaWO_4 crystal is irradiated with neutrons from a pulsed monoenergetic neutron beam (11MeV), inducing nuclear recoils in the bulk. Via Time-of-Flight (ToF) measurements at fixed scattering angles, fixed kinematics are achieved. The scintillation light of the chosen recoil energy is measured by two PMTs, that are optically coupled to the CaWO_4 crystal (figure 5.6 left). More details on the working principle of this measurement method are given in chapter 6 and [15].

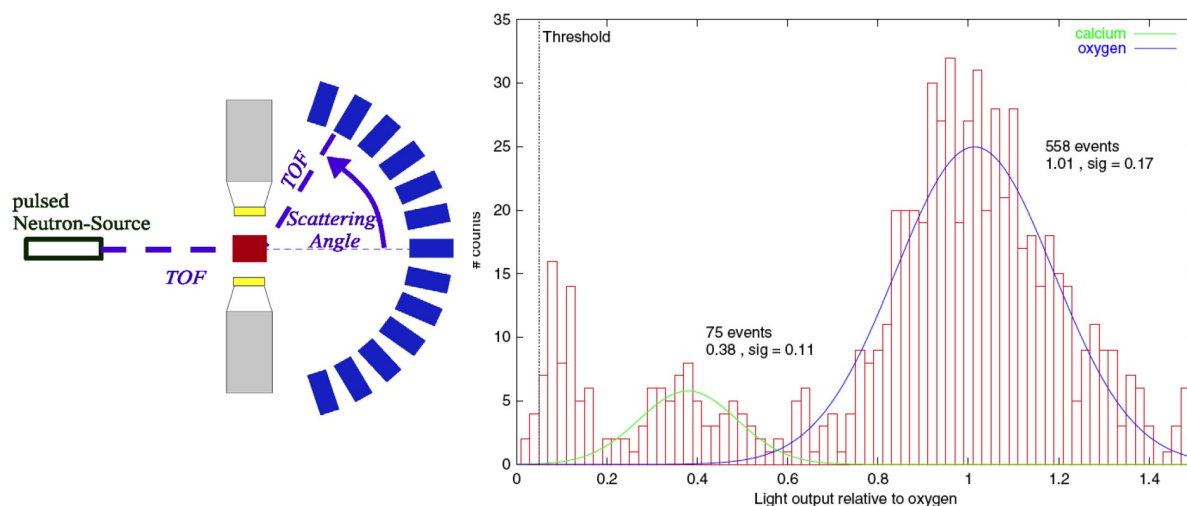


Figure 5.6: Left : Schematics of the experimental setup. The CaWO_4 crystal (red), the two PMT (grey) coupled to the crystal and additional neutron detectors (blue) placed at different scattering angles. Right: Light output of the CaWO_4 crystal irradiated by a monoenergetic neutron beam. The light output is normalised to one for oxygen recoils. The best fits for the two populations, corresponding to oxygen and calcium are shown. Tungsten recoils produce too little light to be detected with this setup. [15]

The response of the CaWO_4 crystal and the QFs results for oxygen/calcium are shown in figure 5.6 (right) and table 5.1, respectively. Since the light output of tungsten recoils is below the threshold of the PMTs, only a lower limit for the QF of tungsten could be obtained.

5.4.3 Neutron Scattering at mK Temperatures - First Steps

In order to further improve the setup described in section 5.4.2, a cryostat was installed at the experimental setup (section 7.2). In [16] and [36], first steps were taken towards

the final goal to measure the QFs of the three elements of CaWO_4 in the mK temperature range.

The CRESST-like detector module was irradiated by neutrons of a monoenergetic neutron beam (11MeV). By analysing the continuous spectra in the nuclear recoil band of the phonon-light discrimination plot, the contributions from the three elements in CaWO_4 can be obtained. Although it is not possible to completely separate the three corresponding bands, the populations can be fitted by Gaussians (figure 5.7) at different phonon energies. Due to kinematic reasons, tungsten recoils are only expected up to $\sim 200\text{keV}$.

With this method the QFs at mK temperatures for oxygen and calcium could be measured with satisfying accuracies, whereas the QF of tungsten still has a large error (see table 5.1).

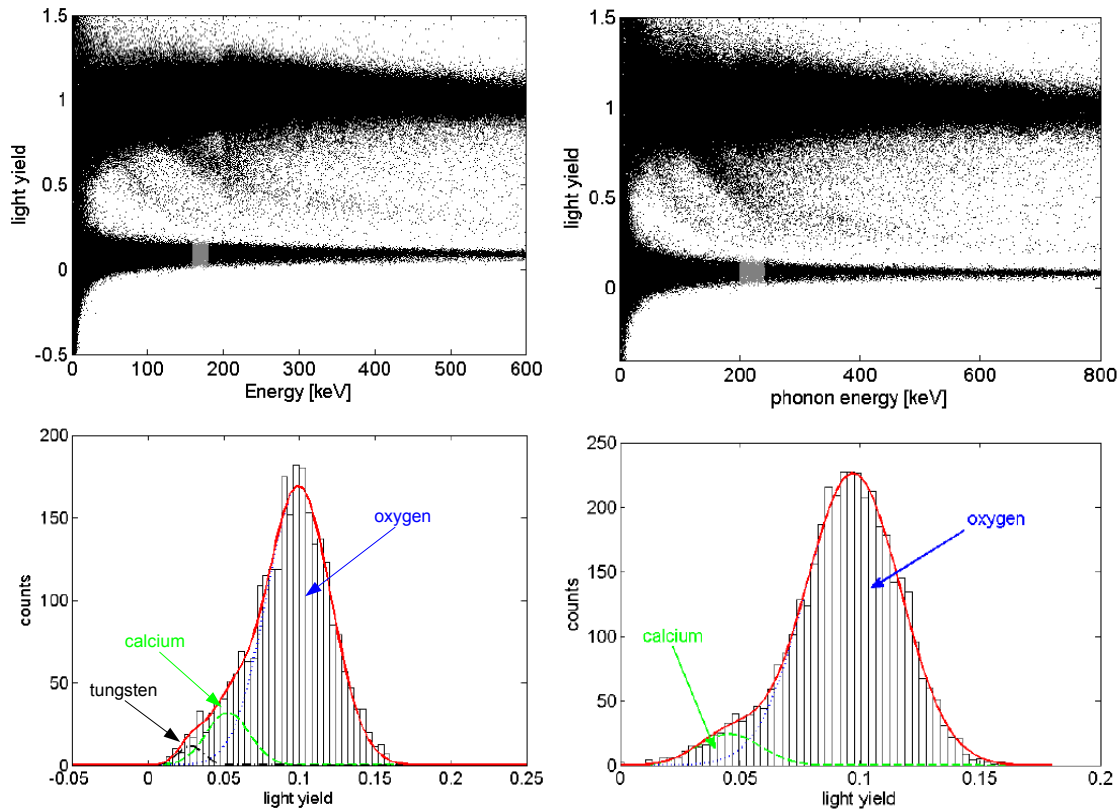


Figure 5.7: Top panels: Light yield versus phonon energy for CaWO_4 irradiated by 11MeV neutrons. The area marked in gray indicates the investigated energy range. Bottom panels: Histograms of the light yield of the nuclear recoil band. These distributions were fitted with a sum of Gaussians corresponding to the elements that are expected to take part in the scattering process in the respective energy range. Left panels: In the energy range from 160 to 180keV three contributions arise (from O, Ca, W) Right panels: For kinematic reasons, in the energy range from 200 to 240keV only two populations (O, Ca) appear. For further details see [16].

5.4.4 Earlier Results for QFs of O, Ca and W

The values of the QF for the three elements in CaWO_4 measured with the experiments described above, are listed in table 5.1.

Element	ToF-MS	Jagemann	Coppi
Oxygen	14.3 ± 0.5	12.8 ± 0.5	10.0 ± 0.1
Calcium	27.4 ± 1	16 ± 4	19.0 ± 2.5
Tungsten	41 ± 3	> 33	35^{+19}_{-9}

Table 5.1: QF results for the experiments described above. Measurements with the Time-of-flight mass spectrometer (ToF-MS) [14], neutron scattering at room temperature (Jagemann) [37] and measurements at mK temperature (Coppi) [16].

Chapter 6

Working Principle of the Experiment

Since it is not possible to obtain a satisfying accuracy for the Quenching Factor (QF) of tungsten at mK temperatures with the setup described in section 5.4.3, another method of measurement has been applied.

A certain scattering angle for the neutrons is chosen. Then, for a fixed neutron energy, one expects three populations of nuclear recoils in the phonon channel of the cryodetector originating from O, Ca and W recoils, respectively (figure 6.1).

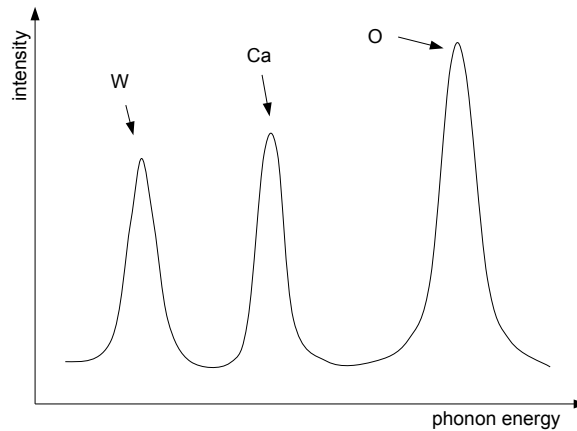


Figure 6.1: Schematics of the expected recoil spectrum in the low-temperature phonon detector for a fixed scattering angle.

6.1 Time-of-Flight Method

A CRESST-like CaWO_4 detector module is irradiated by a pulsed neutron beam from the accelerator. For simplicity, in order to explain the working principle of the experiment, incident neutrons of 11MeV are assumed in this section. Neutron detector arrays are placed at a typical distance of 0.5-2m at different scattering angles to measure the scattered neutrons (see figure 6.2). If the pulse width of the beam bunches is in the order of $\sim 2\text{-}3\text{ns}$, the neutrons scattered in the cryodetector can be identified by measuring the

time between their production in the hydrogen cell at the end of the beamline and the detection in the neutron detector arrays (Time-of-Flight measurement).

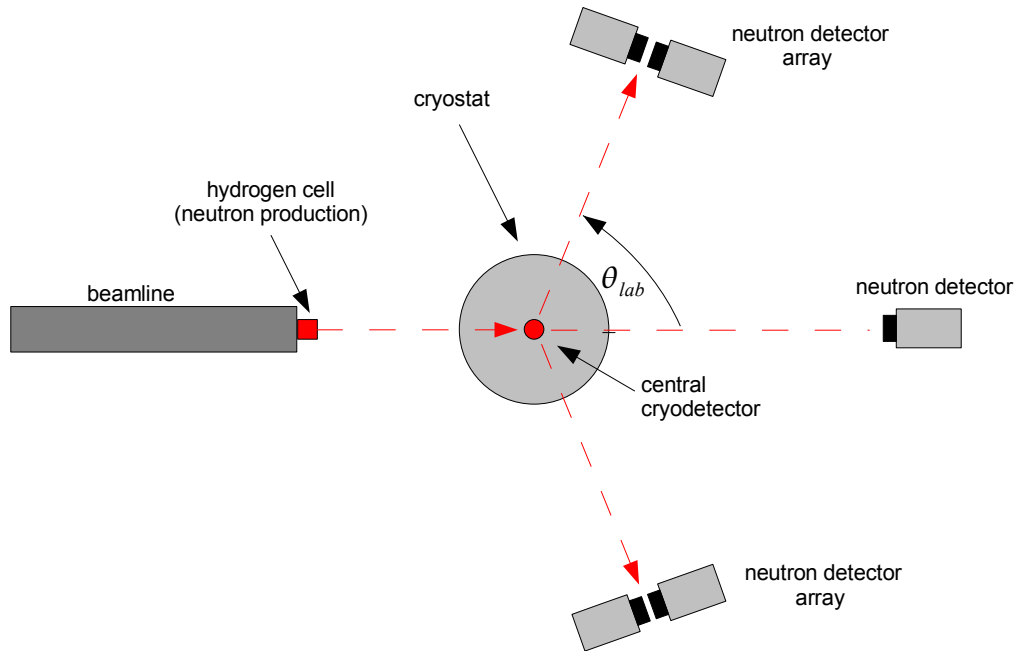


Figure 6.2: Schematical top view of the experimental setup. An additional neutron detector is installed at 0° to monitor the pulsed beam directly.

The events obtained in this way are thus related to one of the three elements in CaWO_4 (as we will see in chapter 9, a background from the surroundings of the cryodetector remains). Due to high energy resolution in the phonon channel of the cryodetector, the recoiling nucleus can be identified. Since in the cryodetector module the phonon and light channel are measured simultaneously, the corresponding light output can be obtained on an event-by-event basis. Thus, a value for the QFs as defined in chapter 5 can be given by averaging the light output of the events in each population and determining their respective phonon energy.

6.2 Scattering Angles

As the QFs for O and Ca at mK temperatures could already be measured with the method described in section 5.4.3, the scattering angle is preferably chosen to get a maximum number of tungsten recoils. Figure 6.3 shows the differential elastic cross-sections for incident 11 MeV neutrons scattering off the three elements in CaWO_4 plotted versus the scattering angle. The cross-section of oxygen is already multiplied by four to take the stoichiometric conditions of CaWO_4 into account.

The cross-section for W shows two local maxima at about 80° and 45° , respectively. Before choosing the preferred scattering angle the following points have to be considered:

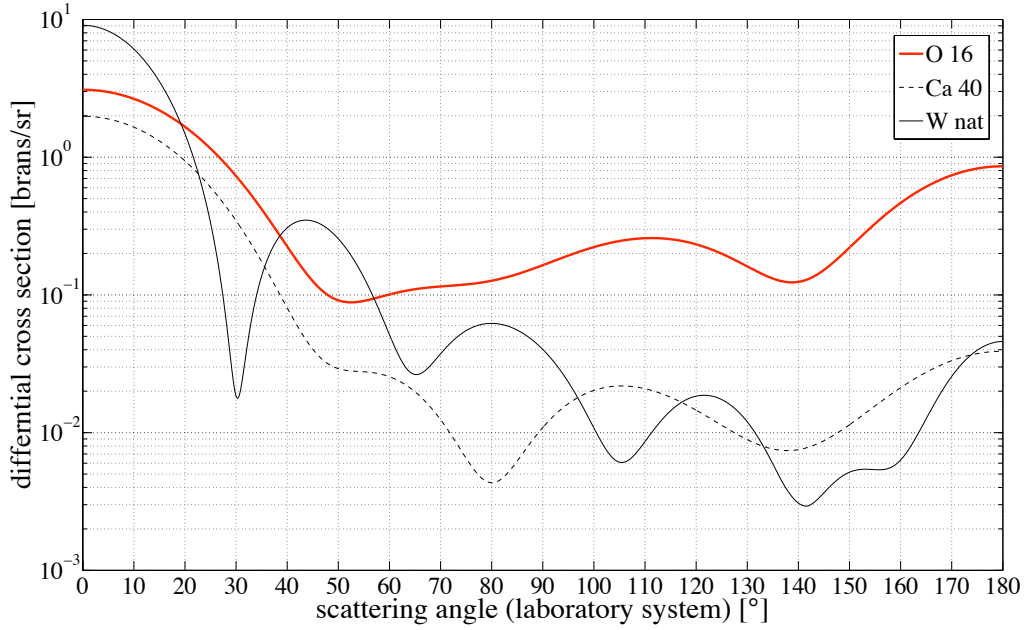


Figure 6.3: Differential elastic cross-sections of O, Ca and W for incident 11MeV neutrons plotted against the scattering angle in the laboratory system. The stoichiometric conditions in CaWO_4 and the natural isotope ratio of tungsten are included.

- The cross section for a scattering angle of 45° is higher by a factor of six than that for 80° .
- At smaller scattering angles, the probability to detect direct neutrons from the source (due to the finite opening angle of the beam itself) increases. Direct neutrons of lower energy might mimic scattered ones and thus give rise to a higher number of accidental coincidences.
- Choosing smaller scattering angles has an impact on the recoil energy E_R in the central detector, since E_R is decreasing and thus making it more difficult to measure the light output which is intrinsically small.

In this work, both angles ($45^\circ, 80^\circ$) were tested and in addition the neutron detector arrays were placed at different distances from the central detector.

The different recoil energies E_R for different elements x and different angles Θ_{CM} can be calculated in the center-of-mass system (CM) for elastic scattering [15],

$$E_R = 2E_n \frac{m_n \cdot m_x}{(m_n + m_x)^2} (1 - \cos \Theta_{CM}) \quad (6.1)$$

where E_n is the incident neutron energy and m_n, m_x are the masses of the neutron and of the element x , respectively. Θ_{CM} can be obtained from the scattering angle in the laboratory system Θ_{lab} by coordinate transformation between the two systems:

$$\cos \Theta_{CM} = -k \sin \Theta_{lab} \pm \sqrt{1 - k \sin \Theta_{lab} \cdot \cos \Theta_{lab}} \quad (6.2)$$

with $k = \frac{m_n}{m_x}$. Since $k < 1$, only the + sign holds in this equation (for details see [15]). In general - even for a fixed energy of the incident neutrons - this leads to a continuous

recoil spectrum in the phonon detector up to a maximum energy $E_R(m_x)$. For the two preferred angles discussed above, the recoil energies are shown in table 6.1 for O, Ca and W.

Element	O	Ca	W
$E_R(80^\circ)$ [keV]	1095	450	99
$E_R(45^\circ)$ [keV]	412	164	35

Table 6.1: Calculated recoil energies for the two scattering angles $\Theta_{lab} = 45^\circ, 80^\circ$ for incident neutrons of 11MeV.

The assumptions and calculations made in this chapter are not restricted to 11MeV neutrons, but hold for neutrons of the whole energy range considered for this experiment (from ~ 1.5 to ~ 15 MeV).

6.3 Recoil Spectra of CaWO_4 at Fixed Scattering Angles

Since the neutron production process (described in section 7.1.3) not only produces ~ 11 MeV neutrons but also neutrons of lower energies, a continuous recoil-energy spectrum is expected, even if the scattering angle is fixed. In this section, the expected recoil rates at fixed scattering angles of the elements in CaWO_4 are calculated for the neutron spectrum of the beam.

A typical ToF spectrum of the neutrons obtained with the neutron detector positioned at 0° scattering angle is plotted in figure 9.1 (section 9.1). This plot can be transformed into an energy spectrum by calculating relativistically the kinetic energy E_{kin} from the time t the neutrons need to travel the distance s .

$$E_{kin} = m_0 c^2 \left(-1 + \sqrt{\frac{c^2}{c^2 - \frac{s^2}{t^2}}} \right) \quad (6.3)$$

The energy spectrum (see figure 9.2 in section 9.1) exhibits a peak at ~ 10.6 MeV and a continuous spectrum, that increases exponentially towards lower energies. The histogram has been fitted by an exponential and a Gaussian characterizing the peak, plotted as red (solid) line in figure 9.2. For energies below the threshold of the neutron detector, the exponential was extrapolated to zero energy.

The National Nuclear Data Center [38] provides cross-sections of nearly all isotopes and many types of interactions online. In this work, software to analyse this data format has been developed in the numerical computing environment MATLAB [39]. In the following only elastic neutron scattering on the three elements of CaWO_4 is considered. The angular distribution of the elastic neutron-scattering cross-section $f(\mu, E)$ is generally represented as a series of Legendre polynomial

$$f(\mu, E) = \sum_{i=0}^{NL} \frac{2i+1}{2} a_i(E) P_i(\mu) \quad (6.4)$$

where E is the energy of the incoming neutron, $\mu = \cos(\theta)$ the cosine of the scattering angle, P_l the Legendre polynomial of order l , a_l the Legendre coefficients of order l

and NL the number of Legendre coefficients. The Legendre coefficients are provided by ENDF and are given for a wide energy range (from $\sim 10\text{keV}$ up to $\sim 30\text{MeV}$). The differential cross-section $\frac{d\sigma}{d\Omega}$ can be calculated by

$$\frac{d\sigma}{d\Omega}(\mu, E) = \frac{1}{2\pi}\sigma(E)f(\mu, E) \quad (6.5)$$

where $\sigma(E)$ is the energy-dependent elastic cross-section for neutron scattering, which can also be obtained from the ENDF database. In figure 6.4 the differential cross-section for a scattering angle of $\theta = 80^\circ$ (laboratory frame) is plotted versus the incident neutron energy for the three elements in CaWO_4 . The stoichiometric conditions in CaWO_4 and the natural isotope ratio of tungsten are included in the calculations.

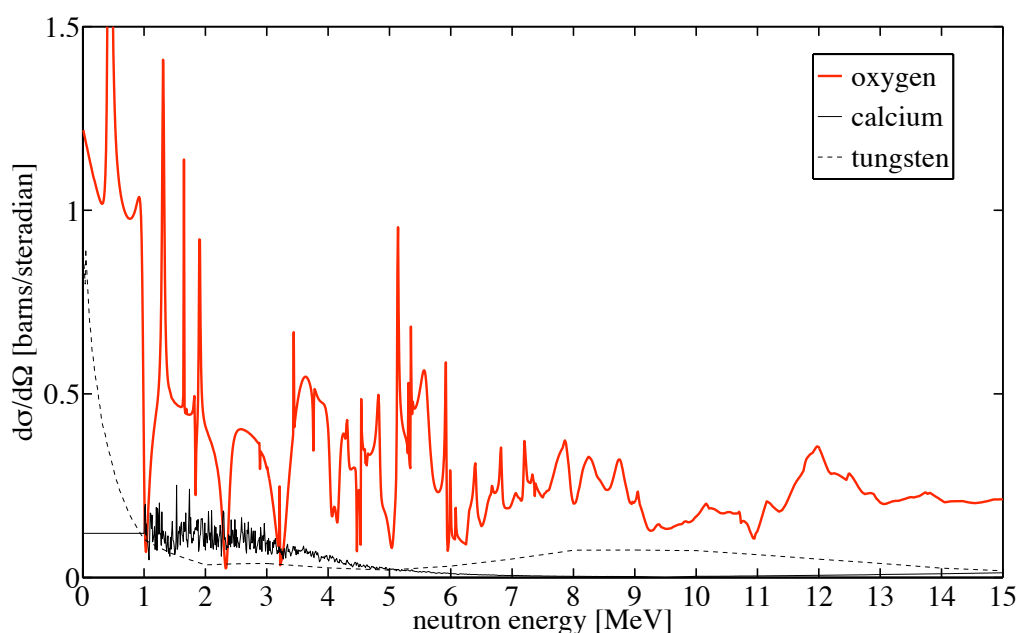


Figure 6.4: Differential elastic cross sections of O, Ca, and W plotted versus the energy of the incident neutrons for a scattering angle of 80° (laboratory frame). The stoichiometric conditions in CaWO_4 and the natural isotope ratio of tungsten are included.

In order to calculate the expected recoil rates in the CaWO_4 crystal, the differential elastic cross section (see equation 6.5) is convoluted with the measured neutron spectrum (see figure 9.2). Figure 6.5 shows the recoil rates of CaWO_4 obtained in this way.

The spectrum is dominated by oxygen over the whole energy range. Calcium is strongly suppressed at energies $> 5\text{MeV}$, whereas the recoil rates for tungsten show a broad local maximum at about 10 to 12 MeV. This is particularly important for the scattering experiment, since one wants to measure the QF of tungsten.

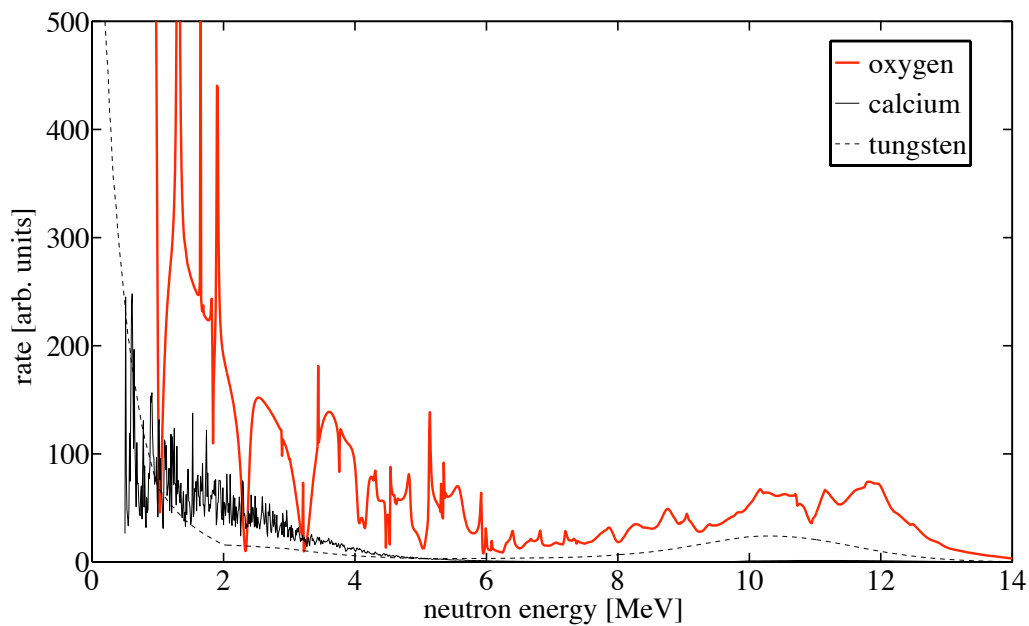


Figure 6.5: Expected recoil rates for O, Ca and W plotted versus the energy of the incident neutrons for a scattering angle of 80° (laboratory frame). The rates are calculated using the measured energy spectrum of the neutrons produced by the accelerator (see figure 9.2) and the calculated differential cross section (see equation 6.5). The stoichiometric conditions in CaWO_4 and the natural isotope ratio of tungsten are included.

Chapter 7

Experimental Setup

7.1 The MLL Accelerator as a Neutron Source

The neutron scattering facility is placed in Hall II at the accelerator of the MLL (Maier Leibnitz Laboratorium) in Garching. Figure 7.1 shows a top view of the accelerator facility. Several important components of this setup will be described in the following sections.

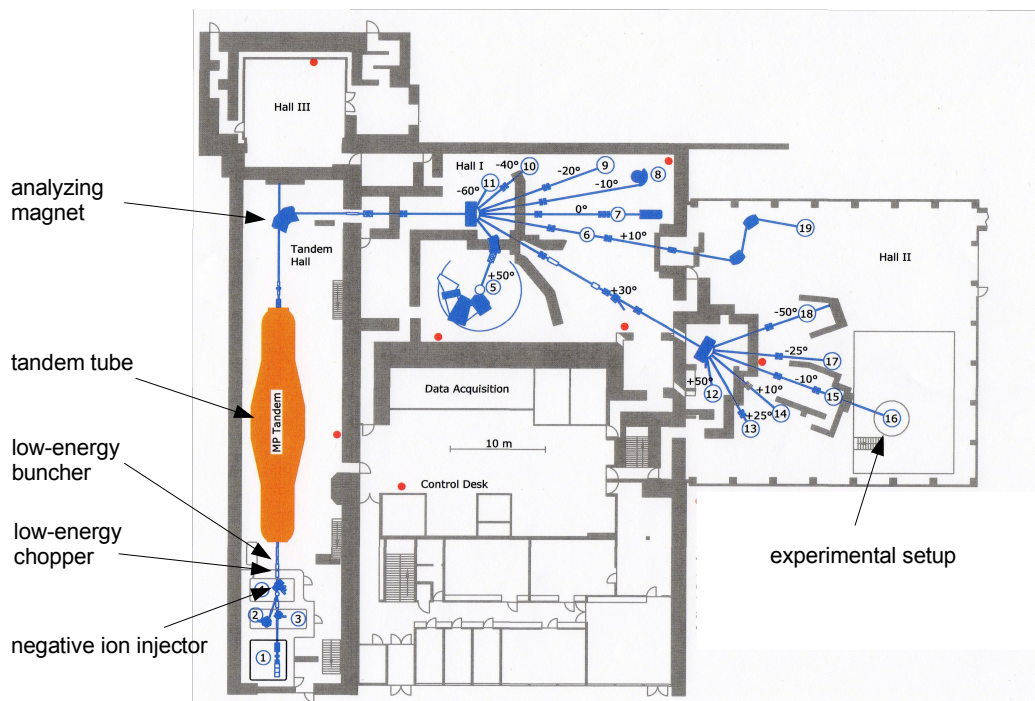


Figure 7.1: Top view of the MLL accelerator facility in Garching. Important components are indicated.

7.1.1 Ion Production and Acceleration

The accelerator laboratory is equipped with a negative-ion injector (figure 7.2) that allows to use a wide range of ions [40]. A solid cone-shaped source is placed in an evacuated vessel, where a heater produces neutral Cs vapour, which deposits on the surface of the source as well as on an ionizer. The ionizer is heated to 1400° and, by applying an electric voltage (U_2), Cs^+ ions are generated and finally sputtered onto the source. There they knock out target atoms (in our case ^{11}B) from the source. Since the ^{11}B atoms have to pass a few layers of evaporated neutral Cs atoms, they easily pick up an electron from the loosely bound outermost electron shell of the Cs atoms. In this manner B^- ions are produced and preaccelerated by the extraction voltage U_1 .

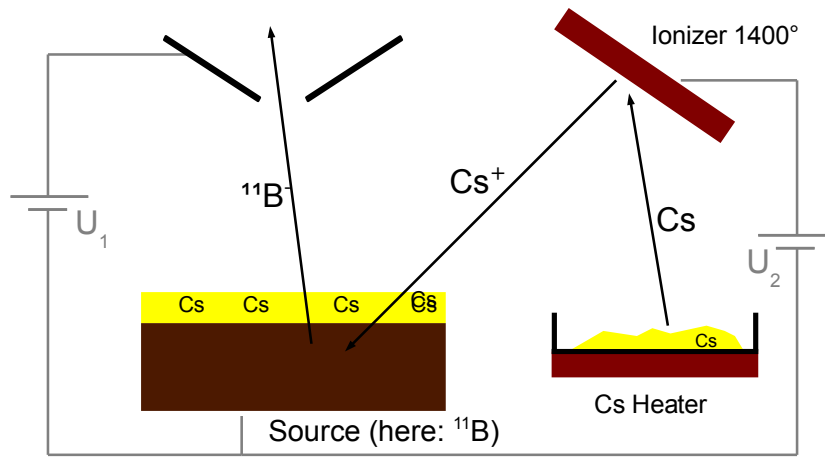


Figure 7.2: Working principle of the negative ion injector. Evaporated Cs atoms are ionized and sputtered onto a solid target, where they knock out negatively charged target ions (in our case ^{11}B). A more detailed description is given in the text.

After passing the low-energy pulsing devices (described in section 7.1.2) the beam is injected into the tandem accelerator tube, where the maximum accelerator voltage of 15MV can be used twice. Due to a stripper foil in the middle of the tank, electrons of the negative ions are stripped off and the generated positive ions traverse the same potential difference (15MV) again.

The beam usually consists of ions with different charge numbers and thus of miscellaneous energies. With the analyzing 90° magnet the desired energy and charge state (here $^{11}\text{B}^{+5}$, means that all electrons of ^{11}B are stripped off) can be selected and focused into the beamline in order to be guided to the experiment.

7.1.2 Pulsed Ion Beam

The Time-of-Flight (ToF) measurement requires extremely sharp bunches of the beam (width $\sim 2\text{-}3$ ns), for which different devices of the accelerator are used and need to be properly adjusted. The so-called Low-Energy Buncher is used to compress the continuous beam periodically into packages. This is achieved by a saw tooth voltage applied between the hollow buncher tubes, which enclose the beam. The principle is shown in figure 7.3.

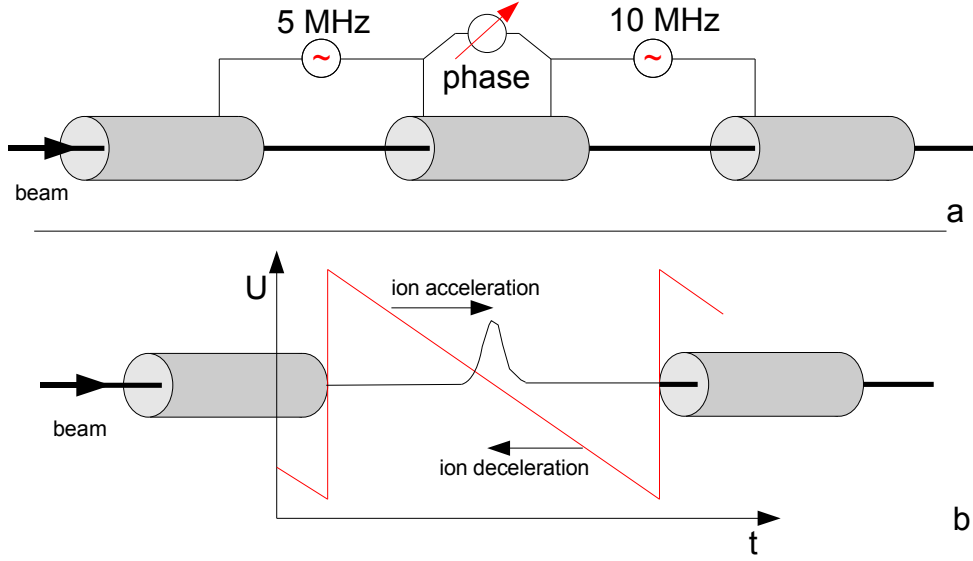


Figure 7.3: Scheme of the Low-Energy Buncher: (a) principle of the actually used setup with two applied sine-shaped voltages, (b) functional principle of an ideal saw tooth voltage (U) between the buncher tubes.

Applying a saw-tooth-voltage in the gap between the two tubes early arriving ions are decelerated, late arriving are accelerated, thus a periodic accumulation of ions is generated. Since a clean and stable saw-tooth voltage at the desired frequency of 5 MHz is difficult to generate, two sine waves of 5 MHz and 10 MHz, respectively, are applied at two separated gaps of the bunch tubes. By adjusting the phase between them one can obtain an approximately saw-tooth shaped voltage. Because of this approximation, along with a sharp peak periodically appearing every 100ns, a background intensity (± 20 ns around the peak) remains, which is depicted in figure 7.4a. For this reason a Low-Energy Chopper is installed in front of the Buncher, to cut away parts of the beam, before it reaches the Buncher. As shown in figure 7.5 the Chopper simply consists of a capacitor with an applied AC voltage, which wiggles the beam over an aperture. Regulating the amplitude of the voltage and the phase with respect to the buncher, the cut region (hatched area in figure 7.4a) can be adjusted at will. As can be seen in figure 7.4b, a pattern with sharp peaks remains. The buncher produces a logical signal for every bunch in order to have a timing information, that is required for the coincident measurement.

7.1.3 Neutron Production

To produce neutrons in the MeV regime, the reaction $p(^{11}\text{B},n)^{11}\text{C}$ was chosen [41]. This nuclear reaction takes place in a cell (inner diameter: $\sim 1\text{cm}$, length $\sim 3\text{cm}$) placed at the end flange of the beamline at a distance of $\sim 30\text{cm}$ from the cryodetector. The hydrogen gas at a pressure of 2bar in the cell is separated from the vacuum in the beamline by a $5\mu\text{m}$ thick molybdenum foil that can stand the pressure difference of 3bar and allows the high energetic ^{11}B beam to pass with an average energy loss of 4.9 MeV [15]. The hydrogen cell can be filled and evacuated by a system of transfer tubes. The energy of the ^{11}B beam is adjusted in such way that a maximum event rate is

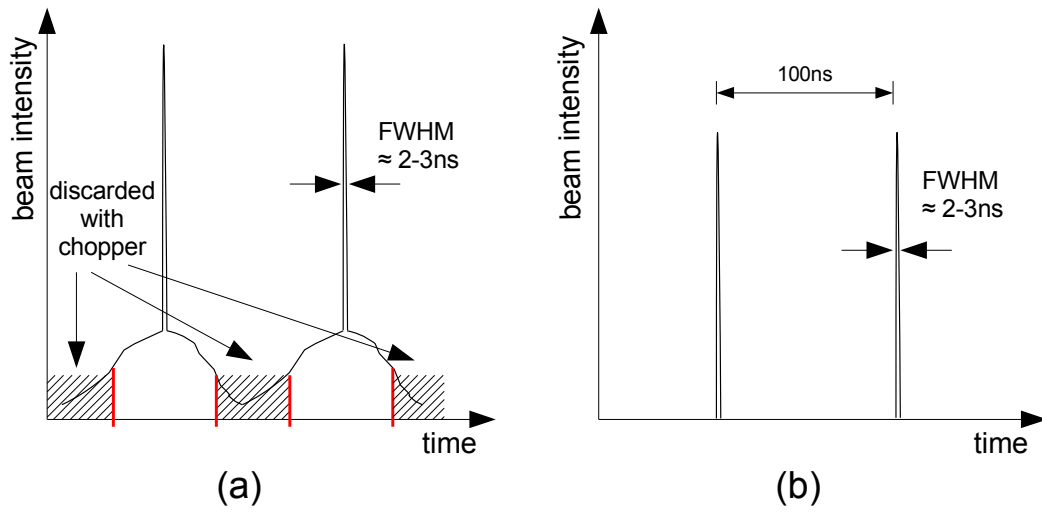


Figure 7.4: Schematics of typical beam structures. (a) shows a pattern using only the Buncher, whereas in figure (b) the Chopper/Buncher ensemble is turned on and properly adjusted. The hatched areas, confined by red vertical lines, indicate the part of the beam that is discarded by the Chopper.

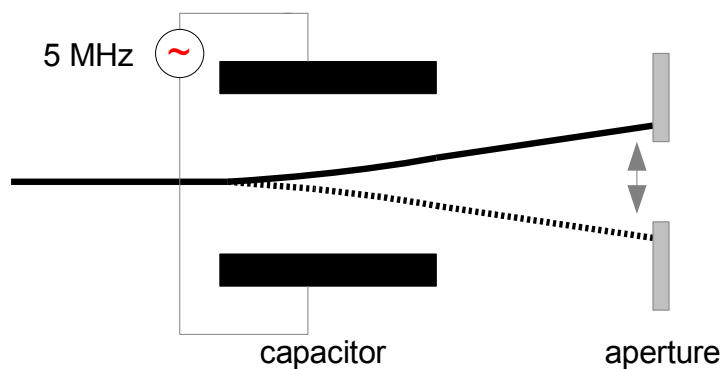


Figure 7.5: Working principle of the Low-Energy Chopper. An AC voltage is applied on the capacitor, that wiggles the beam over the aperture. More details are given in the text.

achieved without reaching the energy of the first excited state of the daughter nucleus (^{11}C), which would lead to lower-energy neutrons (figure 7.6). A ^{11}B beam of an energy of 55.4 MeV is found to be the optimal value, leading to a resonant production of 11MeV neutrons. Due to a large Center of Mass (CM) velocity the induced neutron beam is collimated in forward direction (inverse kinematics). Because not all ^{11}B ions are interacting with the H_2 gas, a Au beam-stop is installed at the end of the cell. Reactions in this gold disc produce a background of lower energetic neutrons, but for $^{197}_{79}\text{Au}$ this background has been shown to be smallest [42].

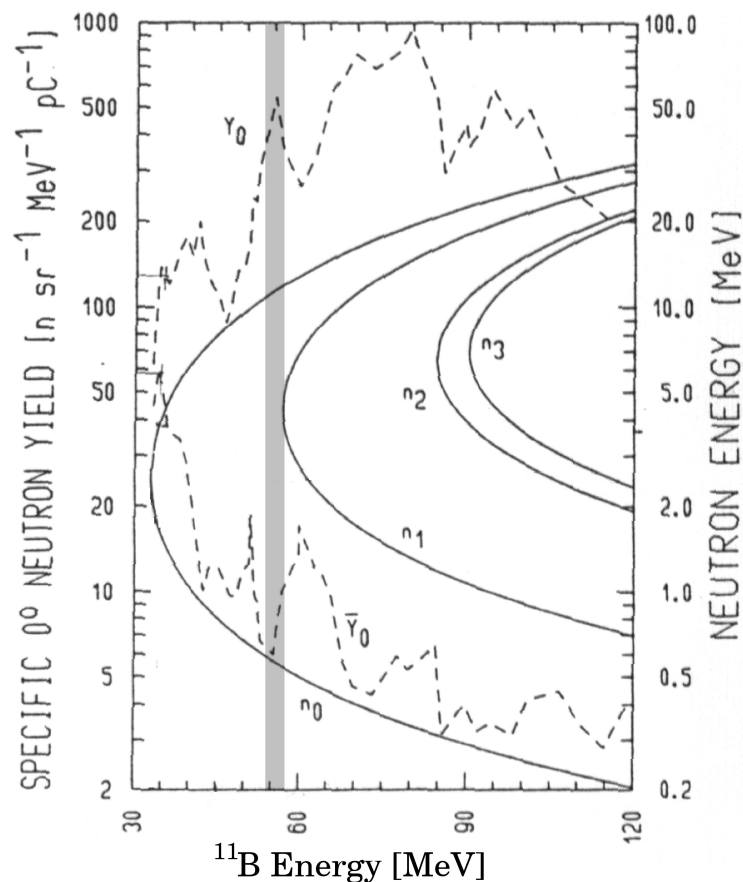


Figure 7.6: Specific 0° neutron yield and neutron energy versus the incident ^{11}B energy for the nuclear reaction $p(^{11}\text{B},n)^{11}\text{C}$. The grey vertical line indicates the ^{11}B energy used in this experiment (55.4MeV). n_0 indicates the line of elastic scattering, whereas n_1, n_2, \dots indicate the lines of inelastic scattering leading to the first, second excited state of ^{11}C . Y_0 and \bar{Y}_0 is the yield of the high-energy branch and the low-energy branch of the n_0 reaction, respectively [41].

The total acceleration voltage is stabilized at 10.2MV resulting in a beam energy of 61.5MeV while losses [15] in the Mo-window (4.8MeV) and the hydrogen cell itself (1.3MeV) lead to the desired resonance energy.

7.1.4 Mounting of the Cell and Beam-Monitoring System

During the commissioning beamtimes it appeared to be quite a challenge to hit the target cell properly, thus several mounting and monitoring devices have been installed within this work, both to stabilize the beam at the right position and to control the shape of the beam itself.

The end of the beamline was supported by a variable aluminium profile system (item®-profiles [43]) to avoid vibrations of the setup, for example, when filling the hydrogen cell. In order to check the shape of the beam at about one metre distance from the hydrogen cell, a removable quartz screen was installed. When hit by an ion beam, the quartz scintillates and thus reflects the actual beam shape. The screen is mounted together with a mirror, so that the scintillation light of the quartz can be observed through a glass window by a CCD camera (Figure 7.7a). The quartz/mirror ensemble can be moved in and out of the beam by a pneumatic lifter. Using the various quadrupole magnets in the beamline, the beam shape can be optimized, preferably to a circular shape. Elliptical beam shapes not only hit the hydrogen volume, but also the material surrounding it, leading to a parasitic neutron background.

At the hydrogen cell itself, two electrodes can be used to measure the current of the beam. Maximizing the current (figure 7.7b) on the Au beamstop while minimizing it on the ring-shaped aperture in front of the cell can be obtained by adjusting X and Y dipole magnets.

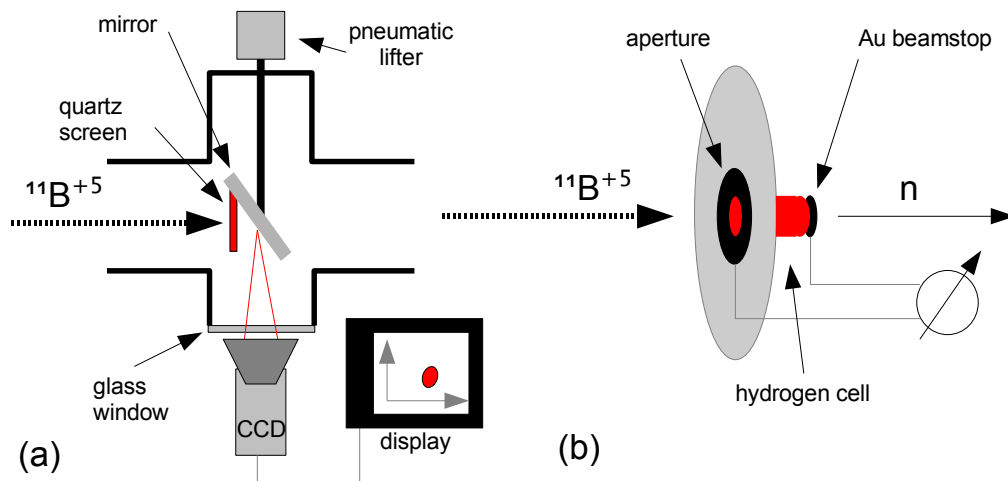


Figure 7.7: (a) The camera setup to monitor the ^{11}B beam. (b) Schematic view of the hydrogen cell with its electrodes (aperture, Au beamstop) to measure the beam current.

7.2 Cryogenic Setup

7.2.1 ^3He - ^4He Dilution Refrigerator

To cool the CRESST-like detector to its operating temperature of $\sim 20\text{mK}$ a ^3He - ^4He dilution refrigerator (KELVINOX400, cooling power of $400\mu\text{W}$ at 100mK) with a base temperature of $\sim 10\text{mK}$ is used [44]. Despite the complexity of this kind of refrigerator

and the big effort to install the cryostat in the beamline of the accelerator, it represents the most convenient way to obtain the required mK-temperatures and cooling power. In the following we will give a brief description of the working principle of a ^3He - ^4He dilution refrigerator, for further details see [45].

In order to obtain temperatures in the temperature regime $< 0.1\text{K}$, evaporation cooling that uses the latent heat of evaporation while pumping on a cryogenic liquid (e.g. ^3He , ^4He), is not sufficient. As can be seen in figure 7.8 a minimum temperature of $\sim 0.3\text{K}$ can be reached by reducing the vapour pressure of ^3He due to the exponential decrease of the cooling power ($Q \propto \exp -\frac{1}{T}$). Pumping on ^4He results in a limit of $\sim 1\text{K}$.

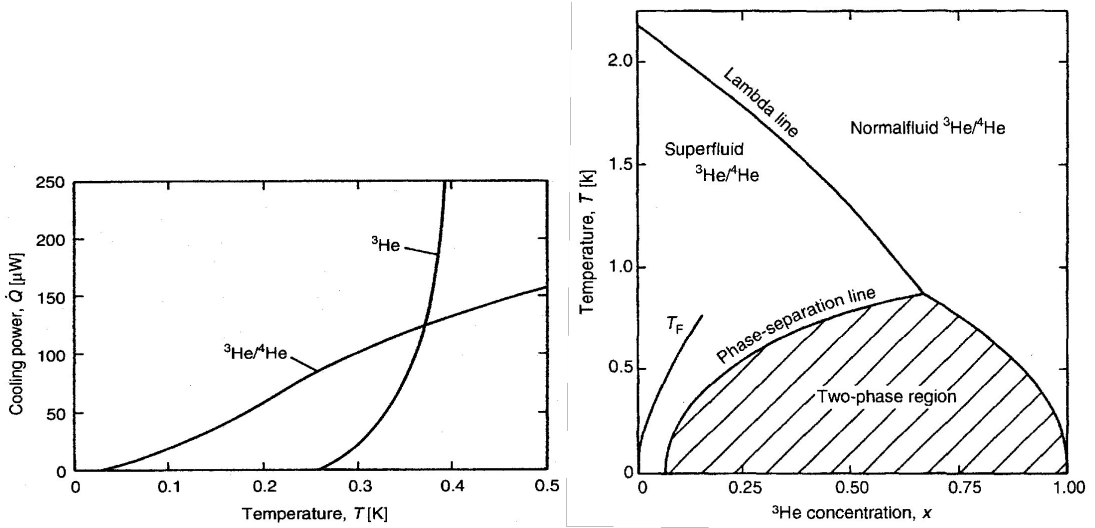


Figure 7.8: The left panel indicates the cooling power of the ^3He evaporation and the dilution cooling of a ^3He - ^4He mixture plotted against the temperature. The right plot shows the phase diagram of a ^3He - ^4He mixture at saturated vapour pressure. Below the lambda point ($T=0.867\text{K}$) the mixture separates into two phases. The finite solubility of ^3He in the mK range is of utmost importance to reach mK temperatures (see text) [45].

To reach even lower temperatures another cooling method is applied, namely the enthalpy of mixing two quantum liquids. This can be realized by using a mixture of ^3He and ^4He below its lambda point at $T=0.867\text{K}$, where the mixture separates into a ^3He -rich and a ^3He -poor phase (see figure 7.8). The finite solubility of ^3He in ^4He (6.6% @ $T=0\text{K}$) is crucial for the cooling mechanism. If ^3He is removed from the ^3He -poor phase, ^3He atoms will pass the phase boundary to maintain the minimum solubility. Since the enthalpy of ^3He in the dilute phase is larger than in the concentrated phase, each ^3He atom passing the phase boundary is cooling the system. As one can see in figure 7.8 left the temperature dependence of the cooling power is weaker and is maintained down to the mK range.

The technical solution of this cooling mechanism is shown in figure 7.9. Since a continuous cooling is required, the mixture is circulated in a closed cycle with pumps, that are placed outside the cryostat at room temperature. The mixture is precooled by a ^4He evaporation stage (the so-called 1K-pot), where the mixture condenses. The ^3He is continuously removed in the so-called still by pumping which as a welcome side-effect leads to the cooling of the system by ^3He -evaporation. The phase boundary occurs in

the mixing-chamber, the coldest part of the cryostat, to which the detector module is thermally coupled. Temperature differences between the downstreaming and upstreaming gas/liquid are compensated by heat exchangers.

Since the scattering experiment requires a minimum amount of material around the detector module to avoid parasitic neutron scattering, a dedicated slim He-dewar was designed and installed (see figure 7.15) [44].

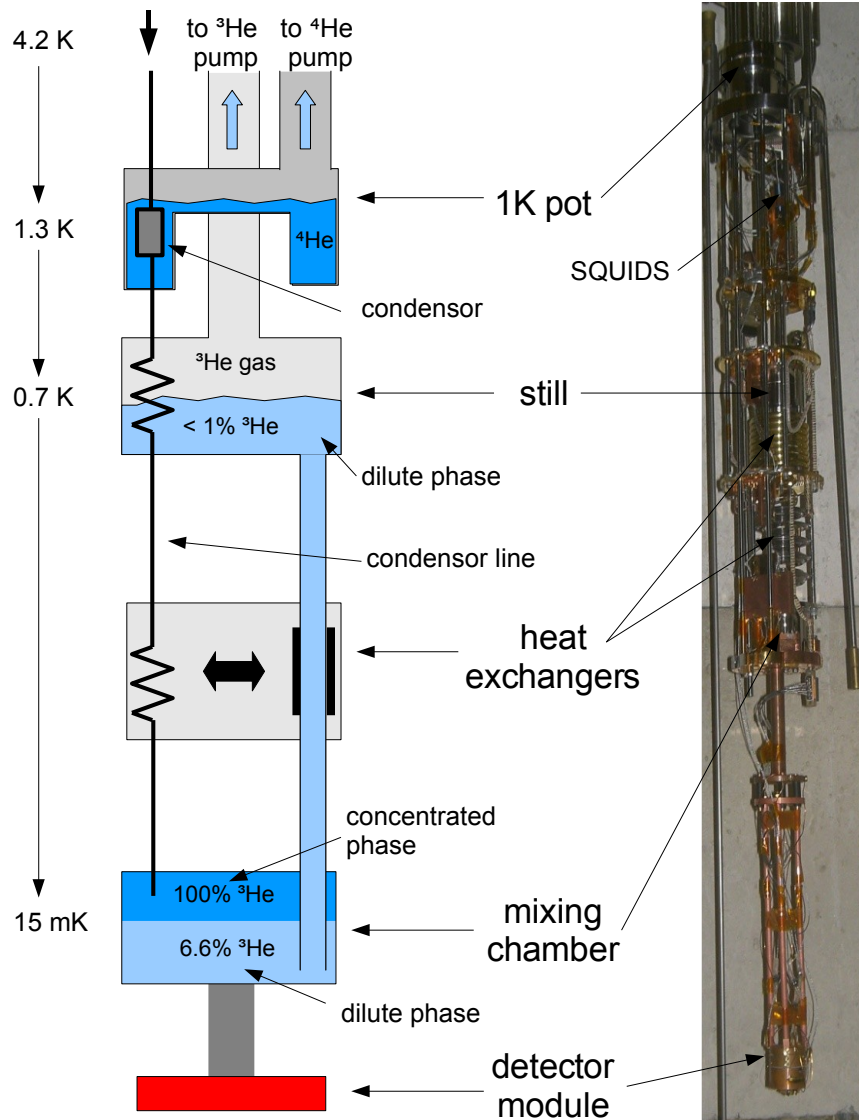


Figure 7.9: The main components of a ^3He - ^4He dilution refrigerator are shown schematically (left) and indicated on a picture of the cryostat used in this experiment (right). The working principle of a dilution refrigerator is explained in the text.

7.2.2 CRESST-like Detector Module

The central cryodetector module of the scattering experiment is built like a CRESST detector module, of which the working principle is described in section 2.1. A detector module consists of a phonon detector and a light detector.

The CRESST modules are designed for a low-background environment like in the Gran Sasso Laboratory and can stand a maximum rate of 0.5-1Hz, whereas the detector for the neutron scattering experiment on the earth's surface has to cope with much higher rates (tens of Hz).

For this reason a dedicated detector module (figure 7.10) with the following features was designed and developed in [35] and installed in [36].

- To reduce the overall event rate in the phonon detector, the dimensions of the cylindrical CaWO_4 crystal are 20mm in diameter and 5mm in height. In addition, this geometry achieves a low number of neutron double scatterings ($\sim 7\%$), which is important for the separation of the nuclear recoil bands of the three elements in CaWO_4 .
- An Ir-Au TES (Transition Edge Sensor) with a sharp transition curve (width $\sim 2\text{mK}$) at a temperature T_C of $\sim 60\text{mK}$ is directly evaporated onto the absorber crystal.
- The decay times of the pulses can be reduced to $\sim 2\text{ms}$ by increasing the surface of the TES. Unfortunately this increases the heat capacity of the TES, resulting in a lower pulse height, i.e., reduced sensitivity. As a compromise TES equipped with Al-phonon collectors, that are superconducting below 1.2K and thus have a vanishing heat capacity, are used to absorb phonons generated in the CaWO_4 crystal. More details are given in [35].
- The detectors are operated in the so-called electrothermal feedback mode to stabilize the detector via a change of the dissipated power of the bias current in the TES: After a particle interaction, the resistance of the TES is increased. This leads to a lower current in the TES and thus to a "cooling" of the detector. As a result the decay times of the pulses are reduced.
- The light detector consists of a 20mm x 20mm silicon crystal of thickness $525\mu\text{m}$. The Ir-Au TES is of the same kind as the one described above with a transition temperature of $T_C \approx 37\text{mK}$.

The detectors are mounted in a copper housing (wall thickness $\sim 5\text{mm}$), where the CaWO_4 crystal was initially held by teflon clamps. During commissioning tests of the detector, dark counts (events in the phonon detector, but not in the light detector) occurred, that were referred to lattice relaxations due to tensions caused by the clamps. Thus the upper teflon clamps were exchanged by weaker ones made of annealed CuSn_6 (bronze), what solved the dark-count problem [36].

On the bottom side of the CaWO_4 absorber crystal, the light detector is placed. The remaining parts of the holder are coated with a highly reflective foil to increase the light-collection efficiency.

A teflon ring thermally isolates the two detectors. Both are weakly coupled to the mixing chamber by Cu-wires. Together with heaters and thermometers (RuO_2) for each detector an independent temperature stabilisation of the two detectors can be maintained. The temperature regulation is achieved by two resistance bridge systems (Picowatt, AVS-47B), that operate the heaters via a PID controller.

The TESs of both channels are read out by two SQUIDs (Superconducting Quantum

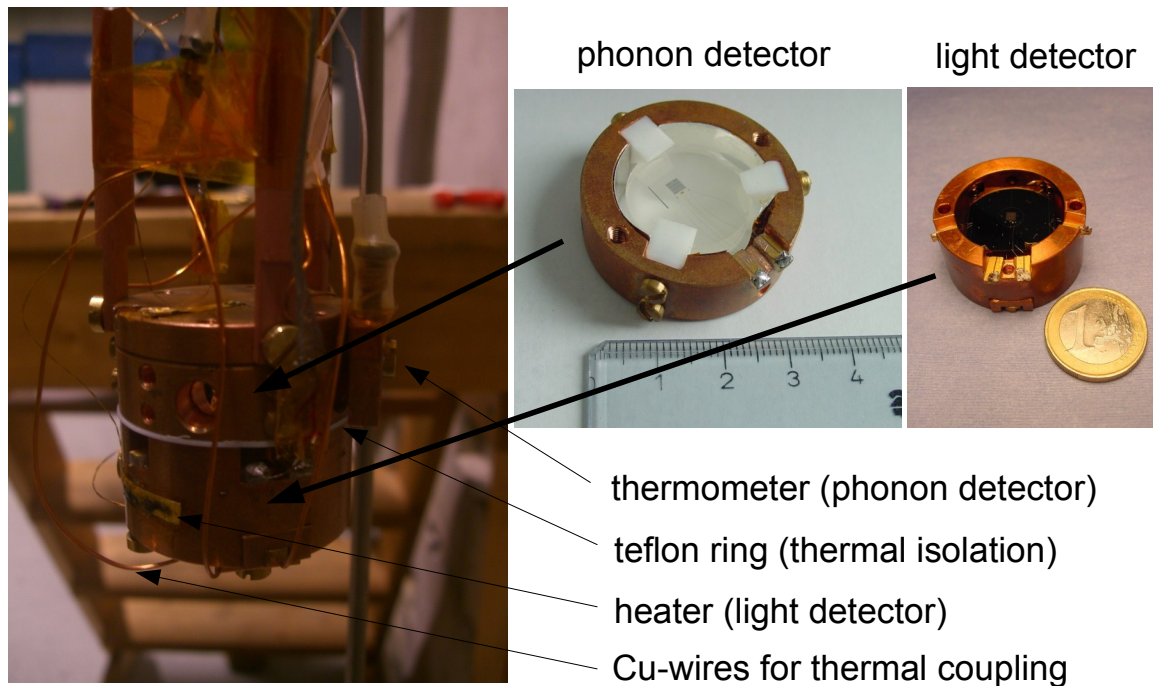


Figure 7.10: The pictures show the two detectors of the module for the scattering experiment, the phonon detector and the light detector, respectively. On the left side the detector module is mounted in the cryostat, where both detectors are independently coupled to the mixing chamber with Cu-wires and thermally decoupled in-between with a teflon ring. Both detector holders are equipped with separate heaters and thermometers to stabilise the temperature separately.

Interference Device), thermally coupled to the 1K pot (figure 7.9). For details concerning the SQUID system see [36].

For the energy calibration of the light detector, a ^{55}Fe source is mounted below the light detector (not present in figure 7.10). It is enclosed by a copper box of wall thickness 3mm. Through a hole of $\sim 1\text{mm}$ in diameter at the top of the box, the light detector is irradiated by X-rays from the source. The hole in the box is covered by an aluminium foil of thickness $\sim 0.015\text{mm}$, hence the Al-fluorescence photons, induced by X-rays from the ^{55}Fe source can be additionally used for calibration. The X-ray emission does not affect the CaWO_4 crystal and thus the phonon detector, since the ^{55}Fe source is mounted below the light detector.

Details on the calibration process of the light and phonon detector are given in section 7.3.5.

7.3 Neutron Detectors

In order to detect the neutrons scattered off the central detector module, 34 neutron detectors are placed at certain scattering angles around it. Photomultiplier tubes (PMTs) collect light from a special organic scintillator, that allows to distinguish neutrons from gammas via Pulse Shape Discrimination (PSD).

To avoid direct neutron events, polyethylen shieldings are placed between neutron detectors and hydrogen cell (see figure 7.15).

7.3.1 Organic Liquid Scintillators

Scintillation Mechanism

In this section a brief introduction to some important properties of organic liquid scintillators with focus on PSD is given, further details can be found in [46] [31]. For the detection of charged particles, materials with the property of luminescence can be used. If charged particles cross such materials, they interact electromagnetically with the molecules in the scintillator leading to excitation or ionization. In liquid organic scintillators the deexcitation of π -state electrons of benzene-like molecules produces photons in the visible or ultraviolet range, which can be detected by PMTs. In figure 7.11 the orbital structure of such ring-shaped hydrocarbon molecules is shown together with a diagram of the energy levels of the π -orbital system. Depending on the relative spin

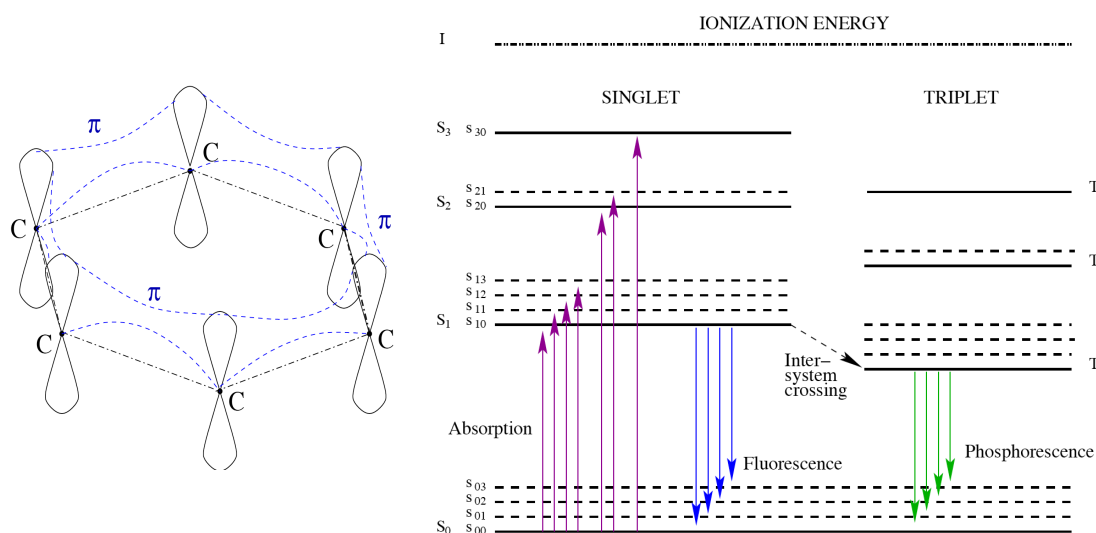


Figure 7.11: The diagram on the left side shows a ring-shaped benzene molecule. The full (black) lines indicate the p_z orbitals of carbon and the dashed (blue) lines the molecular π orbitals. The diagram on the right shows the energy levels of a typical π -orbital with singlet (S_0, S_1, \dots) and triplet (T_1, T_2) states. The energy spacings between the electronic levels are between 2 and 4.5eV. S_{00}, S_{01} etc. indicate vibrational sub-levels [46].

orientation of the two electrons in a molecular orbital, singlet ($S_0, S_1, S_2 \dots$) or triplet (T_1, T_2, \dots) states are excited. Since transitions between triplet and singlet states are highly forbidden due to selection rules (phosphorescence, decay times $\sim 10^{-6}$ s), most of the energy is dissipated via fluorescence light emission (decay times $\sim 10^{-9}$ - 10^{-8} s) from excited singlet states to the ground state (S_0). Triplet states can be populated indirectly when two ionized molecules recombine, Thus the density of populated triplet states is proportional to the density of ionized molecules. Because transitions of the kind T_i - S_0 are forbidden, most of the triplet states are depopulated by intermolecular interactions, which results in delayed fluorescence compared to the direct emission [46].

Since the emission spectrum of a scintillator overlaps with its own absorption spectrum,

often a second organic component, a so-called wavelength-shifter is added in small concentration ($\mathcal{O}(1\%)$). Those molecules absorb photons emitted by the scintillator and reemit at longer wavelengths. As a consequence this energy is not sufficient to excite the primary component. It becomes transparent and this light can reach the photocathode of the PMT. In addition, the wavelength is shifted towards the region, where common photocathodes of PMTs have their maximum sensitivity.

Pulse Shape Discrimination (PSD)

Since heavier and slower particles in comparison to fast electrons have a larger energy deposition per unit length $\frac{dE}{dx}$ in the scintillator material and thus a higher ionization rate, they have a higher fraction of delayed fluorescence, as mentioned above. This has an impact on the longer components of pulse-decay times. As a consequence, different particles can be distinguished by their pulse shape. Figure 7.12 qualitatively shows pulses of alpha particles, fast neutrons (proton recoils) and gamma rays for comparison.

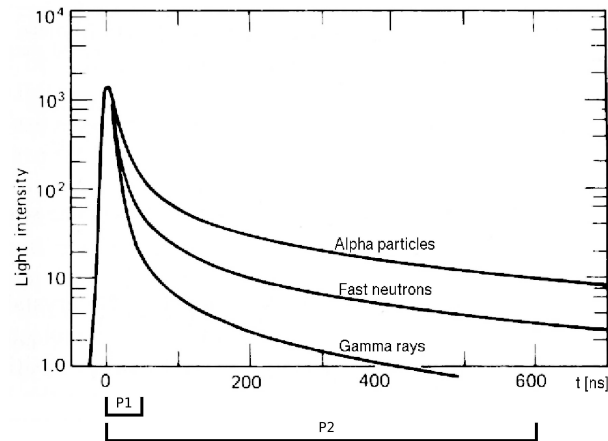


Figure 7.12: Pulse shapes of different particles are shown qualitatively. P1 and P2 indicate integration gates, that are applied from 0 to 50ns (short gate) and 0 to 600ns (long gate), respectively [32].

The pulse can be integrated over different time intervals. Typically, two so-called integration gates are applied, one short (~ 50 ns) and one long (~ 500 ns). This is sufficient to distinguish between different particles (in our case: neutrons and gammas). The long integration gate contains enough information to identify the incoming particles down to a certain energy, where the bands overlap due to the signal-to-noise ratio. This is shown in figure 7.13.

7.3.2 Design of the neutron detectors

The neutron detectors consist of a hexagonal Al container for the liquid scintillator. The inner diameter is ~ 9.1 cm and the height is ~ 5 cm (figure 7.14). A Philips XP-3461-B photomultiplier is optically coupled to the perspex window of the container with silicone oil, which has nearly the same refraction index as the window. The alkali

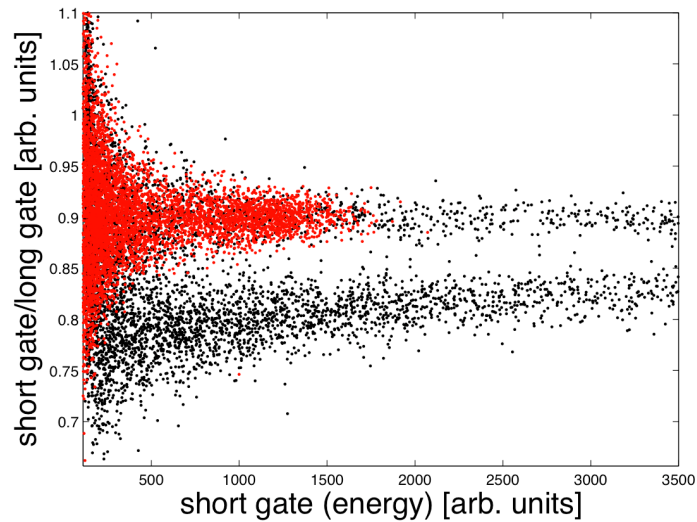


Figure 7.13: The ratio of the integrated pulse signals of the short and the long integration gate is plotted versus the short gate, which is a measure for the deposited energy. The black dots indicate events from an AmBe neutron source, whereas the red dots indicate events from a Na22 gamma source. The upper population represents the gamma band, whereas the lower band originates from neutron-induced protons. The measurement was performed as a proof of principle with the setup described in section 7.3.2.

photocathode of the PMT has a diameter of 76mm. The time resolution of the PMT ranges from 2 to 3ns. The PMT tubes are operated with a negative voltage of -1900V. The whole detector weights about 2.5 kg and is enclosed in a PVC tube. Currently 34 PMTs of this type are installed and working in our setup.

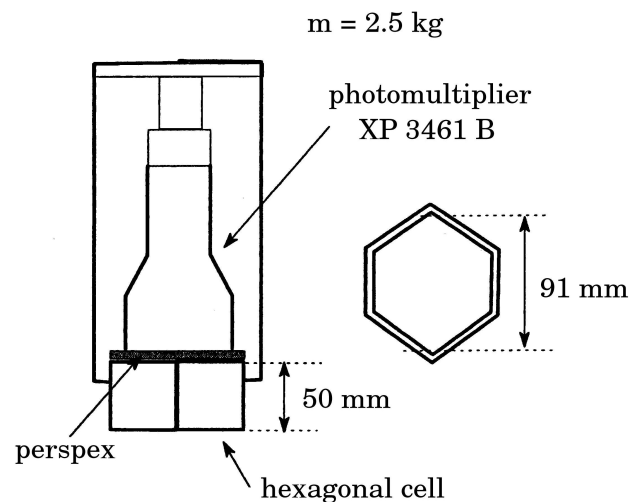


Figure 7.14: Schematic diagram of the neutron detectors used in the Scattering Experiment. The PMTs were constructed and first used by the SICANE team [47] in Lyon, France. Later they were shipped to Munich.

7.3.3 Construction of a new Mounting System

In this work, the mounting system of the whole experimental setup was replaced by a new, more variable system consisting of Al profiles (commercially available from [43]). This provides high stability of the mounted devices (neutron-detectors, beam-line, polyethylen shieldings) and allows quick changes of the experimental setup (e.g. change of the scattering angle). Figure 7.15 shows the present experimental setup from different perspectives.

7.3.4 Filling with New Liquid Scintillator

The manufacturer Nuclear Enterprise, Ltd. (NE) developed an organic liquid scintillator (called NE213) with excellent neutron-gamma discrimination properties. The neutron detector were originally equipped with this scintillator. Unfortunately, after some time ($\mathcal{O}(10y)$) the PSD performance and the light output degraded due to oxygen that leads to a destruction of the benzene-like structures.

In this work, the old scintillator was replaced by the EJ-301 scintillator in principle identical to NE213 but now produced by Eljen Technology [48], USA. The most important properties of this liquid scintillator are summarized in figure 7.16, whereas its main ingredients are displayed and briefly characterized in figure 7.17.

Before being filled into the PMT cells, the liquid scintillator has to be deoxygenated by sparging with pure nitrogen ($\sim 10h$ for one litre), because contact with oxygen deteriorates the benzene-like structures and thus reduces the scintillation efficiency. With the setup shown in figure 7.18 the scintillator can be filled into the PMT cells without having contact to oxygen. After the filling process the cells are sealed with clamped teflon (PTFE) tubes, since teflon resists the aggressive organic scintillator.

7.3.5 Calibration and Discrimination threshold

Energy Calibration

To characterise different scintillators an energy calibration was carried out, by irradiating the samples with gammas from different sources. Due to the low Z -value of the ingredients of organic liquid scintillators, no photo-peaks are visible and thus Compton edges are used to realize an energy calibration. The energy E of a Compton-scattered electron is given by

$$E(\Theta, E_\gamma) = E_\gamma - \frac{E_\gamma}{1 + \frac{E_\gamma}{m_e c^2} (1 - \cos \Theta)} \quad (7.1)$$

where E_γ is the incoming gamma energy, m_e the electron mass and Θ the scattering angle. The maximum energy E_{CE} transferred to the electron is achieved by backscattering of the photon and becomes visible as the Compton Edge in the spectrum, where the pulse height in the PMT is plotted versus the event rate (figure 7.19, left). E_{CE} is given by

$$E_{CE} = \frac{E_\gamma}{1 + \frac{m_e c^2}{2E_\gamma}} \quad (7.2)$$

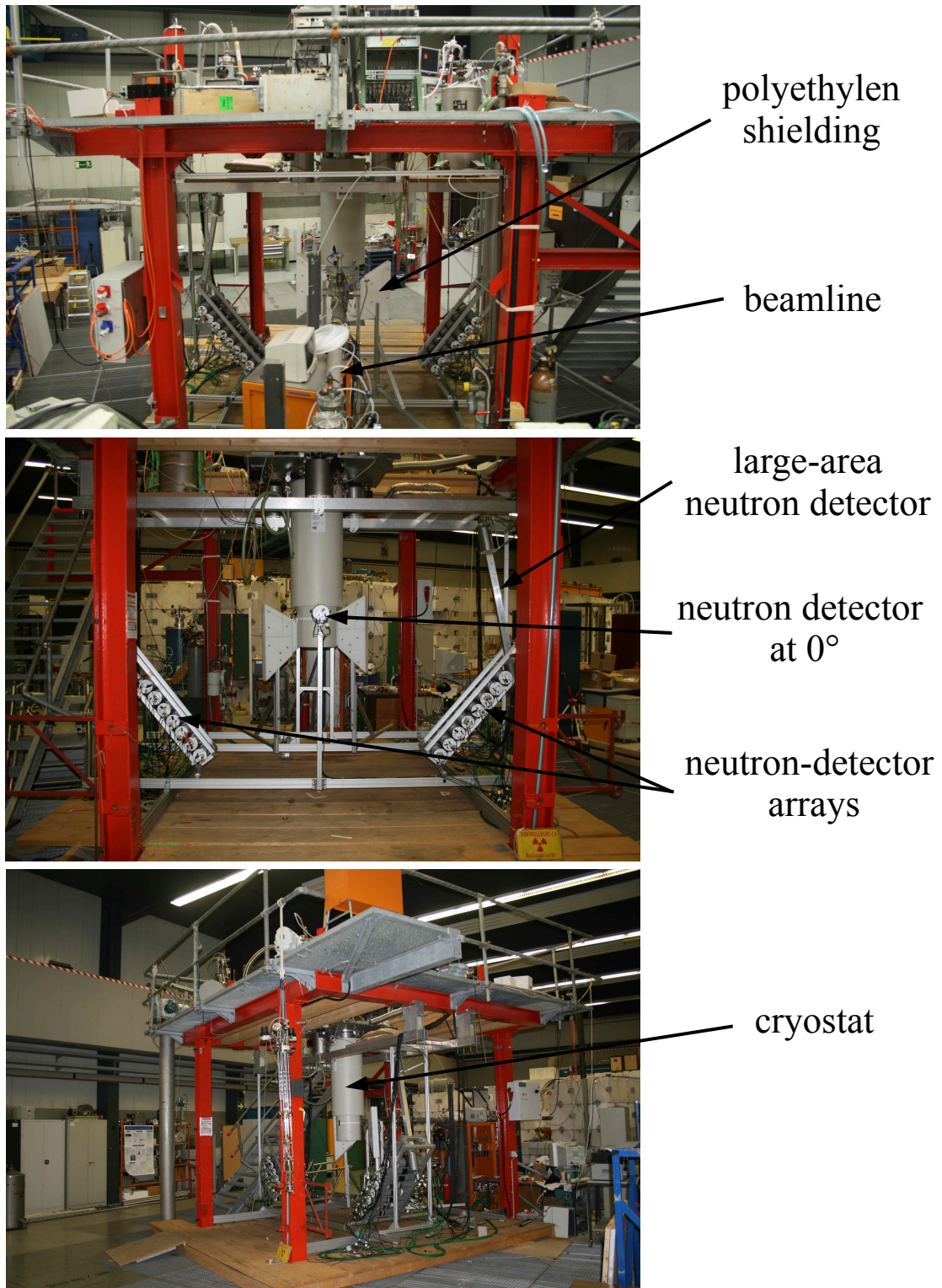


Figure 7.15: Experimental setup from different perspectives (Top: from the beamline, middle: from opposite of the beamline, bottom: side view). The gas-handling system of the dilution refrigerator and parts of the electronics are located on top of the setup.

PROPERTIES

Light Output (% Anthracene)	78%
No. of Blue Photons per 1 MeV of Electron Energy	12,000
Wavelength of Maximum Emission	425 nm
Specific Gravity	0.874
Atomic Ratio, H:C	1.212
No. of C Atoms per cm^3	3.98×10^{22}
No. of H Atoms per cm^3	4.82×10^{22}
No. of Electrons per cm^3	2.27×10^{23}
Flash Point (T.O.C.)	26°C (79°F)
Refractive Index, n_D	1.505

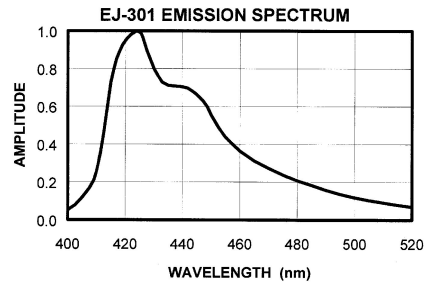


Figure 7.16: Properties of the EJ-301 organic liquid scintillator (identical to the widely used NE-213). On the right side the emission spectrum of the scintillator is shown [48].

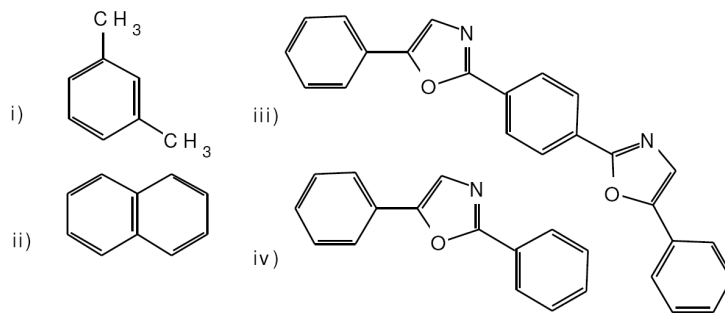


Figure 7.17: Structure formulas of the main ingredients of EJ-301 (NE213) [15]. It consists of the organic scintillator naphthalene (ii) which is dissolved in 1,3-Dimethylbenzene (i); this primary component emits photons at $\lambda \sim 340\text{nm}$. Two wavelength-shifters, POPOP (iii) and PPO (2,5-Diphenyloxazole) (iv) are used to achieve the emission spectrum as shown in figure 7.16.

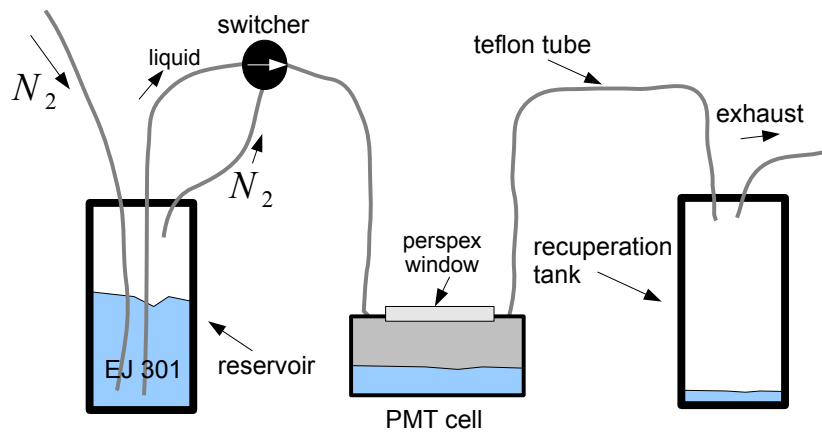


Figure 7.18: Filling setup for the PMT cells. In the reservoir the scintillator can be deoxygenated by sparging with pure nitrogen. Afterwards the liquid can be pressed into the cell with nitrogen. When the cell is filled completely, it is sealed with clamped teflon tubes.

In table 7.1 the gamma energies of different sources used in this work are listed along with the respective energies of the Compton Edge.

source	process	branching	half-life[y]	E_γ [keV]	E_{CE} [keV]
^{22}Na	β^-/EC	100%	2.6	1275	1062
^{22}Na	e^+e^- annihilation	90%	2.6	511	341
^{137}Cs	β^-	85%	30	662	478

Table 7.1: Gamma sources used in this measurement with their respective gamma energies E_γ [15] and the energy of the Compton Edge E_{CE} .

Due to the finite resolution of the detector, the exact fit function for the Compton spectrum is the convolution of a Gaussian (detector resolution) and a distribution described by equation 7.1. To characterize the scintillators in their discrimination capability, the following procedure is sufficient: A Gaussian fit is applied to the high-energy part and the Compton edge is assigned to the point a_{CE} where the spectrum has decreased to half of the maximum (towards higher pulse heights) [49] [15]. In figure 7.19 left, the spectrum of the scintillator LAB+10 $^{\frac{g}{l}}$ PPO (see section 7.3.6) calibrated with ^{22}Na and ^{137}Cs sources is shown together with the Compton edges fitted by Gaussians. Assuming a linear detector response [32], the calibration factor f can be obtained by a linear fit to the calibration points $(E_{CE}, a_{CE})_i$

$$E = a \cdot \frac{E_{CE}}{a_{CE}} = a \cdot f \quad (7.3)$$

where a is the pulse height and E the energy deposited in the scintillator. Figure 7.19 (right) shows that the linear fit (here for the scintillator LAB+10 $^{\frac{g}{l}}$ PPO) is in good agreement with the assumptions made above. The error of the fit is assumed to be the total calibration error.

Determination of the Discrimination Threshold

The energy, above which electron and nuclear recoil events can be distinguished (here at a 2σ confidence level), is referred to as the discrimination threshold (DT) of a scintillator.

To determine the DTs of organic liquid scintillators, the following steps are taken:

- From a scatter plot like that shown in figure 7.22, where the ratio of the event rates in the short and long integration gate is plotted against the deposited energy, an energy interval of $\sim 100\text{keV}$ in width is chosen.
- The ratio of these events can then be plotted in a histogram, where two distributions due to electron and nuclear recoils are visible.
- The two populations in the histogram are fitted by two Gaussians (figure 7.20 right). A 2σ -discrimination is possible, if the distributions do not overlap on a 2σ -level.

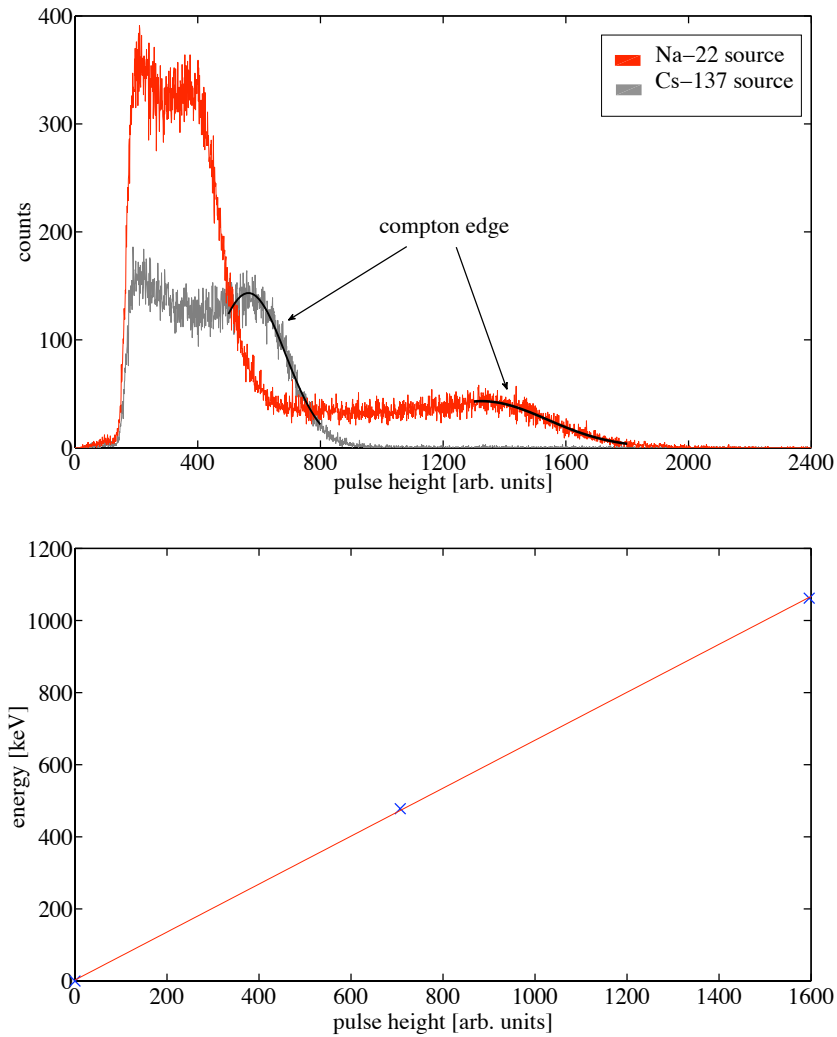


Figure 7.19: Top: Pulse-height spectrum of the scintillator LAB+10₁^gPPO irradiated with the ²²Na and ¹³⁷Cs gamma sources. The black lines indicate the Compton edges fitted by Gaussians. Bottom: The calibration points obtained from the Compton edges of ¹³⁷Cs ($E_{CE} = 478\text{keV}$) and ²²Na ($E_{CE} = 1062\text{keV}$) are plotted together with a linear fit.

Starting at high energies ($\sim 3\text{MeV}$) this fitting procedure is repeated shifting the 100keV energy interval to lower energies (steps of $\sim 50\text{keV}$). In each step the 2σ -points of the two Gaussians (marked in figure 7.20 right) are recorded. In figure 7.20 (left) these points are plotted versus the energy and the discrimination threshold can be obtained by the crossing points of the two curves.

7.3.6 Tests with Different Liquid Scintillators

With the method described in section 7.3.5, 6 different scintillators were tested. Along with EJ-301 (NE213) [48], that is now used in the Neutron Scattering Experiment and NE-343, another commercially available scintillator, the scintillators LAB and PXE (figure 7.21) with different concentrations of the wavelengthshifter PPO ($2\frac{\text{g}}{\text{l}}$, $10\frac{\text{g}}{\text{l}}$) are tested. The mixtures are produced at our institute, for further properties of the scintillators see [46].

The measurements were made at the MLL accelerator in Garching with the setup described previously in this chapter. The different scintillators that were investigated were filled using the method described in section 7.3.4. The samples were irradiated by an AmBe neutron source [15].

scintillator	discrimination threshold	light output
EJ-301 (NE-213)	$(111\pm 20)\text{keV}$	100%
LAB+ $10\frac{\text{g}}{\text{l}}$ PPO	$(732\pm 80)\text{keV}$	$(72\pm 6)\%$
LAB+ $2\frac{\text{g}}{\text{l}}$ PPO	$(1201\pm 132)\text{keV}$	$(74\pm 7)\%$
PXE+ $10\frac{\text{g}}{\text{l}}$ PPO	$(304\pm 33)\text{keV}$	$(90\pm 9)\%$
PXE+ $2\frac{\text{g}}{\text{l}}$ PPO	-	$(71\pm 6)\%$
NE-343	$(614\pm 67)\text{keV}$	$(80\pm 8)\%$

Table 7.2: Discrimination threshold and relative light output for different scintillators obtained with the method described in section 7.3.5. The light output is normalized to that of EJ-301.

In figure 7.22 the scatter plots of the tested scintillators are shown and the corresponding discrimination thresholds and relative light output of the scintillators are listed in table 7.2.

Since EJ-301 (NE-213) has the lowest threshold and the highest light output it was chosen as scintillator for our neutron detectors. Nevertheless, PXE+ $10\frac{\text{g}}{\text{l}}$ PPO shows promising properties and due to its much lower cost (factor ~ 10) it could be a solution for detectors, requiring a larger amount of scintillator (i.e. section 7.4).

Data from these measurements was also used in [50] to investigate discrimination properties of scintillators for the future large scale neutrino experiment LENA (Low Energy Neutrino Astronomy).

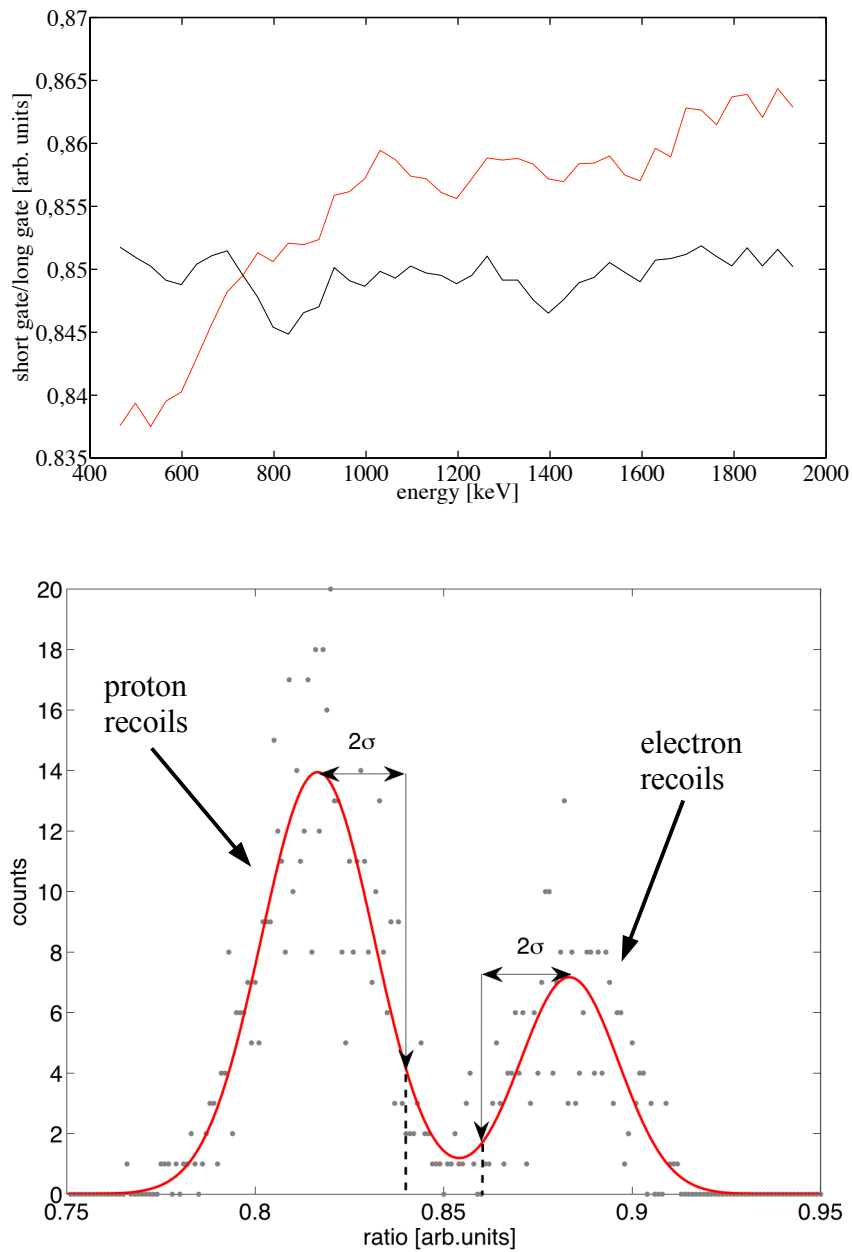


Figure 7.20: Bottom: The ratio of the event rates of the short and long integration gates (ratio) from events of an interval of $\sim 100\text{keV}$ around a definite energy ($\sim 1400\text{keV}$) is plotted in a histogram (grey dots). The solid line indicates the two Gaussians fitted to the spectrum. The dashed lines mark the 2σ -points of the two Gaussians. Top: The 2σ -points obtained at different energies are plotted versus the energy. The discrimination threshold is obtained by the crossing point of the two lines. In this case the threshold is at 732keV (LAB+ $10\frac{5}{1}\text{PPO}$).

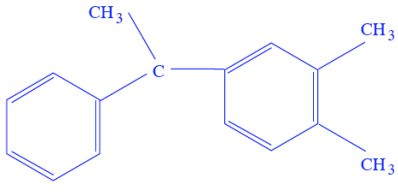
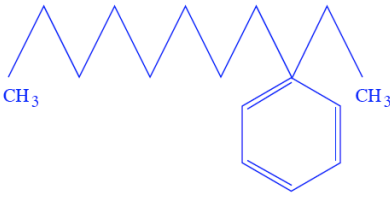
Solvent	phenyl-o-xylylethan	linear-alkyl-benzene
Short name	PXE	LAB
		
Formula	$C_{16}H_{18}$	$C_9H_{12} + (CH_2)_m \quad m = 7 - 10$
Density	0.986 kg/ ℓ	0.863 kg/ ℓ
Absorption	270 nm	260 nm
Emission	290 nm	283 nm
CAS-number	6196-95-8	68890-99-3
Company	PXE Dixie [102]	Petresa [103]

Figure 7.21: Main properties of the scintillators PXE and LAB [46].

7.4 "Grossmaul" Detector

In order to increase the detection area for the scattered neutrons a new kind of detector was developed in this work.

7.4.1 Design and Properties

The ordinary neutron detectors used for the scattering experiment consist of small cells filled with liquid organic scintillator ($\sim 0.3l$) optically coupled to a photomultiplier (PMT), as described in section 7.3. In order to increase the detection area per read-out channel, a new detector design was chosen. This large-area detector (for historical reasons called "Grossmaul" detector) consists of a quadratic tube (side length 6cm) of 1m length made of 2mm thick Al, which is filled with 3.6l of EJ301 (NE213) liquid scintillator. EJ301 has the lowest discrimination threshold among the tested scintillators (see section 7.3.6) and thus the best neutron/gamma discrimination capability. The tube is sealed at each end by glass windows and custom-built teflon-coated o-rings, that resist the aggressive liquid scintillator. For a backup sealing, the glass windows, in addition, are fastened to the Al-flange at both ends of the tube by a two-component glue (UHU endfest 3000). The PMTs (Philips XP-3461-B) are optically coupled to the glass windows by silicone oil. Each PMT is enclosed by Mu-metal (to avoid magnetical disturbances) inside a light-tight housing made of steel. The PMT-tube is softly pressed onto the glass window by a spring to ensure a sufficient optical coupling. The inner walls of the tube are covered with reflective Al plates (1mm thick, reflectivity $\sim 90\%$) in order to guide the light to the glass windows at the tube's ends. In figure 7.23(left) a schematic view of the setup is shown. The large-area detector has been integrated into the setup of the mounting system made of Al-profiles (see section 7.3.3). In figure 7.23(right) one side-detector array is shown together with the prototype of the "Grossmaul"-detector.

The detector is mounted, so that the whole tube is at a scattering angle of $\sim 80^\circ$ with a maximal uncertainty of $\pm 1^\circ$. Hence no determination of the event position in the

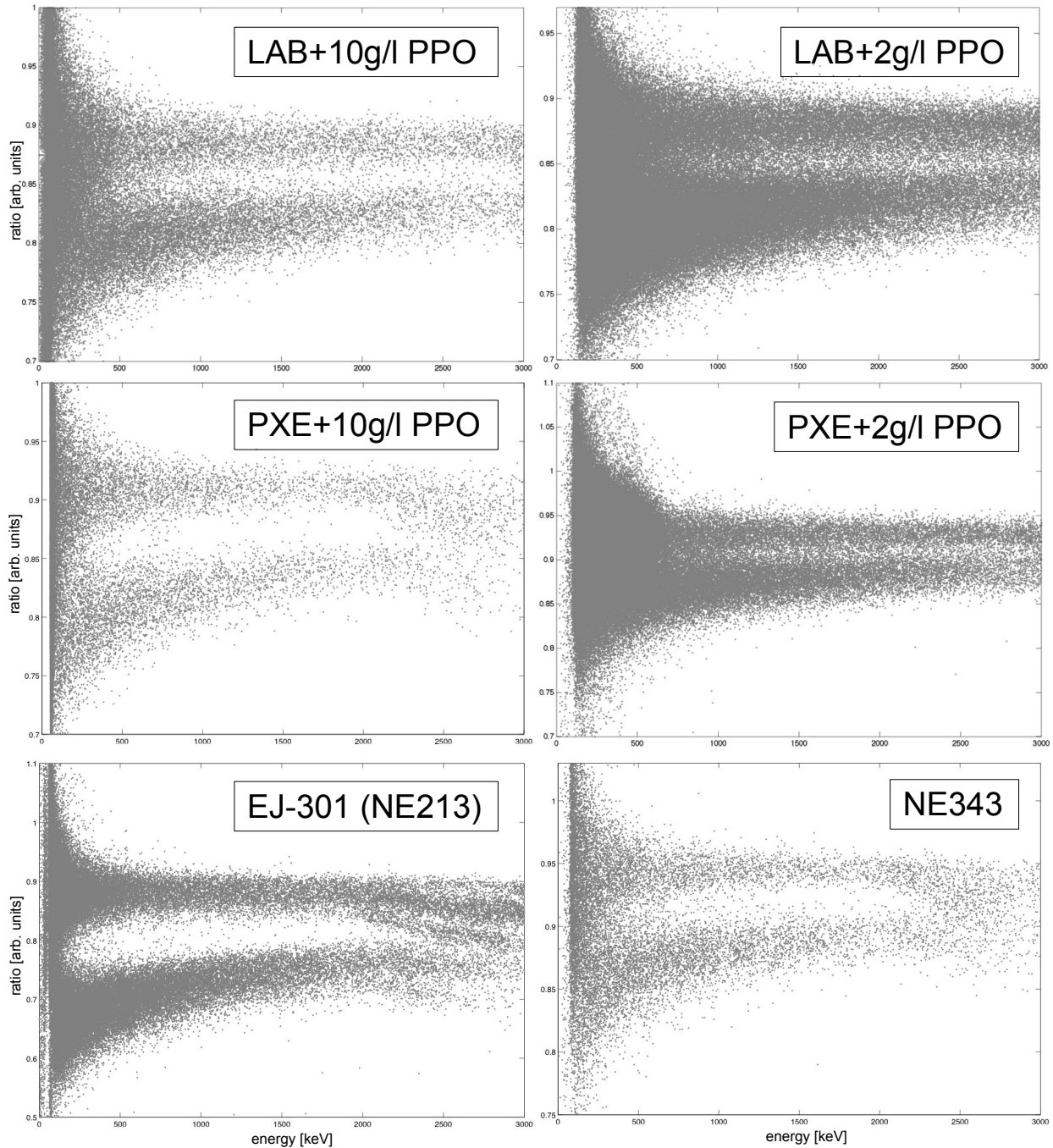


Figure 7.22: Scatter plots of different organic liquid scintillators irradiated with a AmBe neutron source. On the x-axis the energy is plotted in keV (0 to 3000keV) and on the y-axis the ratio of the events in the short and long integration gates is plotted in arbitrary units. The event-density differences between the plots are due to different statistics of the measurements. The overlap at high energies is due to saturation effects of the PMT for scintillators with a high light output. More details are given in the text.

scintillator is required. This would generally be possible by calculating the ratio of the pulse heights of an event measured by both PMTs. In addition, since for the scattering experiment only the neutron/gamma-discrimination capability is important (see section

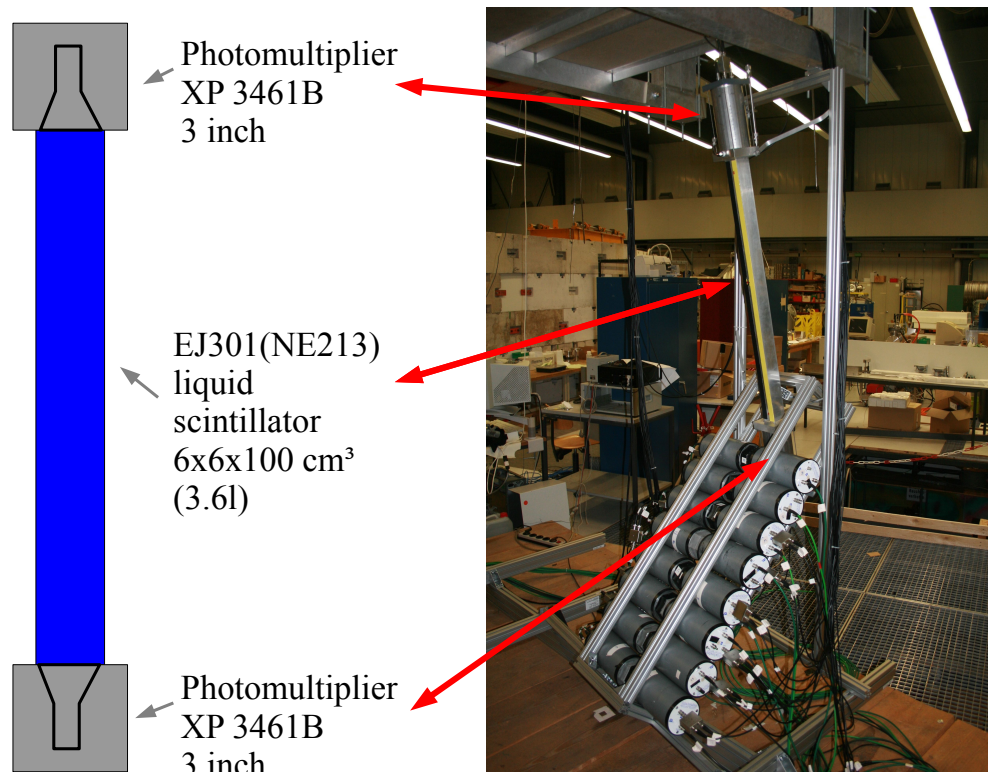


Figure 7.23: Left: Schematic view of the large-area neutron detector ("Grossmaul" detector). Right: Picture of the prototype of the large-area neutron detector. It is mounted above the side neutron-detector array, that is equipped with 16 PMT (grey tubes).

8), no energy calibration is necessary. However, a calibration is helpful to characterize the detector and determine its separation threshold (see section 7.3.5).

7.4.2 First Measurements

The first measurement was performed with an AmBe neutron-source [15] irradiating the large-area detector from a distance of $\sim 170\text{cm}$, which is the typical distance between crypdetector and neutron detector during a beamtime (see chapter 7). In order to test the neutron/gamma discrimination an additional measurement has been performed with a ^{22}Na -gamma source. The data is acquired with the same system used for the measurements described in section 7.3.6. Figure 7.24 shows a discrimination plot of one PMT of the detector, where the ratio of the results of the short and long intergration gates is plotted versus the pulse height. Events from the AmBe neutron source and the ^{22}Na gamma source, are plotted by black and grey dots, respectively. This measurement confirms the good neutron/gamma capability of the scintillator EJ301 (NE213) even for a large scintillator volume (3.6l).

Unfortunately, no energy calibration is possible since the events take place everywhere in

the tube and thus arrive at the PMTs with different pulse heights. Hence no Compton edges are visible and no value for the discrimination threshold can be stated. However, it can be seen, that the proton recoil band is broader (less discrimination capability) compared to that obtained in a measurement with a small scintillator cell of 0.3l (see figure 7.22). The discrimination threshold can be estimated using the energy, where the PMT starts to saturate (see figure 7.22 for EJ301), as a rough energy calibration. The threshold is estimated to be $\sim 350\text{keV}$ and thus a factor ~ 3 higher than the threshold obtained for the small scintillator volume. However, the detector covers a ~ 5 times larger area per channel compared to the ordinary neutron detector.

These first results look promising and for the beamtime in December 2009 the prototype of the "Grossmaul" detector was operated.

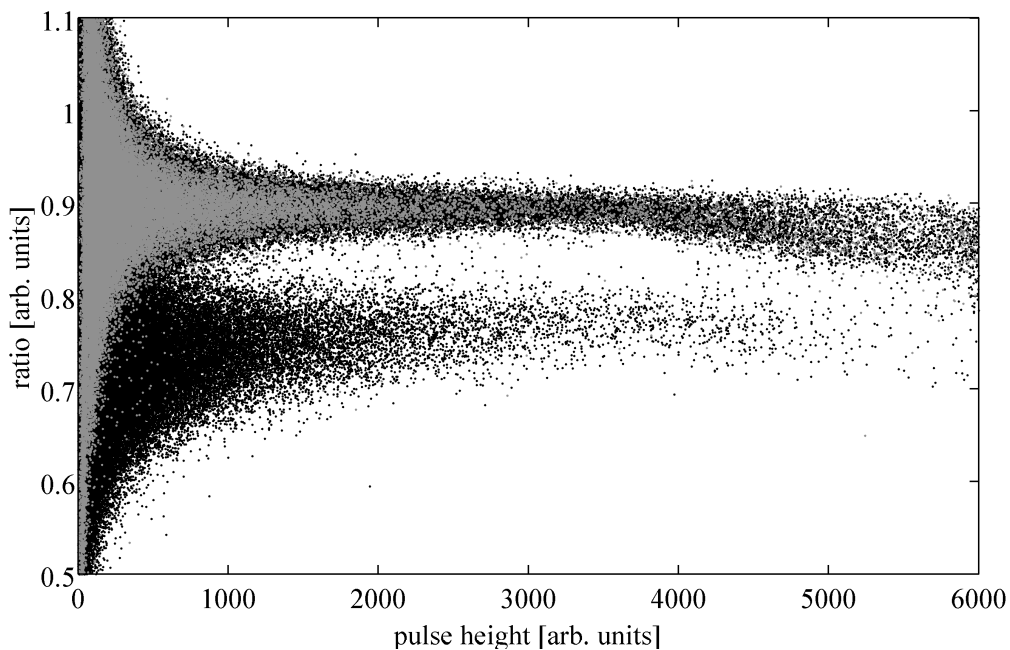


Figure 7.24: Scatter plot of one PMT of the large-area detector, irradiated by an AmBe-neutron source (black) and a ^{22}Na -gamma source (grey). The ratio of the results of the short and the long integration gates is plotted versus the pulse height in arbitrary units. The upper band corresponds to gamma-induced electron recoil events and the lower band to neutron-induced proton recoils.

7.4.3 Future Improvement

For a further improvement of the large-area detector, the reflectivity of the inner walls of the Al tube has to be increased in order to guide more light to the PMT cathodes. A comparison between figure 7.24 and figure 7.22 shows, that the mean pulse height of proton recoils is lower for the larger detector. This can easily be explained, since the light intensity decreases by $\sim 10\%$ at every reflection, hence the larger the distance between the PMT and the position of the event in the scintillator, the smaller the detected light signal. If the reflectivity is increased, the position-dependent difference in the pulse heights should become smaller and thus an energy calibration could be possible. In

addition, the difference of the pulse shapes between electron and proton-recoils should be more significant, if the light intensity is increased.

A reflectivity of $\sim 99.9\%$ can be achieved with a highly reflective foil (VM2000A) as used for example in the CRESST experiment. However, it is quite challenging to cover the Al tube with the foil, as the scintillator dissolves the glue on the back-side of the foil. The glue has to be removed or sealed by a scintillator-resistant glue.

Another approach to improve the current setup is to analyse the data with respect to the position of the event in the scintillator volume, which can be reconstructed by determining the ratio of the pulse heights measured with both PMTs. Thus the pulse-height spectrum would be less smeared out and a position dependent energy calibration and discrimination between neutrons and gammas would be possible.

7.5 Data Acquisition

7.5.1 VME Modules

The scattering experiment (described in chapter 6) requires an advanced and fast electronic data-acquisition system. Since the time-constants of cryodetector ($\sim 2\text{ms}$) and PMTs ($\sim 10\text{ns}$) differ by several orders of magnitude, a hardware coincidence-search is not possible. Hence all events in all detectors during the measurement campaigns are recorded and the analysis is performed offline. The huge amount of data (several terrabytes of data per week) requires a fast bus system. For this reason, a VME-based system was chosen and developed in [36].

The following VME-based modules are used:

- **Time to Digital Converter** (CAEN v1190, 64 channels): The event times of all detectors (PMTs, cryodetectors) and the logical signal from the buncher of the accelerator are recorded. The TDC is working in a continuous recording mode.
- **Analog to Digital Converter** (Struck Sis3302, 8 channels): The cryo-pulses from the phonon and the light detectors are recorded with a maximum sample rate of 100MHz and a resolution of 16bit. The pulse can be averaged onboard in order to reduce the amount of data and to filter noise.
- **Analog to Digital Converter** (Struck Sis3320, 8 channel): Five of these flash-ADC modules are operated to allow data-taking of up to 40 PMTs. The main feature of these modules is, not to record the full pulses, but to apply integration gates to the pulses in order to achieve a pulse-shape discrimination (see section 7.3.1). Only the results of these gates are stored, which reduces the amount of data significantly (several orders of magnitude).
- **Constant Fraction Discriminator** (CEAN v812, 16 channels): CFDs do not trigger on a certain threshold but on a fraction of the pulse height, which makes the trigger time independent of the pulse height. All detectors are connected to one of the three CFD modules and the output is directly fed into the TDC.
- **VME controller** (CAEN v2718): The VME controller connects the VME bus to a standard PC by an optical-fiber cable.

A more detailed explanation of the electronic system will be given in [36]. The data-readout of the modules is described in section 8.1. In figure 7.25 the connection scheme of the electronic devices and the detectors is shown.

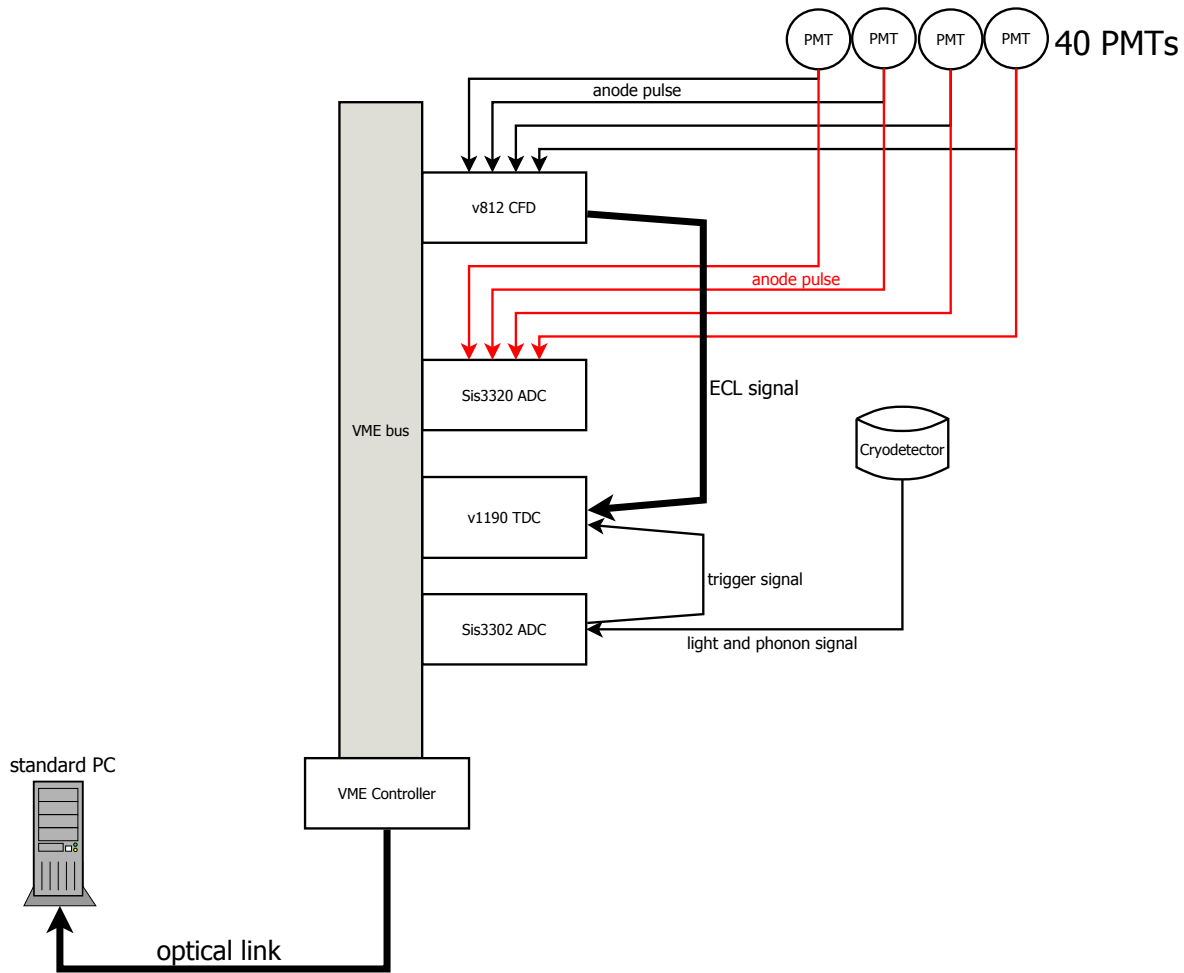


Figure 7.25: Wiring scheme of the VME-based modules and the detectors of the neutron scattering experiment. PMT signals are converted to logical signals (ECL standard) by the CFDs and forwarded to the TDC module [36].

7.5.2 Acquisition Software

For control and readout of the VME-based electronic system, a dedicated software was developed in [36]. In the following the most important features are pointed out.

The software was written in C++ and has a graphical interface to display pulses of all detectors even during the measurement. These live-plots are an important tool to check the functionality of the setup at all times. Besides the pulses from the cryodetectors, PMT pulses can be displayed and the integration gates for the pulse-shape discrimination (see section 7.3.1) can be applied. The length of these gates can be optimized, while the neutron/gamma discrimination capability is checked in a live-discrimination plot (e.g. see figure 7.13). In addition, the software is able to display live-coincidence plots

(like figure 9.1) between two channels. This is especially useful for the adjustment of the beam-pulsing (see section 7.1.2), where a live-coincidence measurement between accelerator bunch and a PMT positioned at a scattering angle of 0° is performed. All parameters of each VME module can be modified at any time (such as trigger settings, thresholds, sampling rates, etc.).

Finally, the data from the VME modules is saved on the hard discs of a PC and is then backed up on the server of the MLL-laboratory in Garching.

Chapter 8

Data Analysis

The software for the data analysis of the neutron-scattering experiment has been written in the numerical computing environment MATLAB and is described in more detail in [36]. High importance was given to the automatization of the individual steps of the analysis, since the enormous amount of data (~ 3 Terrabyte per week of beamtime) makes a manual operation impossible. Nevertheless, every step of the analysis has to be properly monitored and results of the individual steps have to be interpreted before proceeding. Since MATLAB is able to quickly display intermediate data and easily allows changes to the program code, it was favoured over programming languages like C++ which would allow faster computing.

This chapter gives a brief overview of the steps of data analysis used in this work.

8.1 Data Readout

The data of the measurements acquired by the VME-electronics modules (section 7.5.1) are loaded into the MATLAB environment. All modules of the readout electronics are explained in section 7.5.1. In the following the data output of all types of modules are described.

ADC (Sis3302) for the Cryodetector

For both, phonon and light detector, the pulses are recorded with the following properties:

- General pulse parameters: trigger, addresses concerning measurement and pulse numbers
- Full sampling of all pulses (typical sampling length: 30.000 data points, sampling rate: max. 100MHz)
- Timing information derived from the trigger of each ADC (so-called time stamps)

ADCs (Sis3320) for the neutron detectors

Events recorded by the 40 ADC channels (actually 34 neutron detectors have been operated) are saved with the following information:

- General pulse parameters: trigger, addresses concerning measurement and pulse numbers, ...)
- Results of up to eight integration gates, which sum different parts of the pulses (see section 7.3.1)
- Timing information derived from the trigger in the ADC (time stamps)
- Additional pulse information (pulse height, channel number of detector which triggered)

The on-board application of the integration gates, instead of recording the whole pulse, saves memory. This is important, since we have to cope with high rates in the PMTs ($\sim 100\text{Hz}$)

TDC module

The signals of the neutron detectors, the cryodetector and the logical pulse from the buncher of the accelerator (see section 7.1.2) are recorded with a 64-channel TDC module. The following information is recorded

- channel number
- timing information (time stamps)

A measurement campaign (beamtime of ~ 1 week) is typically split into periods ranging from a few hours to a maximum of one day, because maintenance at the experimental setup and monitoring of the pulse conditions of the accelerator make it necessary to interrupt data-taking. The data is saved in different folders and has to be treated as individual measurements, since maintenance can change the setup (for example: working point of the cryodetector). These folders are combined at the end of the data analysis, when comparability is checked.

8.2 Analysis of the Cryodetector Pulses

The Analysis of the pulses of the cryodetector, which is described in section 7.2.2, is an ambitious undertaking. In figure 8.1 typical pulses from the light detector (grey) and the phonon detector (black) are shown. They are measured simultaneously.

8.2.1 Creating a Standard Event

Figure 8.2 shows the transition curve of the phonon detector used in this setup. The temperature of the TES (Transition Edge Sensor) is stabilized in its transition from the normal-conducting to the superconducting state, preferably in the region where the transition is fairly linear. Thus the pulse height is supposed to be proportional to the total energy deposited in the absorber. Nevertheless, if the energy is high enough to reach the non-linear part of the transition or even as high that it warms up the detector to the normal conducting state, the pulses saturate and the detected pulse height is no longer a good measure for the deposited energy. In the normal-conducting state the resistance does not significantly change anymore with temperature and thus the pulse

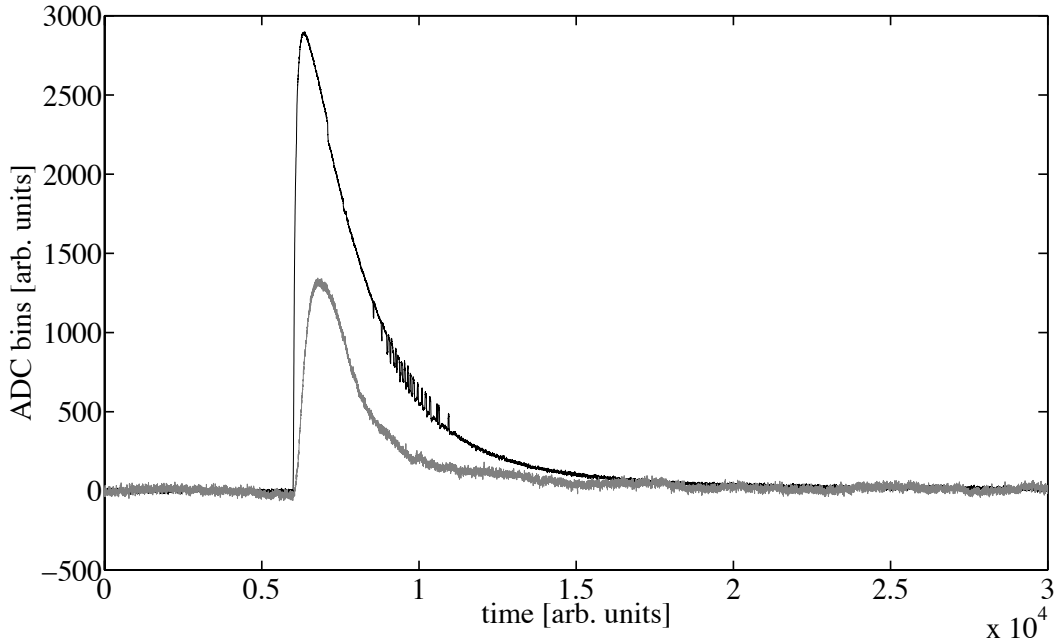


Figure 8.1: Typical pulses from an electron recoil in the CaWO_4 crystal: phonon detector (large, black line) and the light detector (small, grey line). Raw samples of the ADC are plotted in arbitrary units. Typical decay-time constants for this detector are $\sim 2\text{ms}$ (see section 7.2.2).

is flattened at the top (see figure 8.5 in section 8.2.2).

Also noise (which is difficult to avoid in our very sensitive setup) makes an energy determination, where simply the maximal pulse height is measured, impossible, because the deposited energy would be overestimated.

In order to determine the amplitude of the pulses, a dedicated fitting method (the so-called standard-event fit) is used. This method is widely spread for the data analysis of cryogenic experiments (e.g. CRESST) [51]. For this reason a toolbox to establish the standard event fit was integrated in our MATLAB environment [36].

Realisation of the Standard-Event Fit

In figure 8.3 the unfitted amplitude of the light channel is plotted versus the amplitude of the phonon channel. Clearly two bands arising from electron and nuclear recoils appear. The bending of the bands at higher pulse heights arises from the saturation effect originating from non-linearities of the TES transition. A coarse energy calibration is achieved by localising the peaks of the calibration source (here ^{133}Ba), which was always present during the measurement campaigns. The most prominent gamma-line of ^{133}Ba at 356 keV is most visible (see figure 8.3). Additionally, muon-induced electron-recoil events appear significantly in the energy range from 0-500keV.

The phonon detector is fairly linear up to a recoil energy of $\sim 100\text{keV}$. This was determined from the analysis described in this work and in [35] [28]. Thus, pulses from the energy region $\pm 20\text{keV}$ around $\sim 100\text{keV}$ (typically from the electron-recoil band) are chosen to build a standard event. This can be achieved by summing the selected

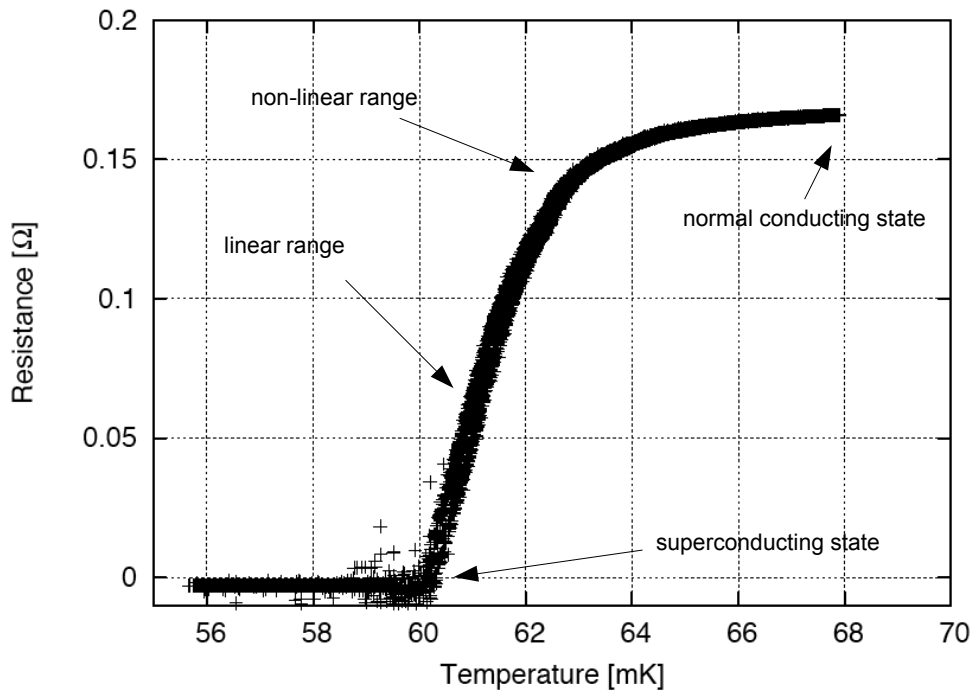


Figure 8.2: The resistance of the Transition-Edge Sensor (TES) of the phonon detector used in this work is plotted versus the temperature. The transition curve between superconducting and normal-conducting state has linear and non linear regions. The curve was recorded in [35].

pulses and by normalizing the amplitude of the resulting pulse to one. The resulting standard event has a smooth shape, because the procedure works as a filter for the noise, which occurs statistically. In figure 8.4 typical standard events for the phonon and for the light channel are shown.

If the deposited energy in the absorber is high enough to saturate the detector, the pulses are flattened at the top and the pulse shape above this energy cannot be used to reconstruct the real pulse height. Hence, only the information from the pulse shape up to this energy (so-called cut-off energy) is used for the fitting procedure. This method is called the **truncated standard event fit**.

The truncated standard events are fitted to every pulse of the phonon and light detector. The free parameter of the fit is the onset of the cryo-pulse. For each onset, the pulse height giving the minimum RMS (root mean square) value, is calculated. The cut-off energy is fixed and equal for all pulses. In figure 8.5, the working principle of this fitting method is demonstrated. The black (solid) line indicates the standard event for the pulse, which is plotted in grey. Only the pulse shape below the dashed line is fitted. Above this energy the pulse shape deviates significantly from the real shape because of saturation effects. As a consequence, one would underestimate the energy of the events by only looking at the pulse height.

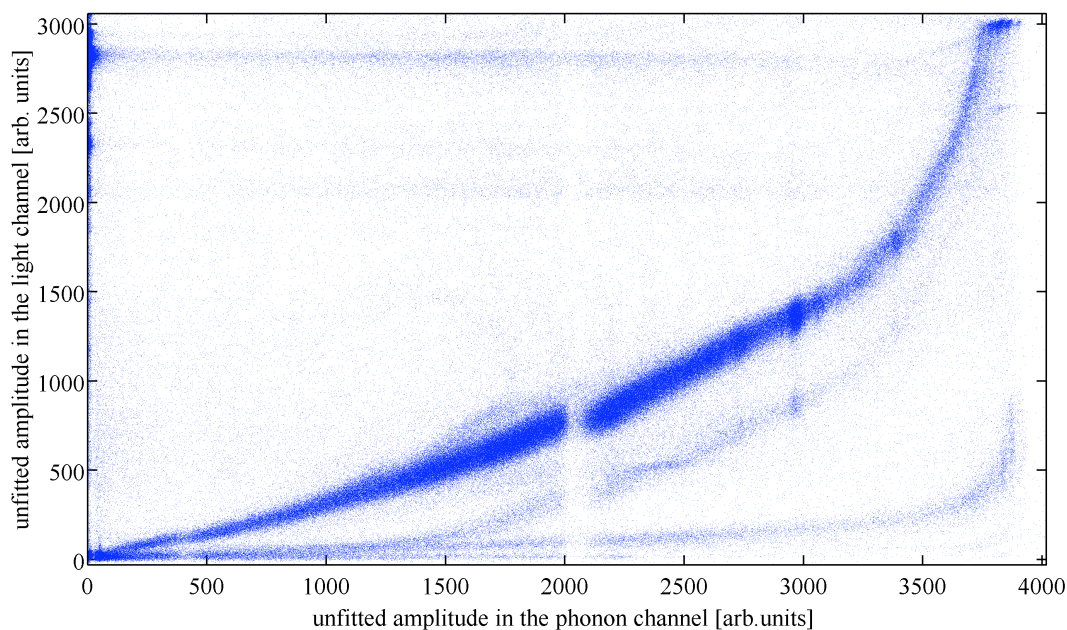


Figure 8.3: A typical scatter-plot, where the unfitted pulse height in the light channel is plotted versus the pulse height in the phonon channel, is shown from a measurement in presence of the neutron beam and an additional ^{133}Ba calibration source. Several populations of events are visible, the most prominent band is referred to as the electron recoil band, in which also the γ -lines of ^{133}Ba are visible. The bands of events at lower light energies are neutron-induced nuclear recoils. The bending of the bands at higher energies originates from saturation effects, of both the phonon and the light detector. The gap at about 2000 on the x-axis is an artefact of the transition curve of the phonon detector [36].

In figure 8.6, the fitted amplitudes of the light channel is plotted versus the fitted amplitude of the phonon channel. After the truncated standard event fit was applied to all pulses of a measurement campaign, the two bands corresponding to electron and nuclear recoils show a linear behaviour up to the MeV phonon-energy range. An additional population originates from X-ray events from the ^{55}Fe source placed below the light detector. This events are light-only events, since X-rays are absorbed directly by the Si substrate of the light detector and thus no phonon signal in the CaWO_4 crystal is expected. This kind of events can be seen in figure 8.3 along the y-axis with a vanishing energy in the phonon channel.

8.2.2 Quality Control of the Events

In this section various populations of events, which cannot be fitted by the standard-event method, are described and solutions to identify them are presented. Events are either modified in order to be fitted correctly or discarded, in order not to falsify the results. An important tool to identify events is the RMS plot, where the root-mean-square value (RMS) of the standard event fit is plotted versus the fitted amplitude in the phonon channel (figure 8.7) and the light channel, respectively.

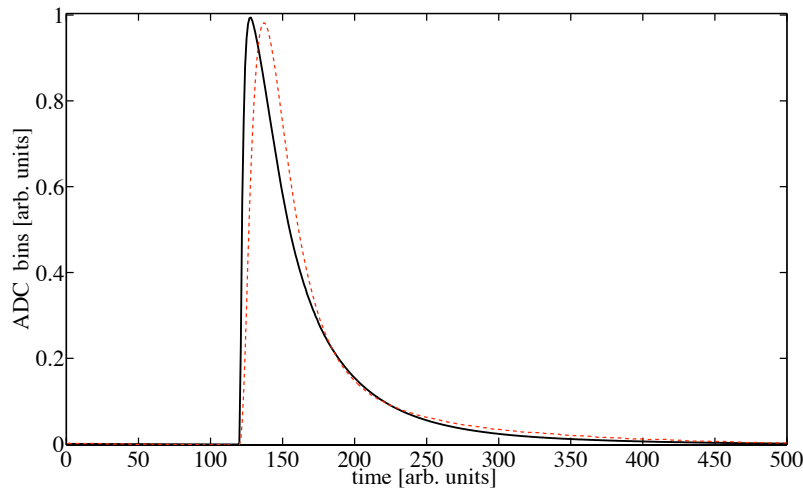


Figure 8.4: Standard events for the phonon (solid black line) and the light detector (dashed red line), constructed by summing electron recoil pulses from the energy region $\pm 20\text{keV}$ around 100keV .

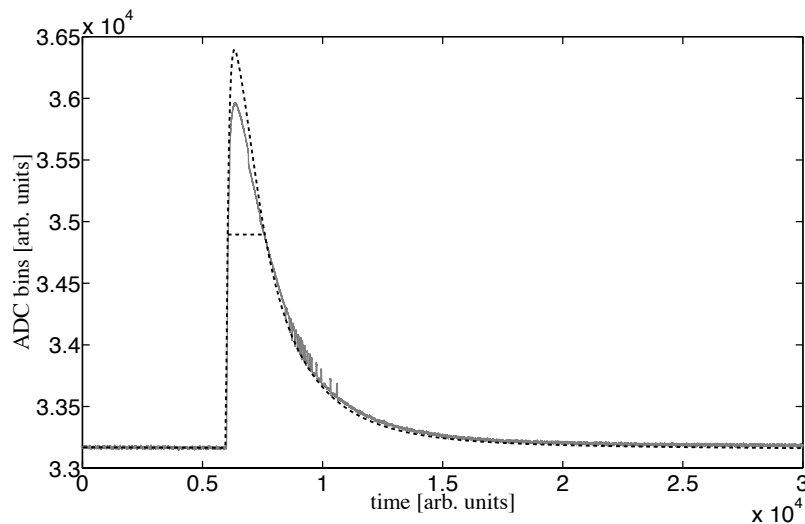


Figure 8.5: A pulse (grey line) with an energy higher than the cut-off energy (dashed black line). The dashed curve indicates the respective standard event. Further explanations are given in the text.

The following populations of events have been identified and methods to treat them are described:

- Events caused by **missing ADC data** (see [36]) as shown in figure 8.8(a), where the first samples were not recorded and show random data. This strongly affects the fitting procedure, the free parameters of the fit are mismatched. The software determines those events and discards them.
- **Pile-up events**, as shown in figure 8.8(b), that are caused by too high event rates, can easily be identified by checking the monotonicity of the pulse decay. If a new

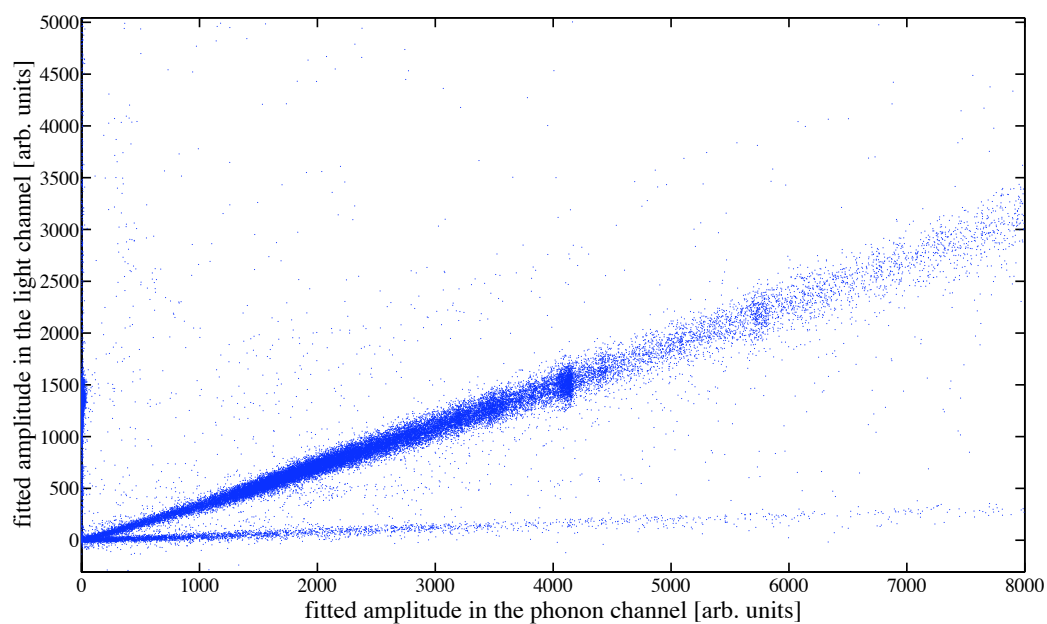


Figure 8.6: Events fitted by the truncated standard-event method are shown in a scatter-plot, where the fitted amplitude in the light channel is plotted versus the fitted amplitude in the phonon channel. The linear detector response up to large pulse heights is clearly demonstrated. The upper band corresponds to electron-recoil events induced by ^{133}Ba -gammas or muons, whereas the events in the lower band are due to nuclear recoils from the neutrons of the accelerator beam, which was always present during this ~ 1 day measurement. The kink in the electron recoil band at pulse height ~ 1500 is due to energy dependent quenching at lower energies (see section 5.2).

pulse appears before the previous pulse has fallen to the baseline level, both events are discarded. For the future, a data analysis software will be built to reconstruct, at least a fraction of pile-up pulses.

- Events with an **unstable baseline** (figure 8.8c,d) can be caused by many reasons: If a previous pulse has not fallen completely to the baseline level before a new pulse rises, its amplitude will be determined in a wrong way. Second, the baseline can be unstable due to electronic noise or mechanical vibrations (microphonics). Third, in several beamtimes strange undershoots appear in the pulses, which are not completely understood. Fortunately, these events can be discarded from the data analysis by cutting away pulses with a large standard deviation of the baseline .
- At higher energies **flux-quantum losses** in the SQUIDs arise often (for explanation see [28]) and thus the baseline is lowered by a multiple of the flux quantum. In figure 8.8(e) a typical pulse of this kind is plotted. In the fitting process flux-quantum losses are compensated. Thus these pulses can be treated as normal events.
- **X-ray pulses** from the ^{55}Fe source (see figure 8.8(f)) have a different pulse shape and are thus not well-fitted by the standard event for light pulses originating from

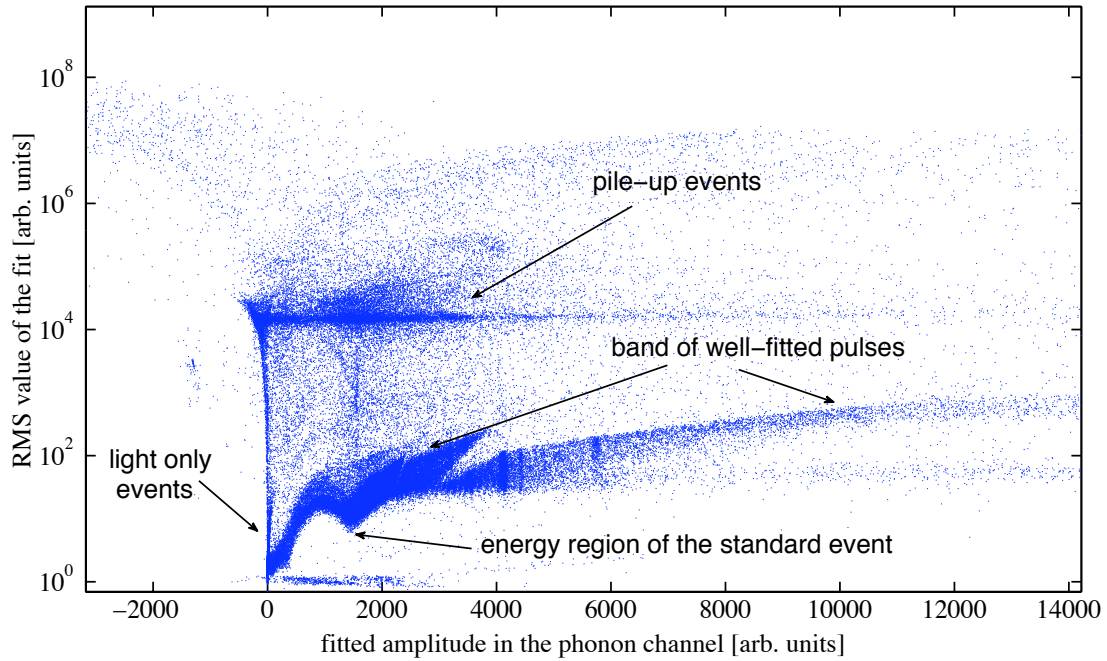


Figure 8.7: The RMS value of the fit is plotted versus the fitted amplitude in the phonon channel. The RMS value provides a measure of the quality of the fit. The lower dominant band contains well-fitted pulses. The local minimum at an amplitude of ~ 1500 is the region, where the standard event was taken from. The splitting of the band at higher energies is due to different numbers of flux-quantum losses of the SQUID. Pile-up and other events, that are fitted incorrectly (see text), are located at higher RMS values.

the CaWO_4 crystal. X-ray pulses can easily be identified, since they do not affect the phonon channel (light-only events).

- During long-time measurements (~ 1 week), the **working point** of the detectors can change for several reasons (e.g. warming up of the detector due to mechanical vibrations). This in turn changes the detector response. Since a change in the working point has an impact on the mean standard deviation of the baseline, a sudden change can be identified by controlling this value (see figure 8.9). It has to be checked properly, if these changes affect the resolution of the detector significantly. If necessary, these regions can be cut away (usually called stability cut).

After the cuts described above have been performed, remaining events with RMS-values in one of the detectors - much higher than the average for a certain amplitude - are cut away graphically in the RMS-plot (see figure 8.7).

The methods described in this section secure a high quality of the fitted pulses. However, the price one has to pay is, that $\sim 60\%$ of all pulses are excluded from the data analysis.

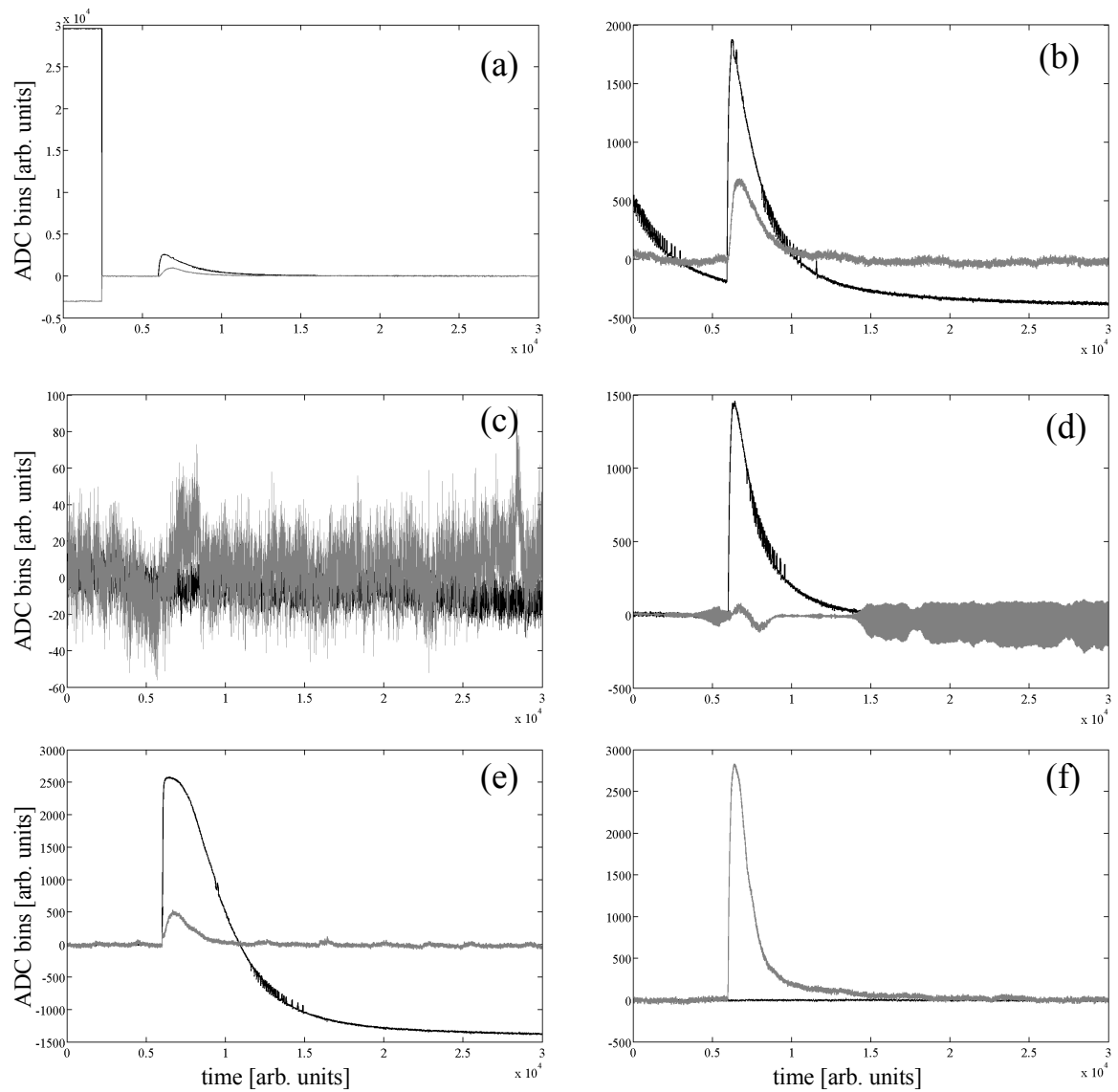


Figure 8.8: Black lines indicate the phonon channel and grey lines describe the light channel. Six examples of pulses, to which special attention has to be paid. (a) Pulse pattern originating from missing ADC data (b) Unstable baseline due to pile-up: the previous pulse has not yet completely fallen back to baseline level. (c) Noise trigger. (d) Undershoot after a pulse in the light channel (not completely understood) and oscillations. (e) Shift of the baseline originating from flux quantum losses in the SQUID. (f) Direct absorption of an X-ray from the ^{55}Fe source in the light detector. Further explanations in the text.

8.2.3 Calibration of the Cryodetector

Calibration of the Phonon Detector

During the beamtimes a ^{133}Ba source is always present in order to calibrate the phonon detector. The source is placed at a distance of $\sim 1\text{m}$ from the cryodetector to avoid too high counts rates.

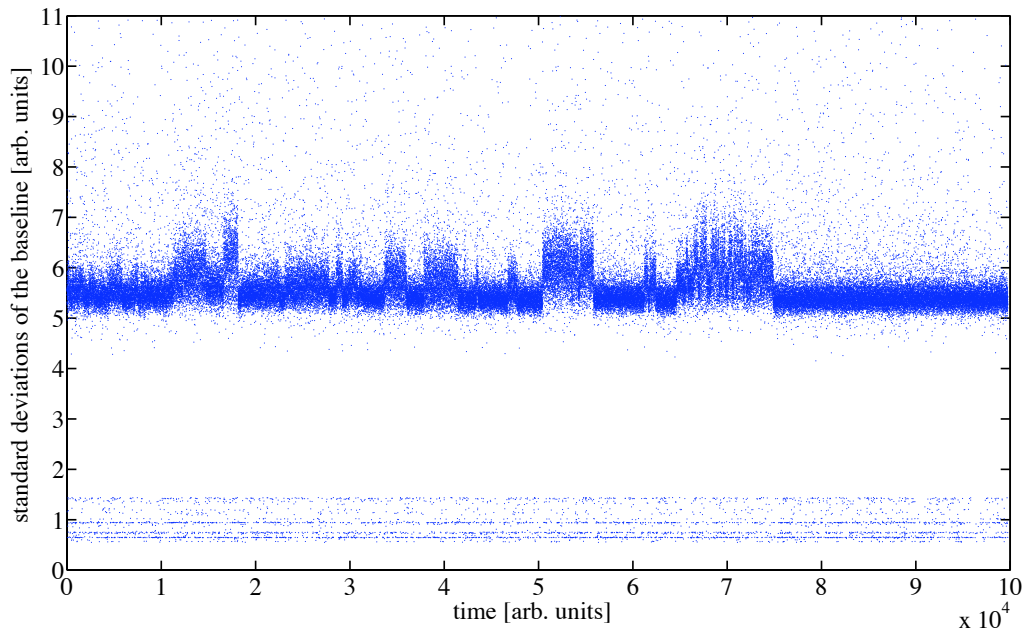


Figure 8.9: The standard deviation of the baseline of pulses in the phonon channel is plotted versus time. The sudden change of the mean value of the prominent band indicates a change in the working point of the detector.

In figure 8.10, a typical energy spectrum of the CaWO_4 phonon detector from a measurement of ~ 5 days is plotted. The four γ -lines from ^{133}Ba (276.4keV, 302.9keV, 356.0keV and 383.8keV) and the $e^+ - e^-$ annihilation line at 511keV are clearly visible. The muon-induced background up to ~ 400 keV is the dominant background source. The γ -lines have been fitted by Gaussians, for the dominant ^{133}Ba -line at 356.0keV the FWHM is about 8.3keV. Because this value is obtained by fitting the peak with the largest statistics, it is a good indicator for the energy resolution of the detector. Also it is a proof for the stability of the detector, as the spectrum is recorded over a period of ~ 3 days.

The curve that fits the calibration points in a reasonable way is a power law of the form

$$E = a \cdot x^b \quad (8.1)$$

where x is the fitted amplitude in the phonon detector, E is the deposited energy, a and b are the fit parameters. In figure 8.11 the calibration curve is plotted together with the calibration points. The result for the fit parameter b is - depending on the working point of the detector - in the order of 1.05 ± 0.05 and thus the detector response is fairly linear.

Calibration of the Light Detector

The silicon substrate that is used as the light detector can, in principle, be calibrated by γ -sources as well. However, on the one hand, the resolution of the light detector is not as good as the phonon channel and thus closeby lines cannot be separated. Furthermore,

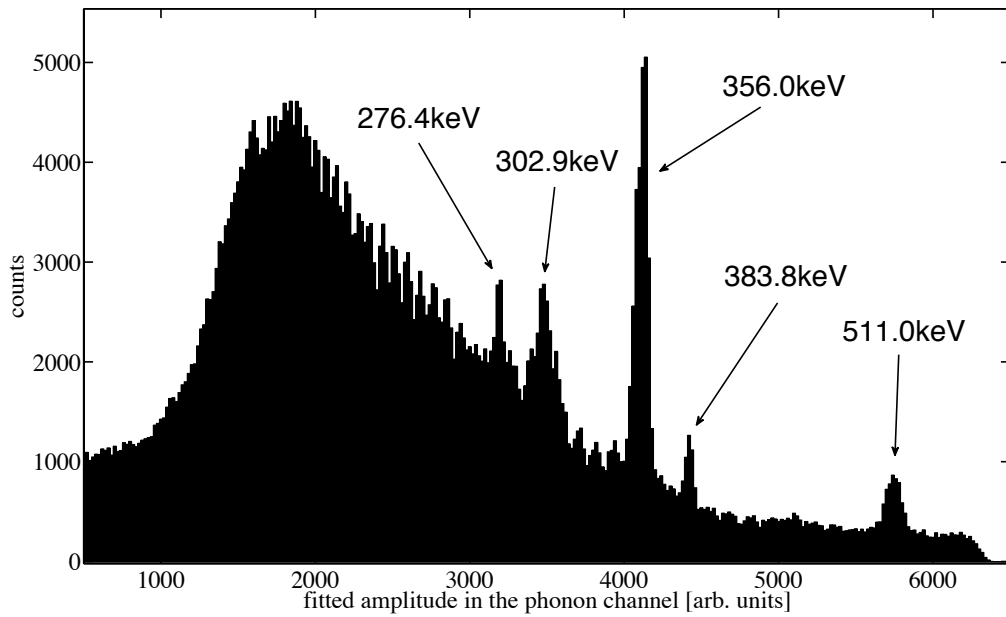


Figure 8.10: Calibration spectrum of the phonon detector irradiated by a ^{133}Ba -source (276.4keV, 302.9keV, 356.0keV and 383.8keV). The peak at 511.0 keV is due to $e^+ - e^-$ annihilation.

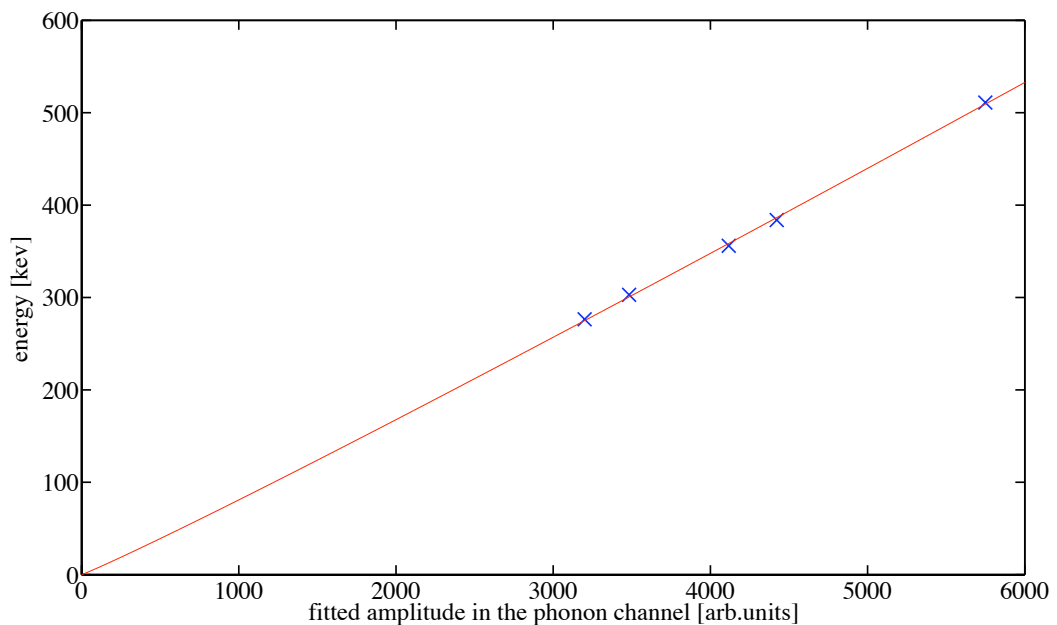


Figure 8.11: The calibration points for the phonon detector from a ^{133}Ba -source (276.4keV, 302.9keV, 356.0keV and 383.8keV) and the $e^+ - e^-$ annihilation (511.0keV) are fitted with a power law function $E = a \cdot x^b$.

it cannot be excluded that the CaWO_4 crystal shows non-linearities (depending on the excitation energy) in its emission spectrum. Thus, this method is not sufficient to prove

the linearity of the light detector.

However, a calibration can be achieved by using the X-ray pulses from a ^{55}Fe source, mounted below the light detector. ^{55}Fe decays to ^{55}Mn by electron capture and the excited ^{55}Mn atoms further deexcite to the ground state by X-ray emission. Hence the K_α (5.899keV) and K_β (6.490keV) lines can be detected in the silicon substrate. In addition an Al foil is installed between the ^{55}Fe source and the light detector. Most of the X-rays pass the foil without interaction, but the interacting ones excite Al atoms. The deexcitation process produces X-rays of 1.49keV, commonly referred to as Al-fluorescence (emission). The X-rays are fully absorbed by the silicon substrate and the produced phonons are measured with a TES (see section 7.2.2). When the X-ray photons interact in the Si substrate, Si atoms are excited, which deexcite by X-ray emission of 1.74keV (Si-fluorescence). If these photons escape the substrate (events near the surface), the detected energy is the difference between the energy of the incoming X-ray photon and the Si-fluorescence photon of 1.74keV. Hence two, so-called Si-escape peaks (4.16keV and 4.75keV), corresponding to the K_α and the K_β line of ^{55}Mn arise.

For the calibration with X-rays a separate standard event fit is applied, where the standard event is constructed by X-ray pulses. This is necessary because the pulse shapes due to X-rays that are absorbed directly by the light detector and due to the scintillation light originating from the CaWO_4 crystal, differ.

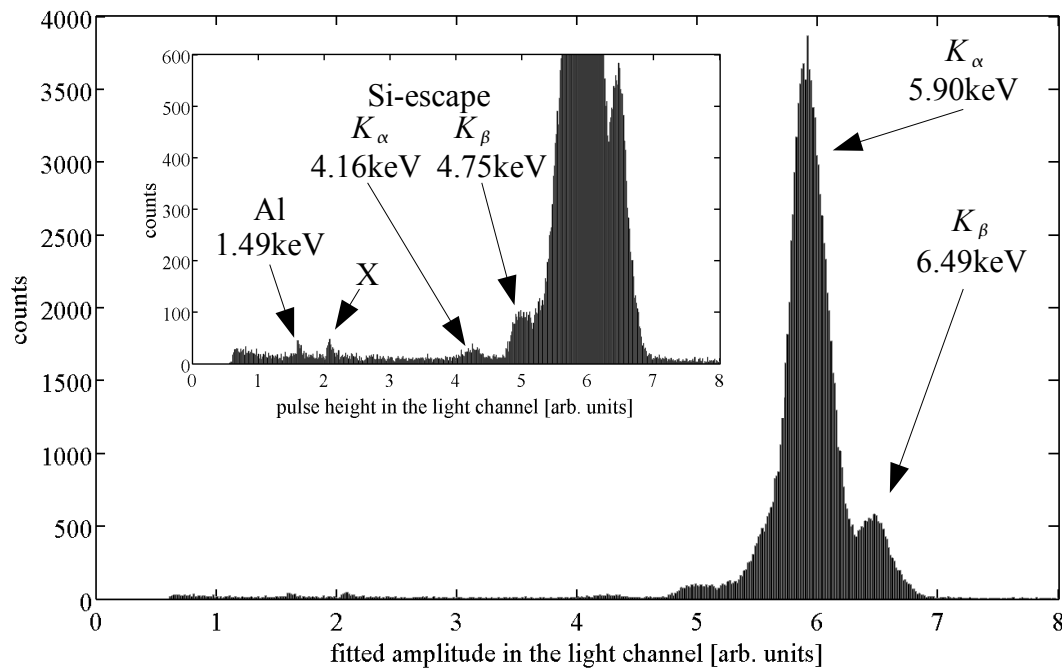


Figure 8.12: Calibration spectrum of the light detector irradiated by a ^{55}Fe source. The K_α and K_β , the respective Si-escape peaks and the Al-fluorescence originating from the Al-foil on top of the source are used for calibration of the light detector (see text). The origin of an additional peak appearing at $\sim 2.1\text{keV}$ is not yet understood. This has to be investigated in future experiments.

In figure 8.12 a typical X-ray calibration spectrum irradiated ~ 3 days by a ^{55}Fe source is plotted. The calibration points can be fitted with a linear fit (see figure 8.13)

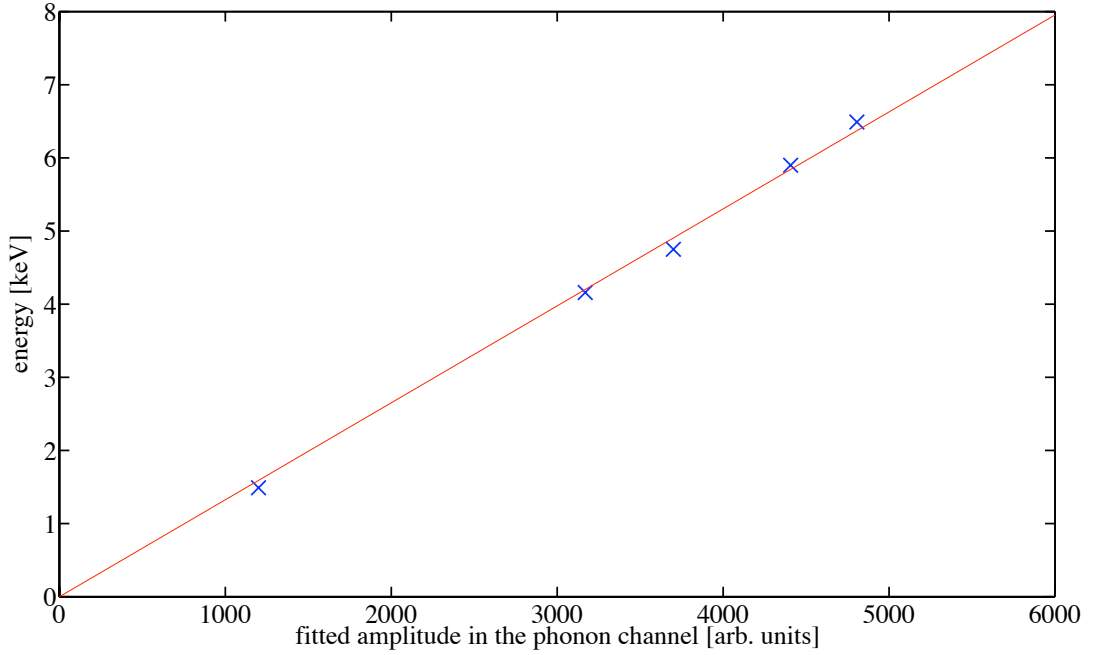


Figure 8.13: The calibration points for the light detector from a ^{55}Fe -source ($E_{K_\alpha} = 5.90\text{keV}$, $E_{K_\beta} = 6.49\text{keV}$), the Si-escape peaks ($E_{\text{Si}-K_\alpha} = 4.16\text{keV}$, $E_{\text{Si}-K_\beta} = 4.75\text{keV}$) and the Al-fluorescence line at 1.49keV are fitted with a linear function.

$$E = a \cdot x \quad (8.2)$$

where x is the fitted amplitude, E the energy deposited in the absorber and a the fit parameter. The FWHM of 390eV and thus the energy uncertainty of the most prominent peak (K_α) is regarded as the energy resolution of the light detector. This is in good agreement with the value obtained in [35].

Now, that the linearity of the light channel is proven, the **absolute energy calibration** of the light detector can be achieved.

The prominent ^{133}Ba -line at 356.0keV can be cut out graphically of a scatter plot as the one shown in figure 8.6. Hence the position of this line in the light channel can be determined with high precision by a Gaussian fit. This point can be used to scale the light channel in terms of an electron-equivalent energy (see section 5). Assuming that the energy dependence of the QF is negligible in the energy range from 100 to 400keV (see section 5.2), the light yield can be normalized to 1 for electron recoils of 356keV . The linearity is further checked by analyzing the calibration data, where other γ sources were present (^{22}Na , ^{137}Cs and ^{57}Co). Unfortunately, our ^{57}Co source placed outside the cryostat was too weak to obtain a sufficient rate to use it for a continuous calibration during the beamtimes. For future experiments a new ^{57}Co source will be available. This is important to reach consistency with the calibration method used in CRESST (see section 5).

Figure 8.14 shows a yield plot of a fully calibrated data set of $\sim 3\text{days}$ in the phonon energy region from 0 to 1.1MeV .

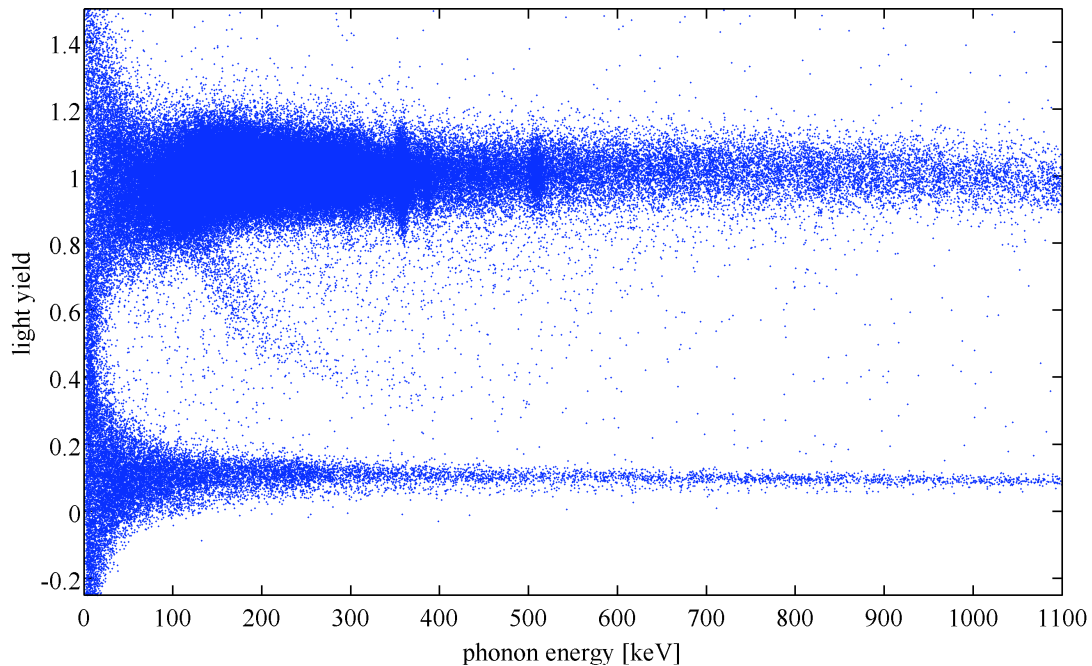


Figure 8.14: The light yield is plotted versus the phonon energy for a ~ 3 day measurement, where the neutron beam and the ^{133}Ba source were present. The upper band originates from gamma-induced electron recoils, the lower band from neutron-induced nuclear recoils. The light yield was normalized to one for electron recoils at an energy of 356.0keV (γ -line of ^{133}Ba). Events between the bands are due to inelastic scattering off tungsten (see chapter 9).

8.3 Search for Coincident Events

8.3.1 Time Stamp Mapping

Since the different VME-modules have different clocks, the time scales disperse with time ($\mathcal{O}(\sim \text{ms/h})$) for several reasons (temperature gradients between the modules, slightly different quartz frequencies, etc.). To solve this problem, the modules can be synchronized by an external clock, which, however, leads inevitably to fixed operation frequencies for the modules. To keep maximum flexibility (different clock rates for the individual devices), another method of synchronizing the modules was chosen and developed in [36].

Since the output of the detectors are recorded in parallel by the ADCs and the TDC, the same pattern of time stamps (see section 8.1) arises in both modules, but they are scaled individually due to the different clocks. Hence the TDC time is chosen as the global time scale and the time scales of the other modules (ADCs) are rescaled ("mapping"). To achieve this, a pattern of time stamps ("finger prints" of typically ~ 100 events) in the ADC is selected. This is compared with the pattern of the TDC time stamps. When the position of smallest deviation between these two patterns is found, the position holds as a calibration point for the scales. This method of "finger print matching" is repeated every $\mathcal{O}(100\mu\text{s})$, to achieve a calibration (matching) between ADC and TDC time scales

for the whole measurement campaign. At the end of this calibration step, the global time from the TDC is assigned to every "mapped" pulse in the ADC as a new property.

8.3.2 Neutron- γ Discrimination

Due to the neutron- γ discrimination capability of the neutron detectors (see section 7.3.1), γ -events originating from the accelerator bunch and γ -background (mainly from cosmic muons) can be discarded. This is an important tool to reduce the number of accidental coincidences significantly. The discrimination cut has to be performed individually for each neutron detector, because every detector has slightly different physical properties. In figure 8.15 a scatter plot of a typical neutron detector is plotted, where the cut neutron events (red) are enclosed by full lines. The cut can be done graphically by a tool implemented in the MATLAB analysis software ("banana cut").

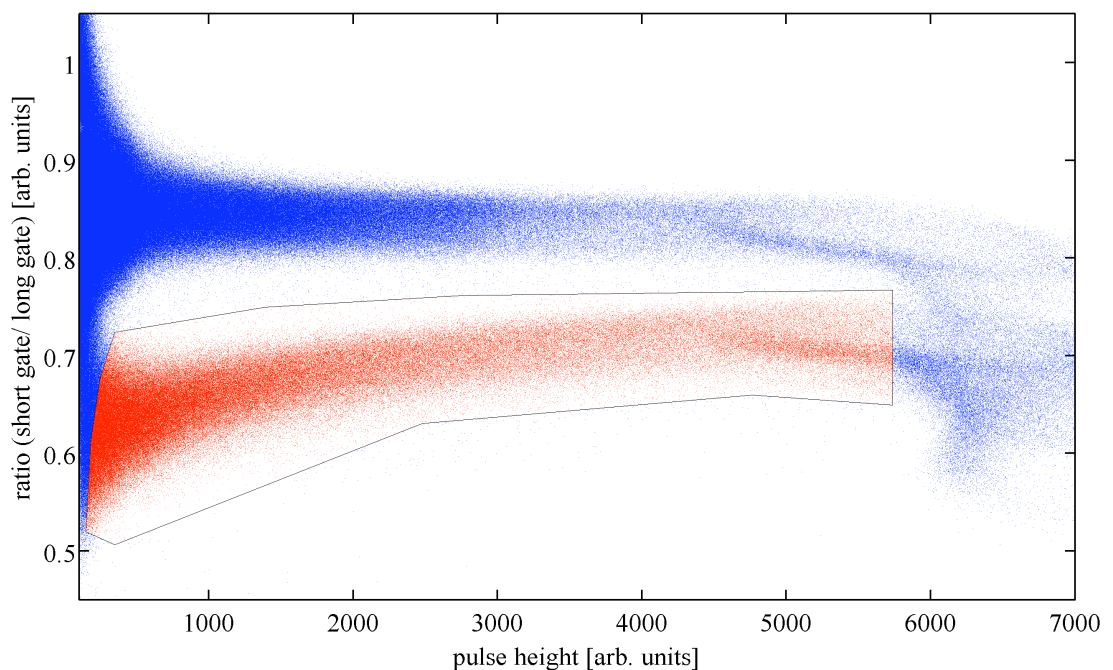


Figure 8.15: Discrimination plot of a neutron detector of the detector array (see figure 7.13). The upper band represents electron recoils induced by gammas, whereas the lower band is due to neutron-induced proton recoils in the liquid organic scintillator. The graphically performed cut on neutron events is shown as red dots enclosed by solid lines. The bands overlap above a pulse height of ~ 5500 [arb. units] due to saturation effects of the PMT. The overlap below ~ 100 [arb. units] is mainly due to electronic noise.

8.3.3 Double Coincidences

In this step of analysis, coincidences between the bunches of the accelerator and events in the neutron detectors are determined (so-called double coincidences). The bunch rate of the accelerator is $\sim 300\text{kHz}$ and the bunches have a measured bunch width of $\sim 2\text{ns}$,

which is in the order of the time jitter of the photomultiplier tubes (PMTs). Since the pulses in the neutron detectors have fast rise times ($\sim 1\text{ns}$), the trigger time of the PMT is taken as the time of the event. In a search margin of $\pm 500\text{ns}$ around every bunch of the accelerator, neutron events in the neutron detector arrays are identified.

Together with the neutrons a large number of gammas is produced in the hydrogen cell, which are detected in the neutron detector after a time $\Delta t_\gamma = \frac{\Delta s}{c}$ (after travelling a distance Δs). In figure 8.16 a typical time-of-flight (ToF) spectrum for a detector of the detector array is shown. The gamma peak at 350ns and the neutron events at about $380\text{-}550\text{ns}$ are visible. Because the absolute peak positions in ToF spectra vary from detector to detector due to different cable length and PMT properties, a time calibration is necessary for each detector.

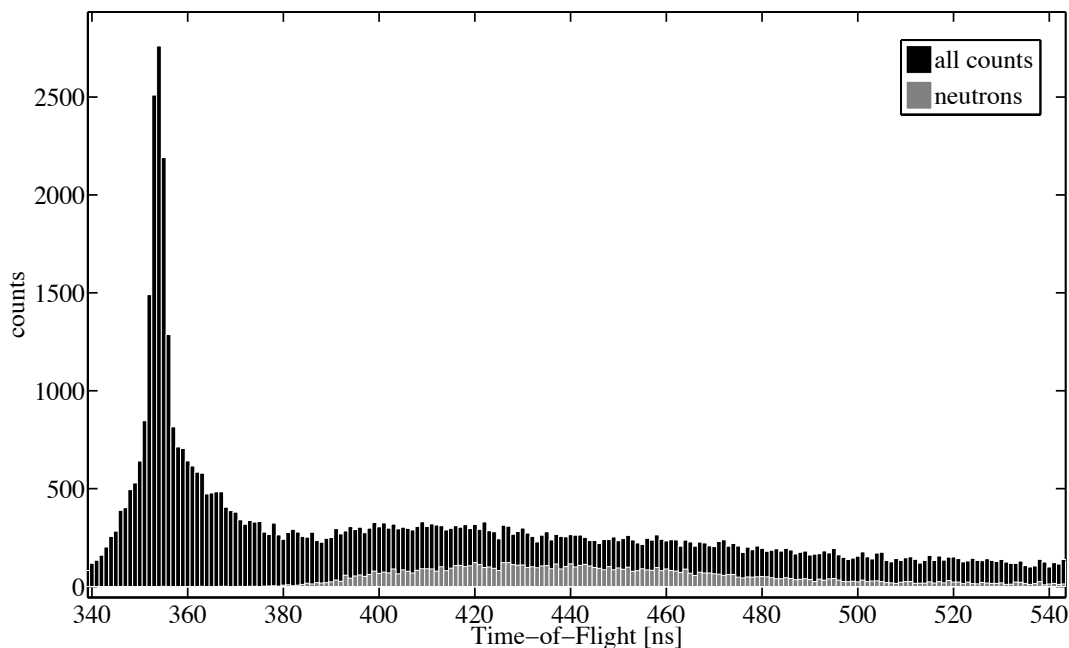


Figure 8.16: Typical ToF spectrum of a neutron detector of the detector array placed at an angle of 80° . The prominent peak at $\sim 350\text{ns}$ is due to gammas from the accelerator bunch, whereas the neutrons arrive later (from $\sim 380\text{ns}$ to $\sim 550\text{ns}$).

Since at the end one is interested in the time-of-flight of the neutrons Δt_n , the gamma peak is used to calculate the time of neutron production t_{start} in the hydrogen cell. Hence the neutron ToF can be calculated as $\Delta t_n = t_n - t_{\text{start}}$ for each detector.

8.3.4 Triple Coincidences

In order to achieve completely fixed kinematics, one has to search for coincident events from the cryodetector, the neutron detector arrays and the accelerator buncher (triple coincidences). The onset of pulses in the cryodetector can be determined with a precision of $\sim 10\mu\text{s}$, which is large compared to the timing accuracies of the neutron detectors and the signal from the accelerator bunch, both being accurate to a few nanoseconds. Pulses in the cryodetector are searched for in a time margin of $\pm 1\text{ms}$ around every

double-coincidence event. The time difference Δt_{triple} between the time of a double coincidence and the nearest cryo-pulse is calculated. Since the probability for a triple-coincidence event is very small $\mathcal{O}(0.1\frac{1}{s})$, the pulse rate of the accelerator can be of the same order or even higher (typically every $\sim 3\mu\text{s}$) than the precision of the onset determination of the cryo-pulses. As the ToF of the neutrons is orders of magnitude smaller ($\Delta t_n \approx 50\text{ns}$) than the precision of the triple-coincidence time, the time of the pulse in the neutron detector holds for the time of interaction in the CaWO_4 cryodetector. In the search margin ($\pm 1\text{ms}$), one expects a constant background originating from accidental coincidences and an accumulation of events at $\Delta t_{\text{triple}} \approx 0\text{ms}$. Figure 9.4 shows a Δt_{triple} -distribution from a five-day measurement campaign (beamtime August 2009). A more detailed discussion is given in chapter 9.

Chapter 9

Results

During the year 2009 four beamtimes of about one week length each were performed. The first two measurement campaigns (February 2009, June 2009) were commissioning beamtimes and have been used to reach a better understanding of the complex accelerator setup (especially the challenging pulsing devices) and to test the new VME-based data acquisition, which was developed in [36]. The results of several tests and acquired data have improved the understanding of the experiment significantly. With the knowledge obtained in these beamtimes, improvements on the experimental setup have been made (see chapter 7). Thus - during the beamtime in August 2009 - it was possible to take data for ~ 6 days. The data acquired in this measurement campaign is analysed and reported in this chapter.

An additional beamtime in October 2009 (~ 7 days) is not yet analysed, but the data analysis is in progress. An discussion on this beamtime is given in section 10.3

9.1 Energy Spectrum of the Neutron Beam

The Time-of-Flight (ToF) spectrum of the neutrons is measured by the neutron detector positioned at a scattering angle of 0° at a distance of ~ 113 cm from the hydrogen cell (see chapter 7). A typical ToF distribution of the beamtime in August 2009 is shown in figure 9.1, where events are plotted in black. Neutron events (plotted in grey) are selected by applying a neutron/gamma discrimination cut (see section 8.3.2). Due to technical constraints of the pulsing devices - only for this beamtime - the spectrum exhibits a double-bunch structure. Besides the main gamma-peak at ~ 610 ns, there appears a secondary gamma-peak at ~ 710 ns, that is shifted by 100ns due to a feature of the 5MHz-clock of the buncher device. About 20ns later than the respective gamma-peaks, the fastest neutrons of $\sim 12 - 13$ MeV reach the detector. The prominent peaks at ~ 630 ns (~ 730 ns) represent neutrons of ~ 11 MeV from the resonant production in the hydrogen cell (see section 7.1.3) and at later flight times neutrons with lower energies reach the detector.

The double-bunch structure does not corrupt the coincidence search, since these two distributions are separated by the analysis software and thus can be combined to one single peak with a higher intensity. However, some problems with this adjustment did occur (see chapter 10), hence effort was made to avoid double-bunch structures. During the beamtime in December 2009 a different bunching method was chosen and a single-bunch structure was achieved.

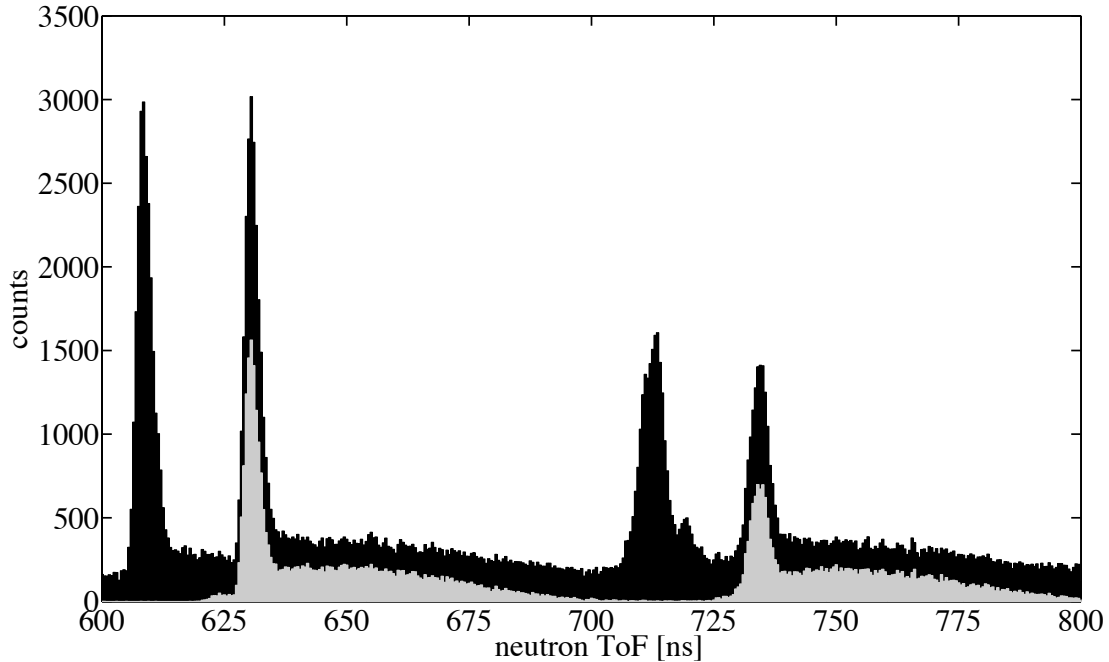


Figure 9.1: Typical ToF spectrum measured with the PMT at 0° scattering angle and a distance of $\sim 113\text{cm}$ from the hydrogen cell. The double-bunch structure (at $\sim 600 - 700\text{ns}$ and $\sim 700 - 800\text{ns}$) is a feature of the bunching devices (see text). The indiscriminated events are plotted in black, whereas neutrons are indicated in grey. Details concerning the neutron spectrum are given in the text .

Using equation 6.3 the neutron-energy spectrum can be obtained (figure 9.2). The measured spectrum - plotted in grey - is fitted best by a sum of a Gaussian centered at $\sim 10.6\text{MeV}$ and an exponential. The spectra is rising exponentially towards lower energies down to the threshold of the PMT at $\sim 1.5\text{MeV}$. Due to the good consistency of data and fit, the exponential curve is extrapolated to zero.

9.2 Coincident Events

9.2.1 Determination of Triple-Coincidence Events

Due to changes in the working points of the cryodetectors, $\sim 1\text{day}$ of data taking from the $\sim 6\text{day}$ data-set of the beamtime in August 2009 has to be discarded, hence the data analysis (described in section 8) is applied on a five-day data-set. From the $\sim 4,000,000$ pulses recorded by each cryodetector, only $\sim 80,000$ events ($\sim 2\%$) fulfill the triple-coincidence condition (see section 8.3.4). A yield plot, where the light yield is plotted versus the phonon energy of the remaining events is shown in figure 9.3.

The event distribution of these coincident events in the time margin Δt_{triple} of $\pm 1\text{ms}$ is shown in figure 9.4. As expected, this histogram shows a constant background due to

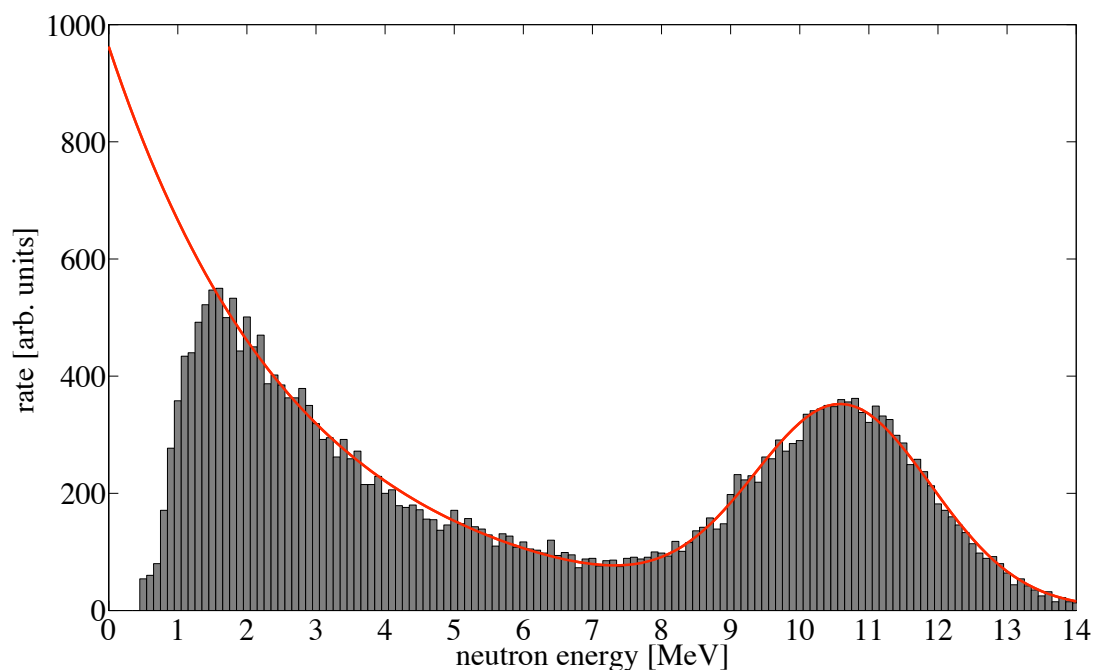


Figure 9.2: Typical neutron-energy spectrum of the beamtime in August 2009. The prominent peak at $\sim 10.6\text{MeV}$ originates from the resonant production of neutrons in the hydrogen cell. The spectrum is well fitted by a sum of a Gaussian and an exponential (red curve). The exponential is extrapolated to zero. For details see text.

accidental coincidences and an accumulation at $\Delta t_{\text{triple}} \approx 0$ (see section 8.3.4). The grey bars indicate the uncut data, whereas the black distribution represents the neutrons, that are cut graphically in the yield plot (lower band in figure 9.3). Figure 9.4 shows events of the energy range between 20keV (separation threshold of the cryodetector) and 2MeV. Higher energies are not of interest, since neutrons of $\sim 11\text{MeV}$ induce nuclear recoils only up to $\sim 1.1\text{MeV}$ for a scattering angle of 80° .

The accumulation around $\Delta t_{\text{triple}} = 0\text{ms}$ exceeds the background significantly within $\pm 10\mu\text{s}$ around the peak position. Since the jitter of the onset time of the cryodetector pulse is in the order of $\sim 10\mu\text{s}$, events in the time interval of $-5\mu\text{s} \leq \Delta t_{\text{triple}} \leq 15\mu\text{s}$ are selected. The interval contains 639 events ($\sim 0.015\%$ of all events in the data set) with a significant background of ~ 300 events. After the neutron cut in the yield plot of the cryodetector, 82 events remain with a expected background of ~ 23 ($\sim 27\%$). This background, which is due to accidental coincidences, is derived by calculating the mean value of coincidences to the left and right of the accumulation in figure 9.4.

9.2.2 Distribution of Triple-Coincidence Events in Time

For each time-of-flight value of the triple-coincidence neutrons and thus for a discrete energy of the incident neutrons, three population of recoil energies in the phonon channel should appear due to kinematic reasons (see chapter 6). In reality, however, not only monoenergetic neutrons are produced, but a continuous neutron spectrum (see figure

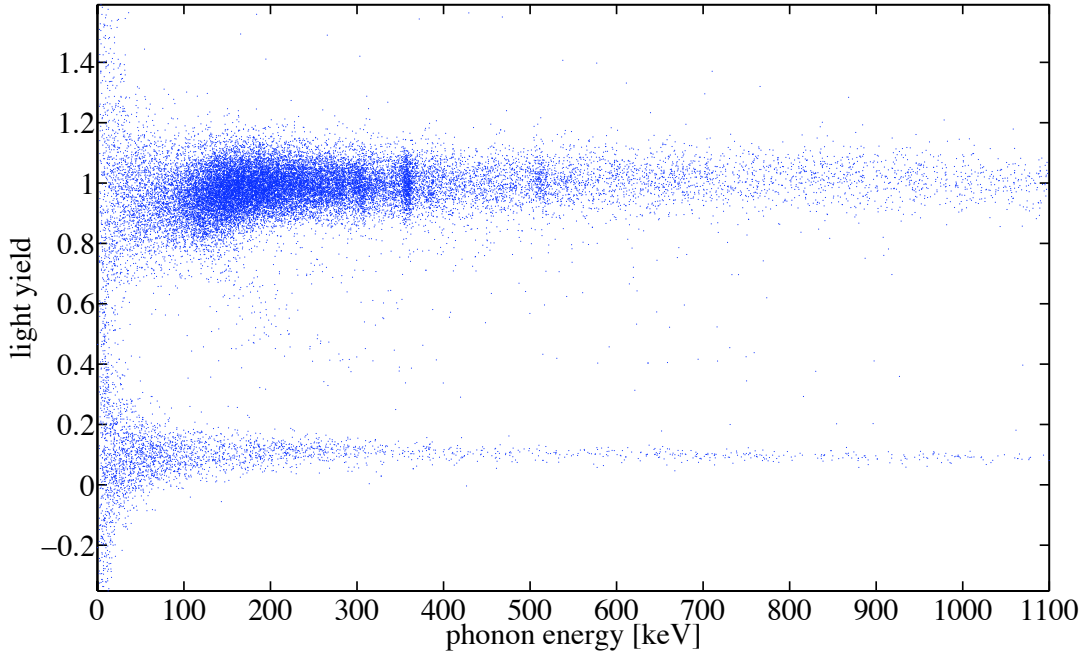


Figure 9.3: Light yield plotted versus the phonon energy for all triple-coincidence events of the ~ 5 day-measurement campaign, where in addition to the neutron beam a ^{133}Ba source was present. The upper band originates from gamma-induced electron recoils, the lower band from neutron-induced nuclear recoils. The light yield was normalized to one for electron recoils at an energy of 356.0 keV (prominent γ -line of ^{133}Ba). Events between the bands are due to inelastic scattering off tungsten.

9.2). The correlation between recoil energy in the phonon channel and neutron ToF is calculated in the following.

The recoil energy E_R is proportional to the energy E_n of the incident neutrons (see equation 6.1):

$$E_R = 2E_n \frac{m_n \cdot m_x}{(m_n + m_x)^2} (1 - \cos \Theta_{CM}) \quad (9.1)$$

$$= K(m_x, \Theta_{CM}) \cdot E_n \quad (9.2)$$

where Θ_{CM} is the scattering angle in the center-of-mass system, m_x the mass of the recoiling nucleus and m_n the neutron mass. The total flight time of the neutrons Δt on their path before scattering ($s_1 \approx 37\text{cm}$) and after scattering ($s_2 \approx 173\text{cm}$) can thus be calculated as (non-relativistic calculation, error $< 1\%$)

$$\Delta t = s_1 \cdot \sqrt{\frac{m_n}{2E_n}} + s_2 \cdot \sqrt{\frac{m_n}{2(E_n - E_R)}} \quad (9.3)$$

$$\approx s \cdot \sqrt{\frac{m_n}{2(E_n - E_R)}} \quad (9.4)$$

where $s = s_1 + s_2$ and the error of the approximation made from 9.3 to 9.4 is $\sim 1\%$, taking into account that $s_1/s_2 \approx 0.2$. The recoil energy can be calculated in dependency

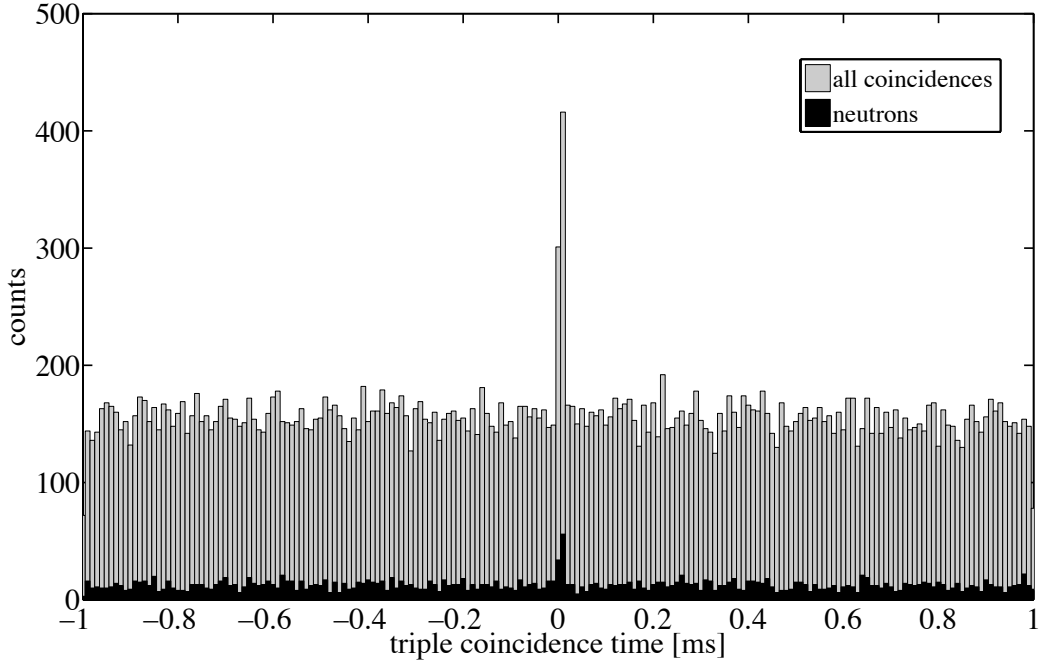


Figure 9.4: All triple coincidences (grey) and events after a cut on neutrons in the cryodetector (black) are plotted versus the time difference between the time of double-coincidence (see section 8.3.3) and the onset of the pulse in the cryodetector within a time margin of ± 1 ms. The constant background is due to accidental coincidences, whereas the accumulation of events around $\Delta t_{\text{triple}} = 0$ ms is due to real coincidences.

of Δt :

$$E_R = \frac{K(m_x, \Theta_{CM})}{1 - K(m_x, \Theta_{CM})} \frac{m_n}{2} \frac{s^2}{(\Delta t)^2} \quad (9.5)$$

In figure 9.5 the recoil energy of the 82 triple-coincidence events remaining after data-analysis cuts are plotted versus the ToF. In addition, the theoretical curves for the three elements in CaWO_4 obtained by equation 9.5 are shown.

In spite of low statistics, three populations of events around the respective theoretical curves are visible. In order to quantitatively identify the recoiling nucleus, an error estimation was carried out.

9.2.3 Error Estimation

The following errors are considered:

- Statistical error in distance s , mainly due to the size of the PMT cell ($\Delta s_{\text{stat1}} = 5$ cm), the size of the crystal in the cryodetector ($\Delta s_{\text{stat2}} = 1$ cm) and the size of the hydrogen cell ($\Delta s_{\text{stat3}} = 1.5$ cm).
- Systematical error due to the uncertainty in the measuring method of the distance s : $\Delta s_{\text{syst}} = 3$ cm. The difficulties in measuring the distance are discussed in section 11.1.5.

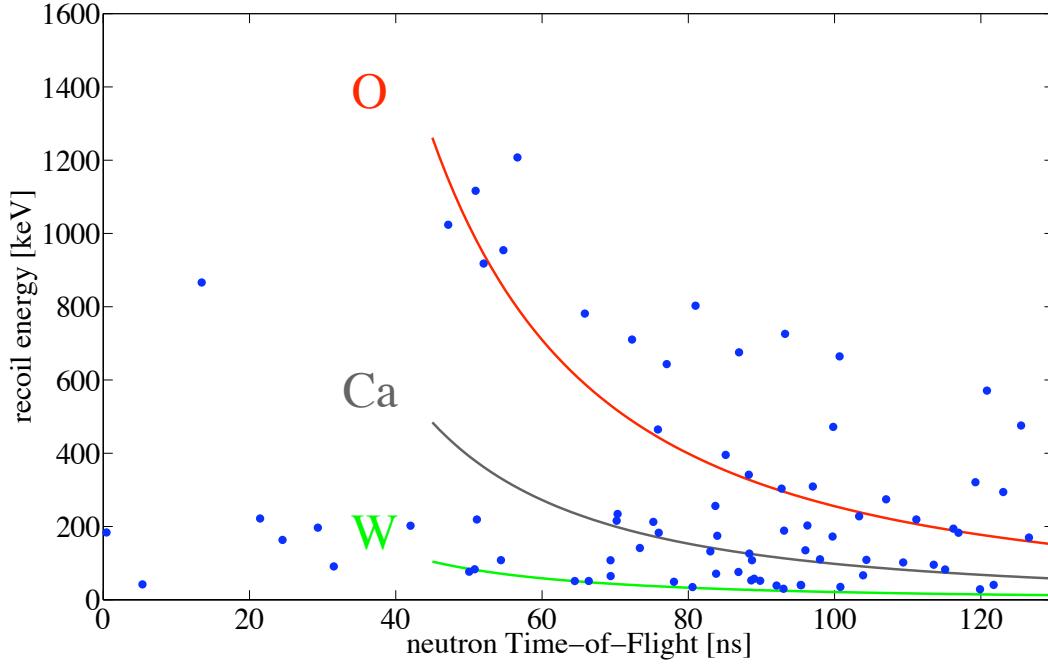


Figure 9.5: The recoil energies of the 82 triple-coincidence neutron-events are plotted versus the neutron ToF. Events with a ToF larger than 130ns have not been recorded due to technical reasons (explained in section 10.2.3). The three lines indicate the calculated recoil energies of the three elements in CaWO_4 for different ToF values.

- Statistical error in determination of angle due to the size of the PMT cell: $\Delta\Theta_{\text{stat}} = 2^\circ$.
- Systematical error in angle due to uncertainties in the positioning method of the detector array and the vertical alignment of the CaWO_4 crystal: $\Delta\Theta_{\text{syst}} = 2^\circ$.
- Statistical error in the flight time due to the uncertainty of the buncher ($\Delta t_{\text{stat1}} = 2\text{ns}$) and the PMT ($\Delta t_{\text{stat2}} = 2\text{ns}$). Improvements concerning these error are discussed in section 11.1.8.
- Systematical error to the finite resolution of the phonon detector: $\Delta E_{\text{phonon}} = 9\text{keV}$ (constant).

The total statistical error of the recoil energy E_R is calculated by using the Gaussian error propagation [52] of equation 9.5:

$$\Delta E_R(\text{stat}) = \sqrt{\sum_{i=1}^3 \left(\frac{\partial E_R}{\partial s} \cdot \Delta s_{\text{stati}} \right)^2 + \sum_{i=1}^3 \left(\frac{\partial E_R}{\partial t} \cdot \Delta t_{\text{stati}} \right)^2 + \left(\frac{\partial E_R}{\partial \Theta} \cdot \Delta \Theta_{\text{stat}} \right)^2} \quad (9.6)$$

The total systematical error of E_R is the linear sum of the error-propagation terms:

$$\Delta E_R(\text{syst}) = \frac{\partial E_R}{\partial \Theta} \cdot \Delta \Theta_{\text{syst}} + \frac{\partial E_R}{\partial s} \cdot \Delta s_{\text{syst}} + \Delta E_{\text{phonon}} \quad (9.7)$$

The sum of the total statistical error and the total systematical error results in the total error

$$\Delta E_R(K(m_x, \Theta_{CM}), t) = \Delta E_R(\text{stat}) + \Delta E_R(\text{syst}) \quad (9.8)$$

In figure 9.6 it is plotted for oxygen recoils together with its main components versus the neutron ToF.

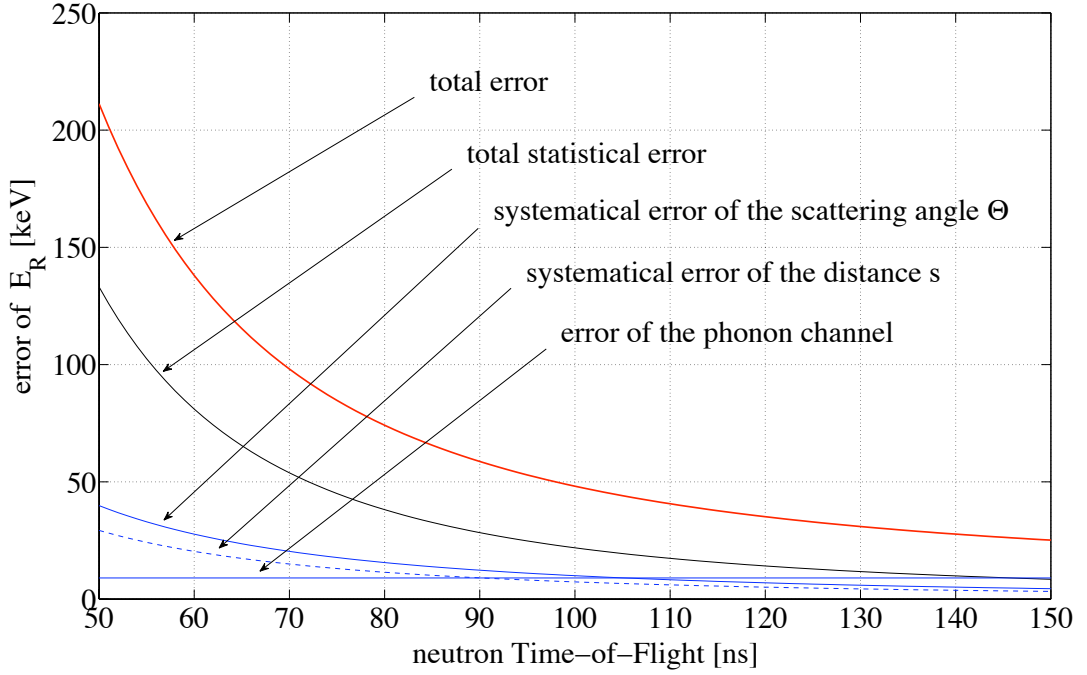


Figure 9.6: Different contributions to the error of the oxygen-recoil energy are plotted versus the neutron ToF. The errors of calcium and tungsten only differ by a constant factor.

9.2.4 Identification of the Recoiling Nuclei

In order to identify the recoiling nucleus, from which the neutrons scattered off, the calculated recoil energy E_R (see section 9.2.2) is shown with its total error ΔE_R (see section 9.2.3) for the three components of CaWO_4 in figure 9.7. E_R is plotted in thick lines, the error bands $\pm \Delta E_R$ are plotted in thin lines for each element. Within the thin lines the nuclear-recoil events for the respective elements are expected in agreement with the estimated errors, whereas events outside there bounds are due to accidental coincidences.

Events with a low recoil energy at short ToF ($< 40\text{ns}$) and events with a large recoil energy at large ToF ($> 80\text{ns}$ and well above the oxygen band) are cut and treated separately (20 events). This is discussed in more detail in chapter 10.

Altogether 62 events remain.

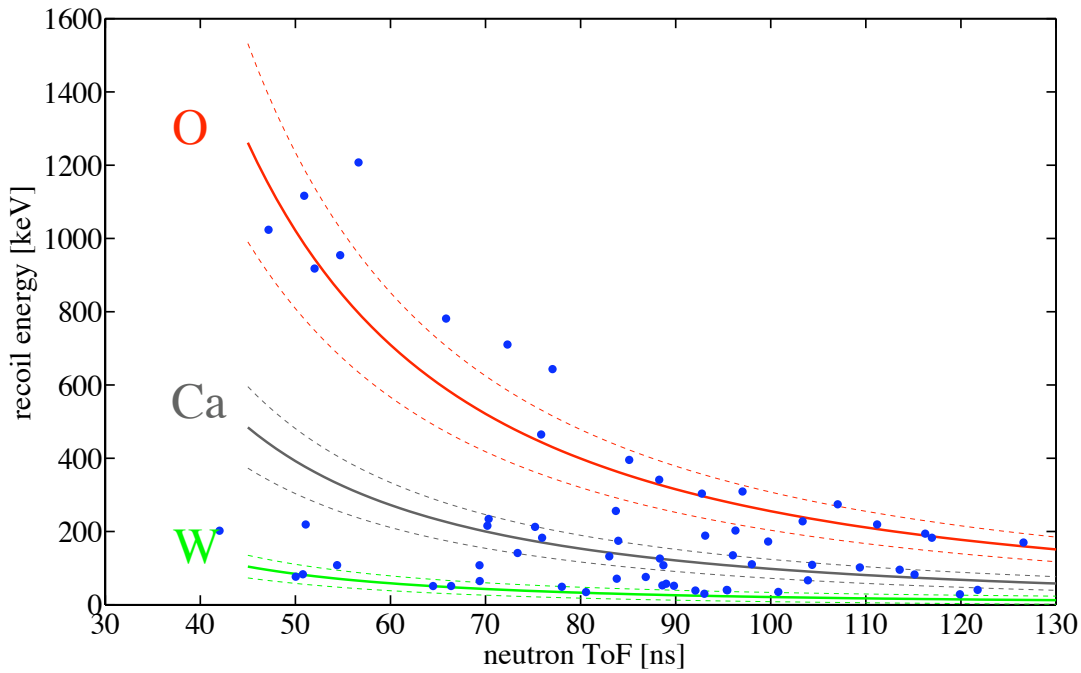


Figure 9.7: The recoil energies of the 62 triple-coincidence neutron-events, that remain after cuts, are plotted versus the neutron ToF. Full lines indicate the calculated recoil energies for different ToF and thin lines the acceptance bounds obtained by the error estimation in section 9.2.3 for O, Ca and W. The cuts are explained in the text.

After all cuts, 14 nuclear-recoils off oxygen, 14 off calcium and 7 off tungsten remain. 16 events are well separated from the calculated bands and thus related as background. 11 events remain on or close to the acceptance-bounds and thus - with this low statistics - no identification is possible. For the further analysis, only the 35 well-identified events are taken into account.

9.3 Recoil Rates

Using the ENDF data-base (see section 6.3) the expected energy-dependent cross-section can be calculated for different scattering angles. In figure 9.8 the cross-sections at 80° for the three elements in CaWO_4 (see figure 6.4 in section 6.3) is convoluted with the energy spectrum of the neutrons from the accelerator (see figure 9.2) to obtain the expected recoil rates.

The energy-dependent cross-sections of calcium and oxygen exhibit a large number of resonances (mainly below 6MeV) and thus strong fluctuations. In order to compare these curves with the actual data, a running-average filter [53] was applied to the cross-sections. This makes the spectra smoother and increases the comparability to the measured data of low statistics.

In figure 9.9 the averaged cross-sections are shown together with a histogram of the

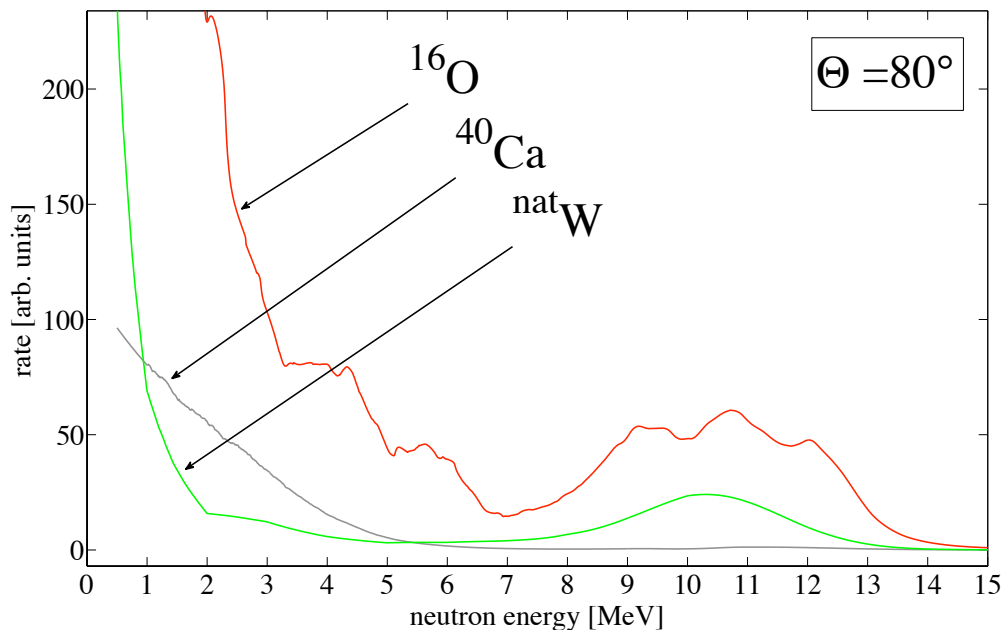


Figure 9.8: Expected recoil rates for the three elements of CaWO_4 at a scattering angle of 80° are plotted versus the incident neutron energy. The cross-sections calculated in section 6.3 are convoluted with the measured neutron-energy spectrum. The stoichiometric conditions in CaWO_4 and the natural isotope ratio of tungsten are included. The spectra are smoothed by applying a running-average filter (see text).

recoil events identified with the respective elements in CaWO_4 (see section 9.2.4). The neutron energy E_n inducing recoils of the respective element is determined using equation 9.3 and the measured recoil energy E_R and ToF Δt . The calculated cross-sections are arbitrarily normalised, but the relation between oxygen, calcium and tungsten has been kept.

There is good agreement between expected and measured recoil rates, as discussed in section 10.1.

9.4 Quenching Factors

The statistics obtained during this measurement campaign are too low to actually derive reliable Quenching Factors (QF) for the three elements of CaWO_4 . However a tendency can be seen and verifies the ToF-measurement method described in this work. Table 9.1 summarizes the values for the QFs (as defined in section 5.1) obtained for the 14 oxygen, 14 calcium and 7 tungsten events identified in section 9.2.4.

The results concerning the QFs are discussed in more detail in section 10.1.

Energy Range	QF(O)	QF(Ca)	QF(W)
$E_R = 9 - 12\text{MeV}$	11	-	42
$E_R = 0 - 12\text{MeV}$	10	8	25

Table 9.1: Quenching Factors (QF) for the three elements of CaWO_4 measured at different energy ranges. Due to the very low statistics (event rates can be seen in figure 9.9), reliable QFs cannot be stated, but a tendency can already be seen. Discussion in chapter 10.

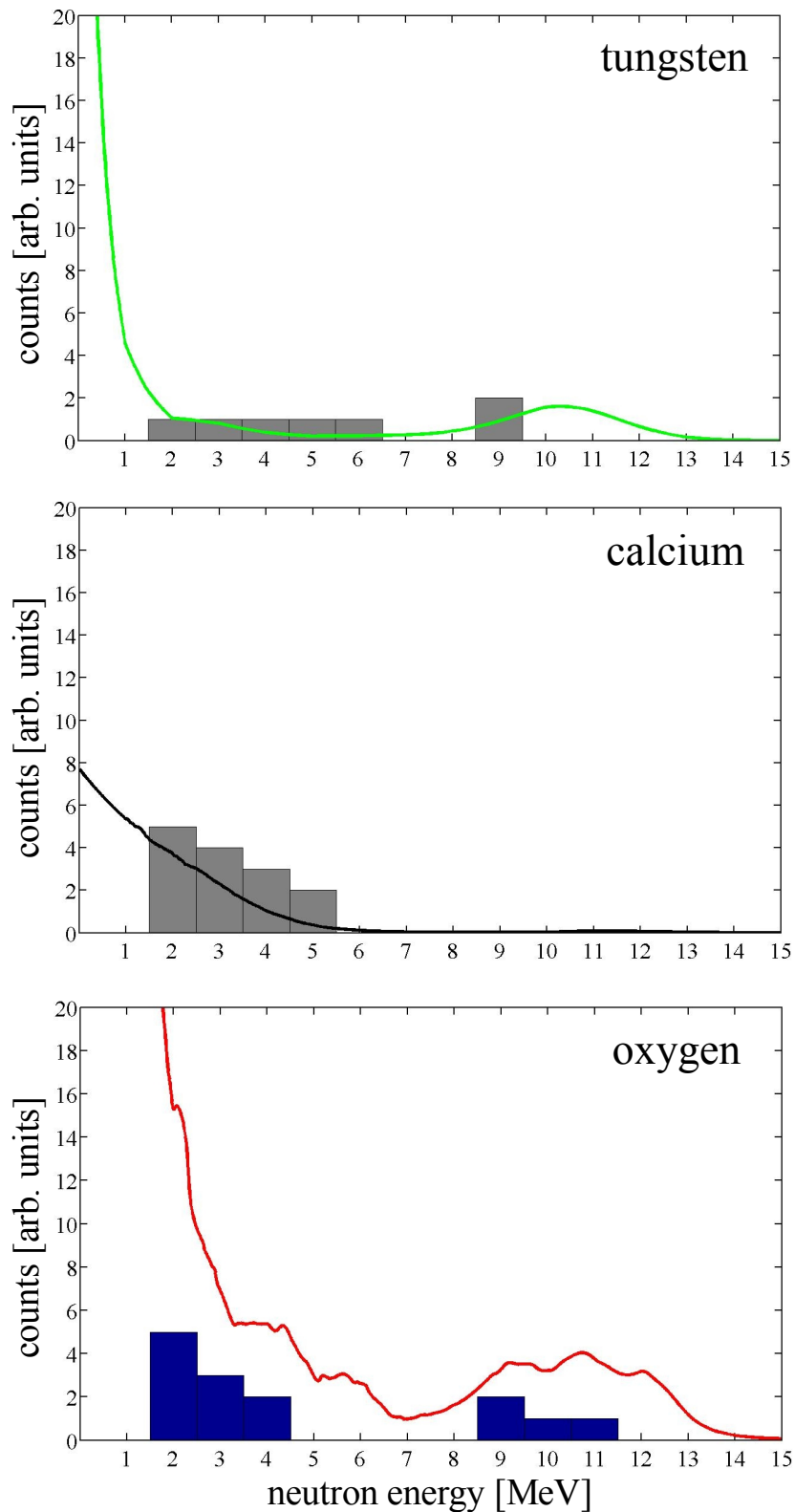


Figure 9.9: Expected recoil rates (full lines) for the elements of CaWO_4 at a scattering angle of 80° is compared with the actual data (histogram) measured in this measurement campaign. The calculated cross-sections are arbitrarily normalised, but the relation between oxygen, calcium and tungsten has been kept.

Chapter 10

Discussion of the Results

In this chapter, the results obtained in chapter 9 are discussed and problems with the experimental setup are pointed out.

10.1 Consistency of the Measured Data

In the following, several consistency checks for the measured data are given:

- A basic proof for consistency is that an **accumulation of triple-coincidence events** appears at $\Delta t_{\text{triple}} \approx 0ms$, which is explained in section 8.3.4 and shown in figure 9.4. These events must originate from actual coincidences between the accelerator bunch, one detector of the detector array and the cryodetector, whereas accidental coincidences cannot explain an accumulation, as they are expected to be uniformly distributed.
- Further, the **signal-to-background ratio** for events from the accumulation around $\Delta t_{\text{triple}} \approx 0ms$ in figure 9.4 increases from 2:1 to 4:1, if only neutrons - instead of all events - are considered (see section 9.2.1). This is reasonable, as the gamma rate exceeds the neutron rate in the cryodetector by a factor of ~ 10 and thus accidental coincidences should originate mainly from gamma events. This confirms, that the origin of the accumulation is mainly due to neutron-induced nuclear recoils.
- As expected by simple kinematics (described in section 9.2.4), **three populations of recoil energies** appear, if the triple-coincidence events are plotted versus ToF (see figure 9.7). This distribution is in good agreement with the calculated recoil energies for the three elements in CaWO_4 .
- With the help of figure 9.7 the following **background estimation** can be performed: As described in section 9.2.4, out of 62 events, 35 are identified as nuclear recoils of one of the three elements in CaWO_4 and 16 are clearly regarded as background. As accidental coincidences are uniformly distributed in time and - in first approximation - also in recoil energy up to an energy of 1.5 MeV, they will also populate the region between the acceptance bounds of the three elements. For this reason, a simple geometrical estimation can be made to approximately derive the total number of background events in this plot. The acceptance regions cover about 16% of the whole energy-time plane, that contains 62 events. Thus a total

background of $\frac{16}{0.84} = 19$ events is estimated for the entire region of interest. This is in good agreement with the expected background rate of ~ 16 events, as derived from the triple-coincidence plot (see figure 9.4 in section 9.2.1).

- The **expected recoil rates** shown in figure 9.9, that are calculated from the ENDF database [38], are in agreement with the measured data. In particular the distribution of events at high energies, from about 9 to 12MeV (ToF of $\sim 45 - 55$ ns), is in remarkable consistency with the expectation that only oxygen and tungsten recoils are found.
- In order to **exclude systematical errors in the data analysis**, a number of consistency tests have been performed. For example it has been checked, if the events - remaining after all coincidence searches - are equally distributed over all neutron detectors and over the whole measurement campaign. No conspicuous data has been found.
- The obtained **values for the QFs** are - in spite of low statistics - a reasonable confirmation for the correctness of the measurement. From earlier measurements, the QF for oxygen is known with high precision (see table 5.1) at mK temperatures ($QF_{\text{oxygen}} = 10.0 \pm 0.1$) [16]. The QF for oxygen (~ 10) obtained from the 14 events in the oxygen acceptance-region is in very good agreement with these earlier results. The seven events for tungsten result in a higher QF (~ 25), which confirms the tendency to higher QFs for heavier atoms (the QF of tungsten is expected to be 35_{-9}^{+19} [16]). Nevertheless, the events identified as calcium recoils do not support this tendency, as the QF is measured to be ~ 8 , which is in disagreement with earlier results ($QF_{\text{calcium}} = 19 \pm 2.5$) [16]. This is assumed to be mainly due to the lower resolution of the light detector and can be seen in figure 8.14 as a significant broadening of the nuclear recoil band below ~ 200 keV. Thus - at lower recoil energies - higher statistics are mandatory to make reliable predictions.

10.2 Problems with the Present Setup

Low statistics are an intrinsic problem of the experimental method, since a certain scattering angle is chosen and thus only a tiny solid angle is covered by the neutron detectors ($\sim 0.5\%$). Thus the experimental setup as well as the data analysis has to be made as effective as possible. The following problems that occurred during the past beamtimes are discussed and suggestions for solutions are given.

10.2.1 Large Mass Surrounding the Cryodetector

As described in section 9.2.1, ~ 300 of all triple-coincidence events are regarded as actual coincidences. One would expect that nearly all of these events should be detected as neutrons in the cryodetector, since a cut on neutrons is already performed in the neutron detectors of the detector array. The number of actual events remaining after a cut on the nuclear recoil band in the cryodetector module (~ 60) does not confirm this assumption. Only one-fifth of the neutrons, that fulfill the double-coincidence and ToF conditions (see section 8.3.3) actually scatter off the CaWO_4 crystal. The rest - four-fifth - of the

neutrons produce electron-recoil events in the cryodetector.

Thus, these neutrons must scatter in the nearby material of the CaWO_4 crystal and produce gammas by inelastic interactions. This is reasonable, as the mass of the detector holder ($\sim 0.5\text{kg}$ of copper, described in section 7.2.2) is ~ 17 times larger than the mass of the CaWO_4 crystal ($\sim 30\text{g}$) and the cryodetector covering a large solid angle will measure a significant part of the produced gammas. Additional material is due to the He-dewar (Al) and parts of the cryostat around the detector module (mainly copper and steel).

This problem can be solved by significantly reducing the mass around the detector, mainly by re-designing the detector module (see section 11.1.1). Also possible changes on the cryostat itself and the He dewar will be discussed in section 11.1.2.

Of course, a reduction of the mass surrounding the detector alone will not increase the number of scatterings in the CaWO_4 crystal, but - since the gamma-rate is reduced and thus less pile-up events are produced - the neutron-rate can be increased by raising the beam intensity of the accelerator. For a quantitative description of these effects a Monte-Carlo simulation is necessary (see section 11.1.6).

10.2.2 Resolution of the Light Detector

The resolution of the light detector decreases significantly at lower energies, which is visible in a broadening of the nuclear-recoil band in the energy region below $\sim 200\text{keV}$ (see for example figure 8.14). This is mainly due to the decreasing signal-to-noise ratio at low energies. As the final goal will be measuring the QFs in the region of interest of the CRESST experiment (10-40keV), an improvement of the light detector is necessary. Otherwise much better statistics would be required. The resolution of the light detectors used in the CRESST experiment is higher, and the broadening of the nuclear recoil band appears at lower energies ($\sim 60\text{keV}$, see figure 5.2).

The resolution can be improved by increasing the light-collection in the detector housing, as discussed in section 11.1.1. In addition, there is a lot of very promising activity at our institute concerning the improvement of light detectors by using Neganov-Luke amplification techniques (see section 11.1.3) [12].

10.2.3 Double-Bunch Structure

At the beamtime in August 2009, a double-bunch structure was provided by the bunching-devices of the accelerator (see section 9.1). Unfortunately, there is a significant overlap of neutron events of the primary and the secondary bunch in the ToF spectrum. This can be seen in figure 10.1, where the neutron ToF of all triple-coincidence events are plotted in a histogram. A significant overlap between about 100ns to 180ns is visible. Events from both bunches are taken for the analysis of the experiment. On the one hand low-energetic neutrons from the first bunch can mimic high energetic neutrons ($\text{ToF} < 40\text{ns}$) at low recoil energies. On the other hand, high-energetic neutrons from the secondary bunch appear as events with high recoil energies at large ToF values (above the oxygen acceptance-region at $\text{ToF} > 80\text{ns}$). Fortunately, these events can be cut (see figure 9.7). However, parasitic events inside the acceptance bounds of the three elements of CaWO_4 cannot be excluded. The sudden drop in the event rate at about 230ns is due to a threshold in the coincidence-search algorithm.

For future beamtimes a method was developed to avoid this double-bunch structure and provide only single bunches with sufficient intensity.

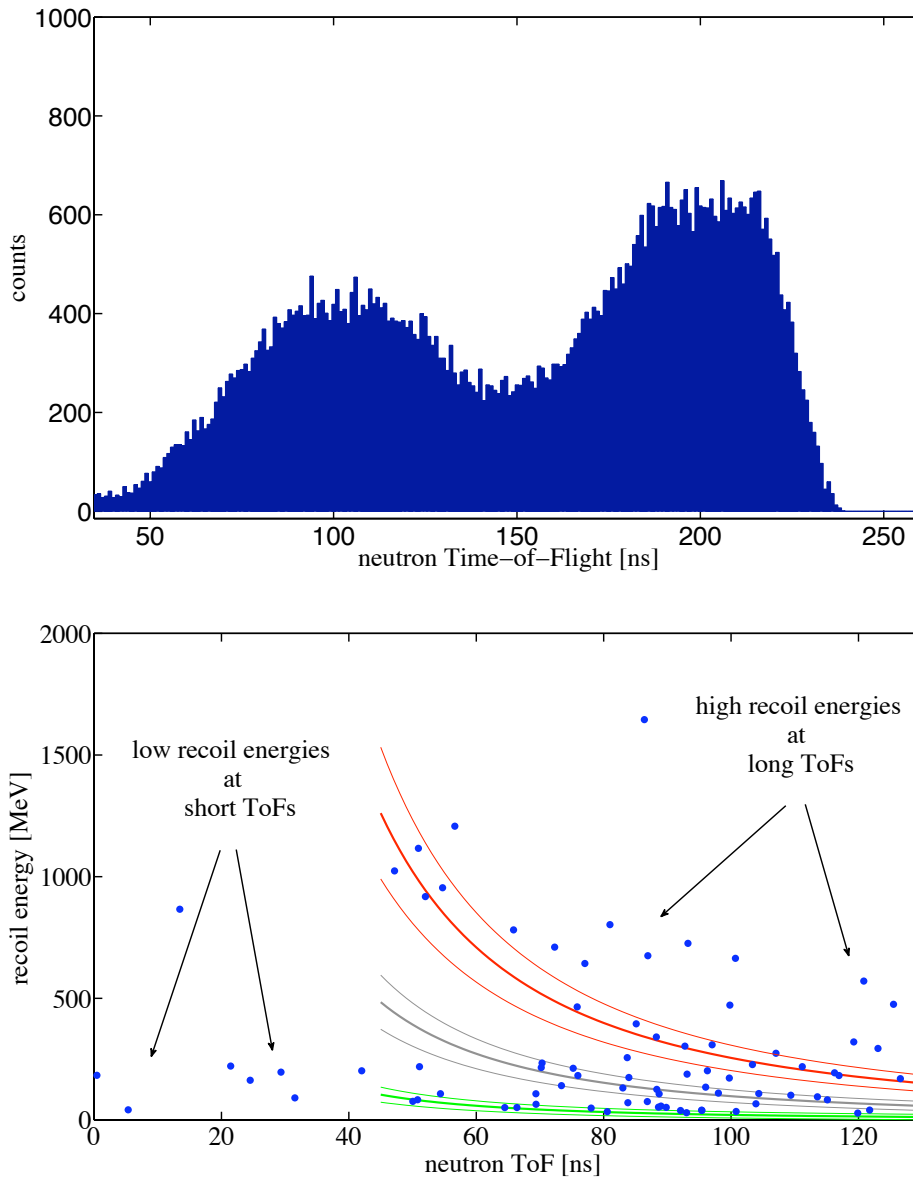


Figure 10.1: Top: Distribution of the ToF values of all triple-coincidence events originating from the double-bunch structure of the beam. The significant overlap between events from the primary and the secondary bunches between ~ 100 and ~ 180 ns is clearly visible. Bottom: Parasitic events that most probably originate from the significant overlap of the primary and secondary bunch are indicated. For details concerning this plot see section 9.2.2.

10.3 Consequences for the Beamtime in October 2009

With the knowledge of earlier beamtimes, several improvements and changes have been performed for the beamtime in October 2009. The bunching of the accelerator (see

section 10.2.3) and also the scattering angle and thus the positions of the PMT arrays have been changed. As one can see from figure 6.3, the differential elastic cross-section for tungsten is higher by a factor of ~ 6 at a scattering angle of 45° compared to 80° . For neutron energies from ~ 8 to ~ 14 MeV, tungsten makes the dominant contribution to the total recoil rate for this scattering angle, as can be seen in figure 10.2.

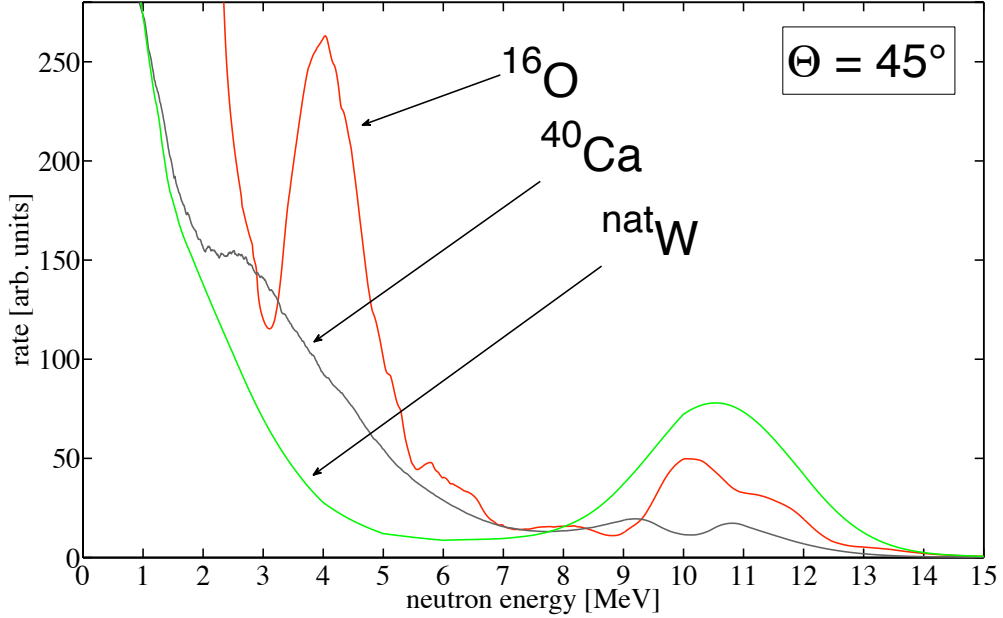


Figure 10.2: Expected recoil rates for the three elements of CaWO_4 at a scattering angle of 45° are plotted versus the incident neutron energy. The cross-sections calculated in section 6.3 are convoluted with the measured neutron-energy spectrum. The stoichiometric conditions in CaWO_4 and the natural isotope ratio of tungsten are included. The spectra are smoothed by applying a running-average filter.

However, to avoid that direct (non-scattered) neutrons from the hydrogen cell can reach the neutron-detector array, the polyethylen shielding has to be positioned inside the opening angle of the neutron beam. This leads to an increase of the number of accidental coincidences. In addition, the influence of the shielding on the neutron spectrum has to be investigated. In order to test such a setup, one detector array was positioned at 45° . The other detector array remained at a scattering angle of 80° , but the distance s to the cryodetector was reduced from ~ 170 cm to ~ 100 cm to increase the number of coincidences, since the detection probability increases with $1/s^2$ towards lower distances. The data-analysis of this beamtime is ongoing and results will be presented in [36].

Chapter 11

Outlook

The results obtained in this work are very promising and show that the Time-of-Flight measuring-method in connection with cryodetectors has been a good choice for the determination of the Quenching Factors (QF) in the region of interest of the CRESST experiment (recoil energies from ~ 10 to ~ 40 keV). Clearly, in order to obtain reliable values of the Quenching Factors for CaWO_4 , more statistics and further improvements are necessary. In the following, some improvements and solutions for the problems discussed in chapter 10 are suggested.

11.1 Future Improvements

11.1.1 New Design of the Detector Holder

In the present setup, the holder of the cryodetectors is too bulky and gives rise to parasitic scattering of neutrons (as discussed in section 10.2.1). The CaWO_4 crystal is surrounded by a cylindrical structure made of copper and a wall thickness of ~ 5 mm. The mass of the holder material exceeds the mass of the detector by a factor of ~ 10 . Much less mass is actually required for the stability of the housing and the support of the detector devices. A model for a new design could be the typical holder of a CRESST detector (see figure 2.3), which consists of copper rings - instead of massive plates - at the top and bottom to hold the CaWO_4 crystal and the light detector. Instead of a massive cylindrical housing made of copper, the crystal is surrounded only by a highly reflective foil (VM2000 [11]), with a negligible mass.

In addition, the clamps - presently made of bronze - should be replaced by ones that are coated by reflective silver or a highly reflective foil. This avoids absorption of light in the clamps, which - at present - cover a significant part of the crystal's face.

The re-design of the detector holder should also include a new construction of the connection between mixing chamber and detector holder. The mass of this construction should be reduced significantly, for example, by using hollow profile structures of copper instead of massive rods.

11.1.2 Changes of the Cryostat

The cryogenic detector is surrounded not only by the detector holder, but also by an onion-like structure of vessels of the cryostat. The main mass-contributions are the Inner

Vacuum Chamber (IVC) made of stainless steel with a wall-thickness of $\sim 3\text{mm}$, radiation shields made of Cu with a total thickness of $\sim 2\text{mm}$, the vacuum-isolated He dewar made of stainless steel ($\sim 2\text{mm}$) and the outer dewar made of Al ($\sim 5\text{mm}$). It has to be considered that scattering neutrons have to pass these materials twice. These vessels cannot be removed, as they are necessary for the operation of the cryostat. However, the masses can be reduced to decrease the number of parasitic scatterings of neutrons and gammas. This has to be properly investigated in cooperation with the institute's workshop in order to assure the functionality and security of the cryostat.

11.1.3 Neganov-Luke Light Detector

At our institute, light detectors based on the Neganov-Luke effect [54] [55] have been developed and prototypes have successfully been tested [12]. The working principle relies on an amplification of the signal induced by photons that are absorbed by the Si substrate of a light detector: A voltage (V) is applied by additional Al-electrodes, which are evaporated onto the Si absorber (see figure 11.1). Electron-hole pairs that are produced by an incident photon, are accelerated by this so-called Neganov-Luke voltage and generate additional phonons in the absorber. Thus the signal is amplified before being measured by the TES. Measurements show, that the signal-to-noise (S/N) ratio of pulses in the light detector can be increased by a factor of ~ 10 with an applied voltage of $\sim 100\text{V}$ compared to an ordinary light detector (see figure 11.1) [12].

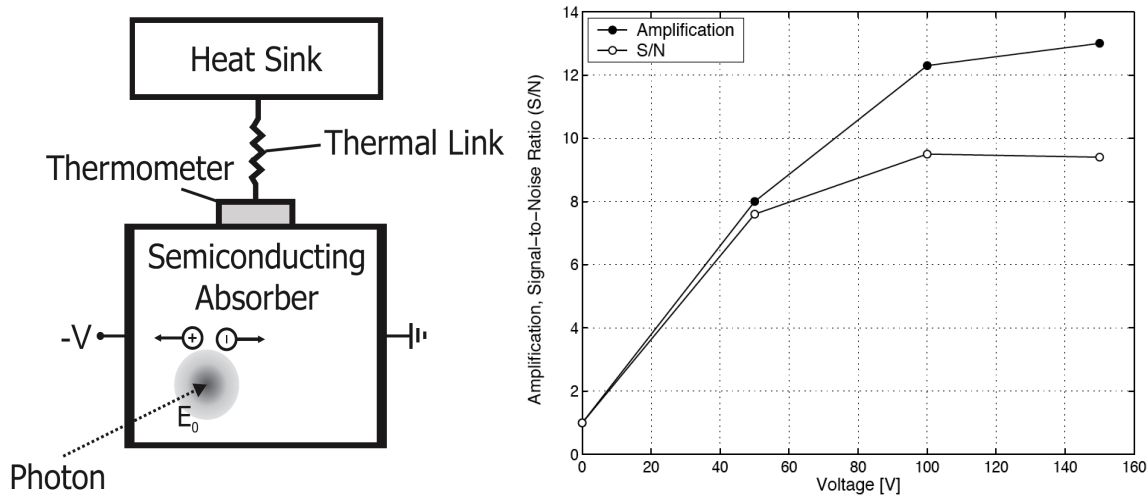


Figure 11.1: Left panel: Working principle of a Neganov-Luke detector with an additional voltage V applied at electrodes evaporated onto the semiconducting absorber (e.g. a Si single crystal). Right panel: The amplification and the signal-to-noise (S/N) ratio are plotted versus the applied voltage V for a measurement with a Neganov-Luke light detector [12]. Above $\sim 100\text{V}$, no further increase of the S/N ratio can be seen.

At the moment, measurements with a CRESST-like detector module equipped with a Neganov-Luke light detector are ongoing. If successful, such a detector should be installed at the scattering experiment as soon as possible.

11.1.4 Additional Large-Area Neutron Detectors

Higher statistics can be obtained by increasing the area covered by the neutron detector arrays. In his work (see section 7.4), a new design of a neutron detector is presented, that increases the detection volume per readout-channel by a factor of ~ 5 . A prototype was running during the beamtime in October 2009 and preparations to integrate more of these large-area detectors in the mounting system (see section 7.3.3) have been started.

11.1.5 Reduction of Systematical Errors

For future beamtimes, systematical errors can be reduced by a more exact measurement of the positions of the cryodetector as well as the PMT arrays. This is a challenging undertaking, because the position of the CaWO_4 crystal changes due to the large temperature change from room temperature to the mK range. In addition, the height of the cryostat above ground can change, as the whole cryogenic setup is mounted on air-dampers. With a further investigation of these effects and an exact measurement of the distances, the systematical error of the flight path of the neutrons Δs could be decreased to $< 1\text{cm}$.

In the same way, the systematical error of the scattering angle can be improved. If the exact vertical position of the CaWO_4 crystal is known, a more precise alignment of the PMT arrays will be possible.

11.1.6 Monte-Carlo Simulations

In order to investigate problems quantitatively and to allow to estimate the improvements due to specific changes of the setup, a Monte-Carlo simulation of the entire setup would be a powerful tool. This would, in particular, help to determine which masses contribute most to parasitic scattering of neutrons (discussed in section 10.2.1) and where efforts to reduce them should preferably be made. In addition, this experiment offers a great opportunity to compare experimental data with the results of simulations.

11.1.7 Update of the Analysis Software

As described in chapter 8, many events of the cryodetector have to be discarded ($\sim 50\%$) for different reasons. A large amount ($\sim 50\%$) of these unusable pulses are due to pile-up in the cryodetector. For the future, a software will be developed, which removes the second (and third, etc.) pulse of a pile-up event. Hence at least one pulse (namely the first) of a pile-up event can be treated as an ordinary pulse. However, if a second pulse is too close to the first, the pulse shape cannot be reconstructed, as the two pulses have too much overlap. Thus, at present no exact quantitative prediction of the increase of statistics can be given, but it should be in the order of $10 - 20\%$.

11.1.8 Improved Beam Monitoring System

The time resolution of the used PMTs is in the order of 3-4ns. As a consequence, the beam pulses of the accelerator cannot be further optimized, as the buncher is adjusted by minimizing the width of the beam-induced gamma-bunch measured by a PMT at a scattering angle of $\sim 0^\circ$ (see section 9.1). A minimum bunch width of $\sim 1\text{ns}$ is

possible with the pulsing setup of the accelerator. For a more exact measurement, a high-precision PMT with a lower time-jitter and a smaller scintillator volume should be installed. This would reduce the statistical error due to the bunch width of the neutron beam.

11.1.9 Application of the CRESST calibration system

As described in section 8.2.3, for the present experiment, the calibration of the phonon detector is achieved by a ^{133}Ba gamma-source and the light detector is calibrated by X-rays from a ^{55}Fe source. Although the detector response is fairly linear (see figure 8.13), no calibration points at low energies ($< 1.5\text{keV}$) are available in this setup. The CRESST experiment makes use of heater calibration pulses, that inject Ohmic heat of a known energy into the detector. Thus a finer calibration in the whole energy range of the detector can be achieved, as well as a stability check during a long-term measurement, since heater pulses can be injected continuously (typically every 30s). Both phonon and light detectors are separately calibrated by heater pulses [11]. The absolute energy-pulse height calibration can then be achieved with the 122keV gamma-line of a ^{57}Co source.

In the future, this calibration method should be taken over for the neutron-scattering experiment described in this work, as for the exact determination of the QF, full consistency with the CRESST experiment will be of great interest. As a side effect, one can get rid of the additional mass of the ^{55}Fe -source (and its holder) that is mounted below the light detector. This would help to further reduce the problems described in section 10.2.1.

11.2 New Target Materials for EURECA

In the framework of the future Dark Matter (DM) project EURECA (see section 4) with its different target materials, the neutron-scattering facility being unique in the world as an experimental setup for the measurement of Quenching Factors (QFs) at mK temperatures, will be a powerful tool. The energy of the neutrons produced by the accelerator ($\sim 11\text{MeV}$) is sufficient to measure light originating from nuclear recoils of heavy atoms (e.g. W or Bi). Once completed, after the realization of the improvements discussed in section 11.1, the setup and the data analysis will be ready to investigate different target materials within beamtimes of typically 2-4 weeks. A large range of suitable crystals are candidates for DM search. In the following a few examples are listed, which are presently under discussion.

- ZnWO_4 - first results show a higher radiopurity and light output ($\sim 110\%$ at 9K) compared to CaWO_4 [56].
- $\text{Bi}_4\text{Ge}_3\text{O}_{16}$ (BGO) - provides a higher light output ($\sim 125\%$ at 20mK) compared to CaWO_4 and has the heavy constituent Bi ($A\approx 209$) that is in the same order than W ($A\approx 184$) [57].
- Al_2O_3 doped with Ti^{3+} and Cr^{3+} - [58] shows encouraging results concerning energy threshold and resolution although this scintillator has an increased heat capacity. In addition, ^{27}Al is a candidate for spin-dependent DM search.

- NaI - a promising candidate with a large light output ($\sim 550\%$ of CaWO_4 at 300K). In addition, ^{127}I makes spin-dependent DM search possible. However, NaI is difficult to handle, since it is highly hygroscopic and fragile.
- Molybdates X_YMoO_4 - e.g. Li_2MoO_4 has been measured at 10mK. The light output, however, is only $\sim 6\%$ compared to CaWO_4 at 9K [59], which makes it less favourable for DM experiments.

A detailed understanding of the light-response of such materials is required in order to achieve maximum performance in a large-scale experiment as EURECA. In its final phase, the neutron scattering experiment in Garching will be equipped with a sophisticated light-detector (see section 11.1.3) and an ultra-sensitive, modular phonon detector, which can be attached to the respective target materials.

Especially after the recent publications of the CDMS experiment [18], a confirmation of the limits for the WIMP-nucleon cross-section - measured with different target materials (to check $\sim A^2$ proportionality) - is of great interest for a deeper understanding of the origin of Dark Matter.

Bibliography

- [1] F. Zwicky, *Astroph. J.* **86**, 217 (1937).
- [2] G. Bertone, D. Hopper, and J. Silk, *Phys. Rep.* **405**, 279 (2005).
- [3] K. G. Begemann, P. Salucci, and F. Stel, *Mon. Rot. R. Astron. Soc.* **249**, 439 (1991).
- [4] A. A. Penzias and R. R. Wilson, *Astroph. J.* **142**, 419 (1965).
- [5] M. R. Nolta *et al.*, arXiv:astro-ph/0803.593v1 (2008).
- [6] D. N. Spergel *et al.*, *Astroph. J. Suppl. S.* **170**, 377 (2007).
- [7] D. Clowe, A. Gonzales, and M. Markevitch, *Astroph. J.* **604**, 596 (2004).
- [8] C. Kraus *et al.*, *Eur. Phys J. C* **40**, 447 (2005).
- [9] R. Trotta, R. R. de Austri, and L. Roszkowski, *New Astron. Rev.* **51**, 316 (2007).
- [10] L. J. Rosenberg and K. van Bibber, *Phys. Rep.* **325**, 1 (2000).
- [11] G. Angloher *et al.*, *Astropart. Phys.* **31**, 270 (2009).
- [12] C. Isaila, PhD thesis, in preparation, TU München .
- [13] M. Aglietta *et al.*, *Phys. Rev. D* **58**, (1998).
- [14] J. Ninkovic *et al.*, *Nucl. Instr. and Meth. A* **564**, 567 (2006).
- [15] T. Jagemann, PhD thesis, TU München (2004).
- [16] C. Coppi, PhD thesis, TU München (2009).
- [17] S. Pfister, private communication (2010).
- [18] Z. Ahmed *et al.*, arXiv:astro-ph/0912.3592v1 (2009).
- [19] E. Armengaud *et al.*, arXiv:astro-ph/0912.0805v1 (2009).
- [20] R. Bernabei *et al.*, arXiv:astro-ph/0804.2741v1 (2008).
- [21] D. P. Finkbeiner, T. Lin, and N. Weiner, arXiv:astro-ph/0906.0002v1 (2009).
- [22] J. Angle *et al.*, *Phys. Rev. Lett.* **100**, (2008).
- [23] E. A. Baltz and P. Gondolo, *Phys. Rev. D* **67**, (2003).

- [24] <http://dmttools.brown.edu> (2010).
- [25] H. Kraus *et al.*, J. Phys.: Conf. Ser. **39**, 139 (2006).
- [26] S. Cebrian *et al.*, Astropart. Phys. **15**, 79 (2001).
- [27] H. Kraus *et al.*, Dark Energy/Dark Matter Conference Lyon (2008).
- [28] R. Lang, PhD thesis, TU München (2008).
- [29] J. E. and others, Phys. Rev. D **71**, (2005).
- [30] P. Meunier, Appl. Phys. Lett. **75**, 1335 (1999).
- [31] J. B. Birks, *Scintillation Counters* (PUBLISHER, ADDRESS, 1953).
- [32] G. F. Knoll, *Radiation Detection and Measurement* (Wiley, ADDRESS, 1989).
- [33] H. Wulundari *et al.*, arXiv:hep-ex/0401.032 (2003).
- [34] S. Scholl, PhD thesis, in preparation, Universität Tübingen .
- [35] W. Westphal, PhD thesis, TU München (2008).
- [36] C. Ciemniak, PhD thesis, in preparation, TU München .
- [37] T. Jagemann *et al.*, Astroparticle Phys **26**, 269 (2006).
- [38] <http://www.nndc.bnl.gov> (2010).
- [39] <http://www.mathworks.com> (2010).
- [40] W. Carli, private communication (2009).
- [41] M. Drog, NIM A **254**, 466 (1987).
- [42] W. v. Witsch *et al.*, NIM **138**, 13 (1979).
- [43] <http://www.item.info> (2010).
- [44] J.-C. Lanfranchi *et al.*, Opt. Mat. **31**, 1405 (2009).
- [45] F. Pobell, *Matter and Methods at Low Temperatures* (Springer, ADDRESS, 2007).
- [46] T. Marrodán, PhD thesis, TU München (2008).
- [47] E. Simon, PhD thesis, Université Lyon (2001).
- [48] <http://www.eljentechnology.com> (2010).
- [49] L. Oberauer, private communication (2009).
- [50] R. Moellenberg, Diploma thesis, TU München (2009).
- [51] C. Cozzini *et al.*, Phys. Rev. C **70**, (2004).

- [52] W. Demtroeder, *Experimentalphysik 1* (Springer, ADDRESS, 2003).
- [53] <http://mathworld.wolfram.com/MovingAverage.html> (2010).
- [54] P. N. Luke, *J. Appl. Phys.* **64**, 6858 (1988).
- [55] B. Neganov and V. Trofimov, *Otkrytia i izobreteniya* **146**, 215 (1985).
- [56] V. B. Mikhailik and H. Kraus, *J. Phys. D: Appl. Phys* **39**, 1181 (2006).
- [57] N. Coron *et al.*, *NIM in Phys. Research A* **554**, 195 (2005).
- [58] M. Luca, PhD thesis, Université Lyon (2006).
- [59] O. P. Barinova *et al.*, Eslevier Science, submitted .

Acknowledgements

Zu allererst möchte ich mich bei Prof. Franz von Feilitzsch bedanken, dass ich bei E15 in ein so angenehmes, freundliches Umfeld aufgenommen wurde und dass ich das Vertrauen bekam, selbständig wissenschaftlich arbeiten zu können. Trotz seines vollen Terminplans fand er immer wieder Zeit wichtige Themen zu besprechen. Seine Beiträge haben maßgeblich zum Gelingen des Streuexperiments sowie dieser Arbeit beigetragen. Nie vergessen werde ich den Tag an dem wir zusammen im Labor Detektoren getestet haben und die vielen interessanten Diskussionen, die auch über physikalische Fragen hinausgingen. Wegen seiner wissenschaftlichen Arbeit aber auch seiner menschlichen Art ist er mir ein Vorbild.

Ganz besonders bedanke ich mich bei folgenden drei Personen, von denen ich im vergangenen Jahr sicherlich am allermeisten gelernt habe. Da ich nicht weiß mit wem ich anfangen soll, das Ganze in alphabetischer Reihenfolge: Bei Christian Ciemniak bedanke ich mich besonders für alles was er mir rund um das Streuexperiment beigebracht hat. Ohne seine experimentelle Erfahrung und die Vorarbeit für das Experiment im Rahmen seiner Doktorarbeit wäre diese Arbeit unmöglich gewesen. Nicht zuletzt wegen seiner freundschaftlichen, ehrlichen Art und trotz der unzähligen Nacht- und Wochenendschichten am Beschleuniger hat mir die gemeinsame Arbeit immer sehr viel Spaß gemacht.

Ich bedanke mich bei Jean-Côme Lanfranchi, der stets für alle Fragen ein offenes Ohr hat, der mir immer geholfen hat wo es geht und dem ich einen Großteil dieser Arbeit zu verdanken habe. Ganz besonders werden mir die Dienstreisen und der Crash-Kurs "Vorträge halten" in Grenoble in Erinnerung bleiben. Danke auch für die Korrektur dieser Arbeit.

Ohne die unzähligen Diskussionen mit Walter Potzel, sein physikalisches Verständnis und schier unbegrenztes Fachwissen wäre das Experiment und diese Arbeit undenkbar. Ich bedanke mich für die vielen Stunden die er mit der Korrektur und Diskussion dieser Arbeit verbracht hat, davon viel in seiner Freizeit und über die Weihnachtsfeiertage. Seine Sicht auf die Dinge und seine Freude an der Physik haben mich stets motiviert.

Bei Prof. Lothar Oberauer und Prof. Tobias Lachenmaier bedanke ich mich ebenfalls für die Aufnahme bei E15 und viele interessante Diskussionen, für die sie immer Zeit fanden.

Ein besonderer Dank gilt Herrn Hagn, der uns immer bereitwillig in elektronischen Fragen zur Seite stand und ohne den ein störungsfreies Messen unmöglich wäre. Seine Erfahrung gepaart mit unglaublichem Fachwissen und großer Einsatzbereitschaft sowie

seine radioastronomischen Experimente sind eine grosse Bereicherung für den Lehrstuhl.

Walter Carli und die Operateure am Beschleuniger standen immer bei Fragen rund um den Beschleuniger sowie technischen Problemen zur Verfügung und haben deshalb einen grossen Anteil am Gelingen dieses Experimentes.

Von Sebastian Pfister habe ich viel über das CRESST Experiment am Gran Sasso gelernt. Nicht zuletzt durch ihn haben mir die Aufenthalte am Gran Sasso immer sehr viel Spaß bereitet.

Bei meinem Büro Kollegen Christian Isaila bedanke ich mich für die Einführung in die Welt von Neganov-Luke und unzählige Gespräche über Gott und die Welt.

Die Experimente zur Untersuchung der Szintillatoren zusammen mit Randolph Möllenberg haben mir sehr viel Spass gemacht. Die Diskussionen mit ihm und Michael Wurm haben mir sehr viel für meine Arbeit gebracht.

Ich danke Chiara Coppi, Sabine Roth, Moritz v. Sivers und Achim Gütlein für die nette Zusammenarbeit in der CRESST Gruppe.

Ich bedanke mich bei Alda Cavallini, die als Werkstudentin maßgeblich zur der Befüllung der Neutronendetektoren beigetragen hat.

Dann bedanke ich mich herzlich bei allen Helfern während der vielen Strahlzeiten am Beschleuniger, besonders bei den Tübingern, die viele Tage hier in Garching verbracht haben: Bei Klemens Rottler, Christoph Sailer, Stephan Scholl, Marcel Kimmerle, Gerhard Deuter, Igor Usherov, Sebastian Diebold und Marc Pfeifer. Und natürlich bei allen Diplomanden, Doktoranden und Professoren(!) von E15 die brav ihre Nachtschichten am Beschleuniger gemacht haben. Ein Riesen Dankeschön dafür!

Ich bedanke mich herzlich bei Sonja Kraus und Maria Bremberger für ihre überaus wichtige Arbeit.

Außerdem danke ich dem Werkstatt-Team rund um Harald Hess, die viele mechanische Arbeiten am Experiment durchgeführt und immer neue Ideen eingebracht haben.

Ein ganz besonderer Dank gilt meinen Eltern, die mich auf meinem Weg immer unterstützt und mir finanziell unter die Arme gegriffen haben.